Accounting for Thermal Resorption of Bubbles in Magma in Experiments and Volcanic Eruptions

Eleanor Alice Dunn

How to cite:

Dunn, Eleanor Alice (2023) Accounting for Thermal Resorption of Bubbles in Magma in Experiments and Volcanic Eruptions. Masters thesis, Durham University.

Accounting for Thermal Resorption of Bubbles in Magma in Experiments and Volcanic Eruptions

Eleanor Alice Dunn
Masters by Research (Volcanology)

Supervisors: Professor Ed Llewellin, Dr Fabian Wadsworth, Dr Madeleine Humphreys & Dr Jason Coumans

Department of Earth Science
University of Durham

January 2023

Abstract

The growth of bubbles drives volcanic eruptions and plays a major role in determining eruption style. Therefore, understanding bubble growth processes is essential for forward modelling of volcanic eruptions and for interpretation of vesicular eruptive products. Decompression experiments at high temperature and pressure have been widely used to investigate bubble growth processes. However, most studies neglect bubble resorption, which occurs during the quench process as water solubility increases with decreasing temperature. Resorption may alter final textures, so accounting for this process is important for interpretation of experimental products.

This study quantifies the extent to which bubble resorption during cooling/quenching modifies the gas volume fraction (ϕ) of the products of a series of decompression experiments. A numerical model is applied that captures bubble growth and resorption over arbitrary pressure-temperature-time (P-T-t) pathways to a published experimental dataset. The analysis proceeds in three stages: 1) Reconstruct the experimental P-T-t pathways and determine how ϕ evolves with time, in order to reconstruct pre-quench values. 2) Vary values of experimental parameters, such as bubble number density (N_b) and cooling rate to show when quench modification is most important. 3) Carry out a parametric sweep and advise on the best experimental conditions to use to avoid over-printing of experimental samples via resorption.

Resorption occurs in all experimental samples that are analysed. In one sample, the final ϕ is over a 50% decrease of the original bubble growth, consistent with values determined by a previous study. The analysis indicates that thermal resorption must be accounted for in the interpretation of experimental results and that greater resorption occurs when N_b is high and cooling rate is low. In some instances, this leads to bubbles resorbing completely from a peak ϕ value as high as 0.10. The numerical model can be used as a tool to design experiments and minimise the effect of resorption, and it is anticipated that this will support more meaningful interpretation of vesicle textures and size distributions.

Contents

List of Figures

1. Introduction

2. A Conceptual Understanding of Bubble Modelling

3. A Theoretical Understanding

4. Importance of Resorption

5. Resorption Driven by Quench

6. Parametric Investigation of Quench Resorption

List of Tables

2. **A Conceptual Understanding of Bubble Resorption**

3. **A Theoretical Understanding**

4. **Importance of Resorption**

5. **Resorption Driven by Quench**

6. **A Parametric Investigation of Quench Resorption**

Statement of Copyright

Acknowledgements

I would like to thank Professor Ed Llewellin, my main supervisor, for his continuous encouragement throughout my masters and for reading through my many drafts. I would also like to thank my co-supervisors Dr Fabian Wadsworth, Dr Madeleine Humphreys, and Dr Jason Coumans for their endless support and knowledge.

Outside of the department I would like to thank my Durham, Bedford, and Egham friends for always being there for me. Finally, I would like to thank my family for never letting me give up and my boyfriend, Andrew, for always making me smile.

1. Introduction

1.1 Thesis Rationale

Bubble growth drives volcanic eruptions, and the understanding of bubbles/vesicles is imperative in understanding eruption styles. Bubble resorption is a crucial process, creating smaller bubbles than would be predicted from bubble growth as bubbles migrate up the volcanic conduit and the pressure drops. Thermal resorption modifies the textures of volcanic products, particularly vesicularity, so that the textures are different from what would be expected at the point of eruption. It also modifies textures of experimental products so that textures are different from how they were during experiments. Resorption needs to be understood if bubbles/vesicles are to be correctly interpreted. A better understanding of bubble processes is required to improve volcanological knowledge of conduit behaviour, which influences the explosivity or effusivity of a volcanic eruption and any subsequent activity. Being able to further understand conduit behaviour will improve volcanic hazard planning and safety efforts.

Bubble properties have been linked to the explosivity of eruptions; bubble content can control magma rheology/viscosity and viscosity changes may create an explosive or effusive eruption (Cassidy et al., 2016; Di Genova et al., 2017). Bubble connectivity and bubble number density (N_b) can control magma porosity and permeability whereby a higher porosity may promote more outgassing and can alter fragmentation (Sparks, 2003; Cashman, 2004; Mueller et al., 2005; Mueller et al., 2008; Rust et al., 2011; Degruyter et al., 2012). The presence of gas bubbles in magma can increase buoyancy and ascent speed (Gardner, 2009) which will lead to an explosive eruption (Winson et al., 2014). Evidence for the consequences of bubble growth has been found in natural samples from the explosive eruption of Mount Pinatubo in 1991. This suggests that growth of gas bubbles during magma ascent leads to intense shear and possibly fragmentation at the conduit walls (Polacci et al., 2001). These properties will all be influenced by a variety of factors at play in the volcanic conduit.

Observation of bubble growth changes in situ is difficult; requiring a combination of analytical methods to understand bubble growth in natural samples and experimental methods to understand how bubbles grow at magmatic conditions. In natural samples vesicles are examined as bubbles frozen in time and used to constrain how the volcanic product is formed and under what conditions (Kaminski and Jaupart, 1997; Larsen and Gardner, 2000; Giachetti et al., 2010). In decompression experiments, synthetic samples are used to characterise bubble growth by simulating volcanic conditions. Despite these methods, many unanswered questions remain, such as: 1) Do experimental studies make valid assumptions about what is happening to bubbles during experiments? 2) What are the key influences on bubble resorption following experimental decompression? And 3) What can be learnt from analysis of experimental resorption about natural resorption?

Bubble growth can be influenced by 1) the pressure and temperature conditions in the volcanic conduit; 2) magmatic properties; and 3) volcanic behaviour. The changing physical parameters of bubbles will then, in turn, influence: 1) rheology of the magma (Manga et al., 1998; Lejeune et al., 1999; Pal, 2003); 2) buoyancy (Corsaro, 2004); 3) compressibility (Killbride, 2016); 4) connectivity and permeability (Klug and Cashman, 1996; Blower, 2001; Mueller et al., 2008; Westrich and Eichelberger, 1994); and 5) shear stress partitioning into thinning melt films between bubbles (Rust et al., 2003; Caricchi et al., 2011). This study will address how resorption affects bubbles during decompression experiments.

1.2 Bubble Growth in Volcanism

Magmas contain dissolved volatiles (e.g., CO_2, H_2O) and the gradient between magma storage pressure and atmospheric pressure, supersaturates the magma in these volatiles, forming a free gas phase at low pressures. The presence of volatiles influences the bulk density of the magma and in turn controls the magma ascent rate, influencing the explosivity of a volcano.

Bubble formation and growth occur under low pressure conditions when magma is supersaturated with volatile species. The first stage is bubble nucleation which occurs when volatiles begin to form as a vapor phase in the magma. As the magma rises, pressure falls and the solubility of the volatiles decreases with the magma becoming saturated or supersaturated with respect to the volatiles, causing bubble growth (Gardner et al., 1999). Often, significant supersaturation is required to form the bubbles at all (Toramaru, 2006). At depths shallower than saturation, bubbles that have formed will grow as the magma continues to rise, initially following an isothermal pathway (Mastin, 2002; Gonnermann and Manga, 2007). Therefore, decompression will always result in bubble growth.

The depth at which saturation takes place is constrained by; the percentage of volatiles dissolved in the magma, the solubility of the volatiles and additional factors such as the presence of crystals. Crystals create a more complex bubble system when the oxides are used as nucleation sites, aiding bubble nucleation (Mangan and Sisson, 2000; Martel et al., 2001; Hammer and Rutherford, 2002). When volatile solubility in the melt decreases, volatiles exsolve from the melt into the bubble (Blank et al., 1993; Dixon et al., 1995, Carroll et al., 1997; Blower et al., 2001). Solubility is a key factor controlling the ascent rate of bubbles, along with magma viscosity and the decompression rate, which influences how quickly the bubbles will grow and reach the surface (Verhoogen, 1951; Toramaru, 1995; Larsen and Gardner, 2000; Blower et al., 2001). The decompression of magmatic volatiles causes the process of rapid expansion and fragmentation at the surface, and therefore the explosivity of an eruption is a product of bubble growth (Taylor et al., 1983; Toramaru, 1995; Rust et al., 2004; Castro et al., 2012; Carey et al., 2013).

Diffusion of volatiles into the bubble will affect bubble growth rate as it controls the gas volume fraction of the bubble and the subsequent increase in bubble size (Proussevitch and Sahagian, 1998; Blower, 2001). The equation of station (EOS) is a thermodynamic equation relating state variables, used to describe the state of matter under a given set of physical conditions – in this case representing how pressure and temperature influence the state of H_2O in the bubble. In bubble growth, this is often represented by the ideal gas law, which considers pressure, volume, temperature, and the amount of substance.

Acting to resist bubble growth are viscous forces of the bubble walls and surface tension which act against the viscosity and the EOS (Gaonac'h et al., 1996; Proussevitch and Sahagian, 1998). A bubble growth model needs to account for all these effects as they are all relevant during ascent.

The pressure-temperature-time pathway controls the changing bubble size (Sparks, 1978) and is dependent on where the bubble is forming within the magmatic system. This pathway can have constant pressure and temperature throughout (isobaric, isothermal), a constant pressure and changing temperature (isobaric, polythermal), a changing pressure and constant temperature (polybaric, isothermal) or a changing pressure and changing temperature (polybaric, polythermal). These different pathways and subsequent conditions are presented in figure 1.1.

1.3 Experimental Volcanology

To constrain bubble growth processes, reconstruction of in-conduit conditions during transportation and eruption is carried out via experiments to replicate the different pressure-temperature-time pathways that are illustrated in figure 1.1. This is done by developing an understanding of the physics of each process and by looking at a spectrum of compositions and conditions. This laboratory-scale volcanic plumbing provides experimental access into the Earth's subsurface.

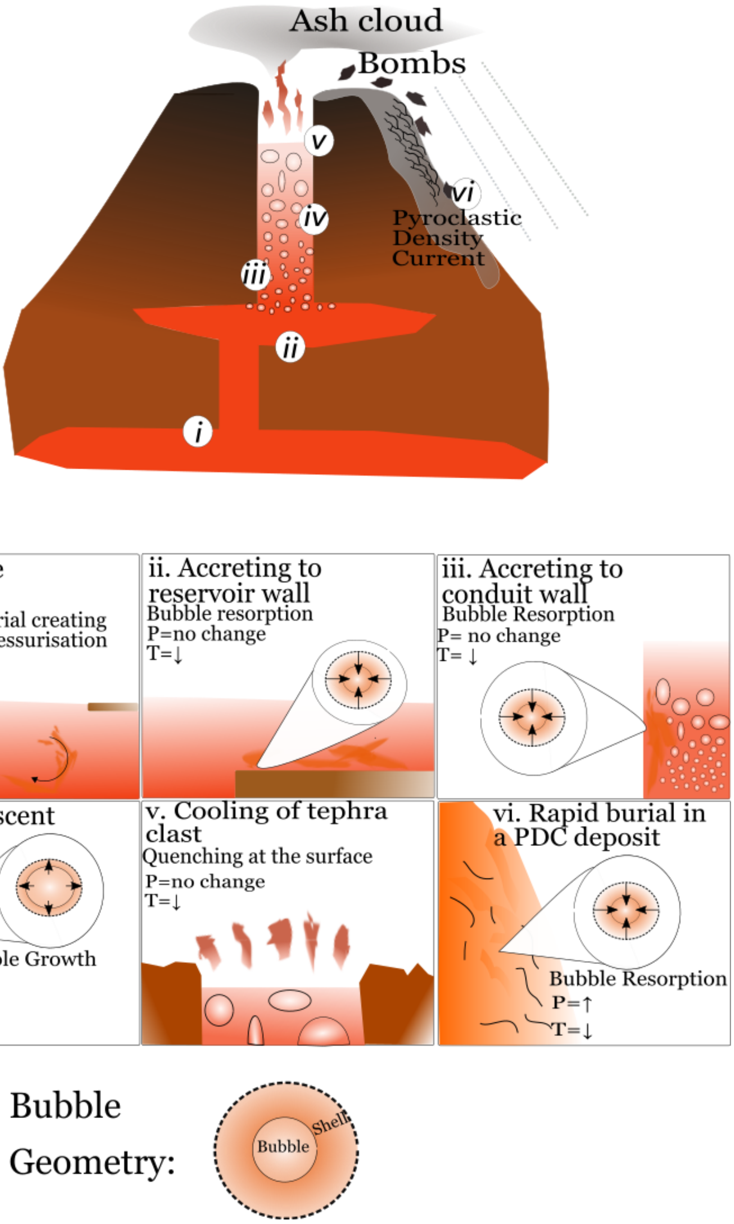

Figure 1.1 The different environments present in a volcanic system; i) the process of cycling between two separate magma reservoirs is shown (Moussellam et al., 2015; Sparks et al., 2019), ii) bubble resorption can happen as magma accretes to the reservoir wall, causing a decrease in temperature (Hansteen and Krügel, 1998), iii) similarly, accreting to the conduit as magma ascends also occurs which can also cause resorption (Heap et al., 2017). For iv) as the bubbles travel up the vent, they degas as temperature and pressure decrease, causing bubble growth as the magma reaches the top of the conduit (Scandone et al., 2007; Rutherford, 2008), v) as magma fragments when erupted and there is rapid quenching at the surface where resorption occurs (Gonnermann, 2015; White and Valentine, 2016), and vi) once erupted, rapid burial via pyroclastic density current (PDC), causing repressurisation of the magma and resorption (Petcovik and Dufek, 2005; Sparks et al., 1999).

Decompression experiments at high temperature and high pressure are used to simulate bubble growth (Mourtada-Bonnefoi and Laporte, 2004; Burgisser and Gardner, 2005; Gardner, 2007; Shea, 2017) and by creating a controlled pressure and temperature environment, enable bubble pathways to be studied in detail. A typical experimental set-up involves an externally heated pressure vessel, fitted with a rapid-quench attachment (Jacobs and Kerrick, 1980), which creates the polybaric-dwell, isothermal-then-quench environment required for resorption. This is used to mimic the decompression processes by first equilibrating the sample and then applying a specified decompression under pressure, temperature, and time constraints. A small aliquot of a natural sample is placed in tubing and welded shut, typically after water has been added to the sample to ensure volatile saturation at the start of decompression, creating an initial equilibrium population of bubbles. Many studies involve samples which are held at constant pressure and temperature before being decompressed quasi-instantaneously to reach equilibrium (figure 1.2), although studies may also investigate samples at disequilibrium for different desired results (Mangan and Sisson, 2000; Iacono-Marziano et al., 2007).

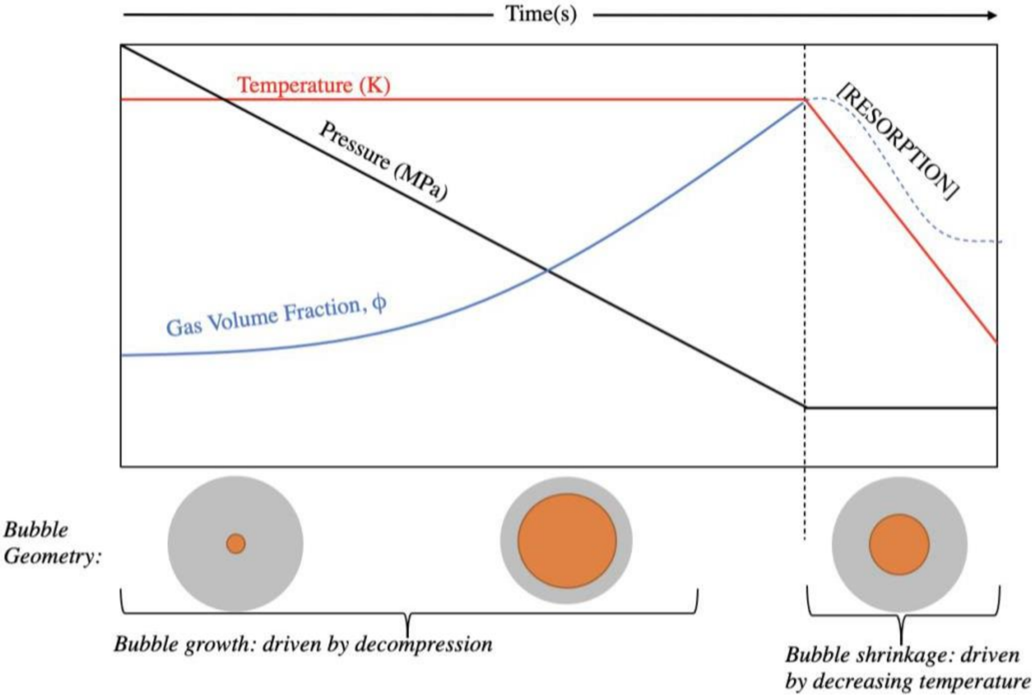

Figure 1.2 Schematic figure displaying the changing bubble size in a typical decompression experiment, a bubble growing due to decreasing pressure and steady temperature before bubble resorption, represented by an increase in gas volume fraction, then occurs due to decreasing temperature and constant pressure.

Experiments can vary in terms of operation and one such operation is to reproduce observed pyroclasts and eruption products such as the vesicle number density (VND) and vesicle size distribution (VSD) (Kaminski and Jaupart, 1997; Lavallee et al., 2015; Pappalardo et al., 2018).

All modes of operation in experimental volcanology aim to use sample results of experiments as a textural record of the pressure-temperature pathway. However, a key feature of experiments is that the samples must be cooled down to inspect the results. At low pressures (< 300MPa) cooling results in an increase in solubility – which can undo the growth of bubbles via resorption. This thesis aims to test the assumption that experimental products are tied to the target conditions of the experiments prior to quenching.

Understanding resorption and the impact it has on bubbles under different conditions can influence future research into bubble growth and enable a better understanding of conduit conditions.

1.4 Bubble Resorption

Bubble resorption occurs when increasing solubility increases the water concentration at the bubble wall, creating a chemical potential gradient in the melt which drives volatiles away from a shrinking bubble, into the melt, causing the bubble to shrink. Depending on the quench rate, this water concentration profile can be preserved when the melt quenches to glass (Zhang and Ni, 2010; Watkins et al., 2012; McIntosh et al., 2014); if it quenches slowly then the gradients relax through diffusion. Unless highly supersaturated, a growing bubble during decompression becomes a shrinking (resorbing) bubble when quenched. Most studies neglect bubble resorption that occurs during the quenching process. However, resorption may alter final textures, so accounting for this process is important for interpretation of experimental products. Resorption occurs in several different volcanic environments, as pictures in figure 1.1.

Within the volcanic conduit resorption occurs during accretion to the conduit wall as there is a decrease in temperature as the melt moves to the outer regions but no change in pressure. Similarly, rapid quenching at the surface, creates a sharp decrease in temperature, after the pressure drop during magma ascent triggers bubble growth. Following the eruption, burial in PDCs decreases the temperature and increases the pressure, influencing solubility of the melt and thus, resorption.

McIntosh et al. (2014) describes the processes of resorption and provides experimental evidence based on re-analysis of vesicular rhyolite samples from rapidly quenched decompression experiments (taken from Burgisser and Gardner, 2005). Upon rapid cooling of decompression samples, spatial distribution of the water concentration around the bubbles is preserved, allowing insight into the pre-eruptive conditions. It is assumed that water will decrease towards the bubble, representing a quenched snapshot of the situation during bubble growth however what is found is that the water increases towards the bubble, indicating that resorption has occurred. Textural evidence indicates that resorption occurs before the melt solidifies. The water content is quantified using Back-Scatter Electron Microscopes (BSEM) and Fourier Transform Infrared (FTIR), producing images which display a distinct resorption halo around the quenched samples.

1.5 Numerical Modelling of Bubble Growth and Resorption

Bubble growth modelling has been a goal of volcanology since Verhoogen (1951), and a versatile mathematical description is required to constrain the required bubble growth conditions. Numerical modelling is a necessary player in understanding bubble growth because when bringing together all factors at play in the volcanic conduit, it is impossible to summarise these processes with only simple equations, without broad assumptions, such as the pressure and temperature conditions that are followed. However, if the aim is to explore the complexities of the volcanic conduit, then these assumptions cannot be made without falsely representing the volcanic system.

Numerical models are often used to test complex mathematical scenarios such as bubble growth. In this study, a numerical model is used to evaluate bubbles in equilibrium conditions and how they grow and resorb with changes in pressure, N_b and cooling rate. Resorption, a process only recently understood and documented, is a crucial process in bubble pathways and is influenced by changing water concentration at the bubble wall. The processes that can increase and decrease the amount, rate, timescale, or the amplitude of bubble resorption are poorly understood despite their impact on volcanic eruptions and products.

Coumans et al. (2020) develops a numerical model which can capture bubble growth and the resorption process over arbitrary pressure-temperature-time pathways using published datasets. Coumans et al. (2020) uses data from Burgisser and Gardner (2004), Mourtada-Bonnefoi and

Laporte (2004) and Hamada et al. (2010) to demonstrate how the numerical model works and how it quantifies resorption based on experimental parameters.

In Coumans et al (2020) the numerical model is used to improve and/or correct interpretations of high-pressure high-temperature experiments and is then applied to natural volcanic systems, while the influence of resorption on various experimental and natural scenarios is investigated. The numerical model has potential to be applied to a range of studies in the future, including: the optimisation of decompression experiments for the simulation of continuous magma ascent (Marxer et al., 2015); bubble formation in evolved alkaline melts (Buono et al., 2020) and using high-temperature high-pressure vesiculation experiments to highlight bubble growth dynamics in post-fragmentation volcanic bombs (Browning et al., 2020). Natural scenarios include looking at repeated cycles of decompression (Gardner et al., 2018), quenching and heating post-eruptive expansion of bubbly pyroclasts (Kaminski and Jaupart, 1997; Giachetti et al., 2010), and post-emplacement cooling-driven resorption in pyroclasts (Watkins et al., 2017). The above studies have all made conclusions based on textural characteristics and use these to infer the process of bubble growth. Applying the numerical model could alter the conclusions made and offer alternative explanations. Alternately, the numerical model could provide evidence that resorption does not play a significant role in the bubble growth process.

1.6 Thesis Structure

This thesis will explore the concepts behind bubble growth and resorption, expanding beyond what is written in this introduction. The theory behind the Coumans et al. (2020) numerical model as well as additions made to the model during this project, will also be included.

Firstly, the background of the project will be discussed in Chapter 2 and 3, in relation to previous work and the Burgisser and Gardner (2005) study, with an in depth look at the experimental set up and results. The numerical methods are also discussed along with the key features of the model applicable to this study. Chapter 2 – a conceptual understanding, looks at the underlying concepts of bubble growth and Chapter 3 – a theoretical understanding, looks at the theoretical aspects of the numerical model.

In Chapter 4 the importance of resorption will be investigated. This will look at the equilibrium sample from Burgisser and Gardner (2005) and its validity while also discussing how the samples are computed in the numerical model. The difference between linear and newton cooling pathways is discussed and how these two pathways can be investigated using two different approaches. One pathway will be selected for use in the rest of the study.

In Chapter 5 resorption driven by quench is looked at. Four samples from Burgisser and Gardner (2005) are put into the numerical model to investigate initial signs for resorption. The effect of changing the decompression rate, final pressure (controlled variables) and N_b (stochastic variable) are investigated using four samples.
In Chapter 6 a parametric investigation of quench resorption is undertaken. This will involve a study of the key influences involved in bubble resorption (N_b, cooling rate, initial pressure, and pressure change) and how resorption is affected by these changes. Real world studies of different pressure and temperature environments is discussed in relation to these results e.g., how much resorption may a submarine volcano experience?

Chapter 7 sums up the study and any implications, final conclusions, and suggestions for further work. This includes what changes are recommended to be made to future studies of bubble growth and decompression experiments. This study is summarised, and the main conclusions highlighted. Finally, implications for the field of volcanology are examined.

2. A Conceptual Understanding of Bubble Modelling

2.1 Introduction

Modelling of bubble growth yields a deeper understanding of volcanic processes and can highlight the relevant parameters behind growth and resorption. The current understanding of bubble growth in relation to the Coumans et al. (2020) study is discussed and questions arising from the study are then outlined.

The growth and rise of bubbles are a key factor in creating either an effusive or explosive eruption such as by influencing porosity and magma rheology and so it is important to understand the inner workings of the volcanic conduit and the physics of rising bubbles. The study of bubble growth and subsequent modelling has existed for many decades with mathematical equations to explain the relevant processes behind bubble growth being published by Verhoogen (1951). The Verhoogen (1951) study highlights how the kinetics of gas evolution, specifically, bubble number density (N_b), is what is crucial to ash formation based on mathematical analysis, and not viscosity as proposed by Rayleigh (1917) and Lamb (1932). As bubble resorption is still a newly developed concept, there is limited modelling of the process.

2.2 Modelling of Bubble Growth

2.2.1 Early Research

Early research into volcanic conduit systems demonstrates that it is important to understand how bubbles behave as they rise to the surface and influence an eruption. Verhoogen (1951) proposes mathematical equations which demonstrate that small bubbles in magma experience higher velocities when rising up the volcanic conduit in comparison to magma that contains larger bubbles. This is the difference between lava 'boiling' and lava fragmentating and represents the link between bubbles and volcanic behaviour. This initial vesiculation theory by Verhoogen (1951) has laid the groundwork for modelling of bubble growth.

Verhoogen's research has been expanded upon and modified (McBirney, 1963; McBirney and Murase, 1970; Bennett, 1974). McBirney (1963) finds that the rate at which bubbles ascent is slow compared to the rate of ascending magma in volcanic conduits and thus Verhoogen's (1951) findings have a limited application to the volcanic environment. Environments such as lava lakes are applicable to Verhoogen's study because there is little vertical movement in the conduit, but submarine volcanism is not suitable because it does not follow Verhoogen's assumptions that ascent rate of bubbles and magma are equal.

Verhoogen (1951), McBirney (1963) and McBirney and Murase (1970) all use various equations in relation to pressure, bubble volume and radius to discuss the open questions that remain such as influences on bubble growth rate. Sparks (1978) is the first to use a numerical model to investigate bubble processes and growth rates.

Sparks (1978) develops a model which considers the effect of growth due to: decompression, magma ascent rate, magma viscosity, gas solubility, gas content, and volatile species diffusivity, on bubble growth rates. A numerical model is developed to calculate bubble growth rate during volcanic eruptions of basaltic and rhyolitic magmas. Sparks concludes that most bubbles stop growing prior to explosive disruption of magmatic froth because bubbles cannot expand further due to an increase in viscosity of the melt which has to be forced between closely spaced neighbouring bubbles, along very thin paths. This view continues to change into the current understanding of today, yet it remains an important concept in the study of bubble growth. The limitations of the Sparks (1978) model are: 1) the bubble is assumed to grow in an infinite liquid; 2) the diffusion equation is not solved fully but approximated by Scriven's law; 3) the advective flux of volatiles towards the bubble wall as the bubble grows is neglected, and 4) both volatile diffusivity and viscosity are assumed to be independent of water content.

Following Sparks (1978), Proussevitch and Sahagian (1998) and Blower (2001) both make significant contributions to modelling bubble growth. Their contributions will be discussed below.

Each parameter controlling bubble growth can be determined using numerical modelling – as determined by Proussevitch and Sahagian (1998). Their model accounts for the energetics of volatile degassing and melt deformation as well as the interactions between viscosity, volatile concentration, and diffusivity. Proussevitch and Sahagian (1998) recognise that bubbles require a model with spherical coordinates thus in numerical modelling, bubbles must be computed differently to a simple 2D shape. Proussevitch and Sahagian (1998) model decompression bubble growth as a unit cell which includes a single bubble surrounded by a finite volume of melt (figure 2.1). The volume of the shell reflects the N_b while its growth is driven by diffusion of volatiles from the surrounding melt. These bubbles are uniformly spaced to ensure simultaneous nucleation because an event distance between bubbles eliminates the need to compute nucleation dependence. This model uses a spherical coordinate system with its origin at the bubble centre. This is unlike previous models (Sparks, 1978) as the adjective flux of volatiles towards the bubble wall as the bubble grows and the diffusion equations are fully solved. This results in a model which simulates the presence of other bubbles in the system.

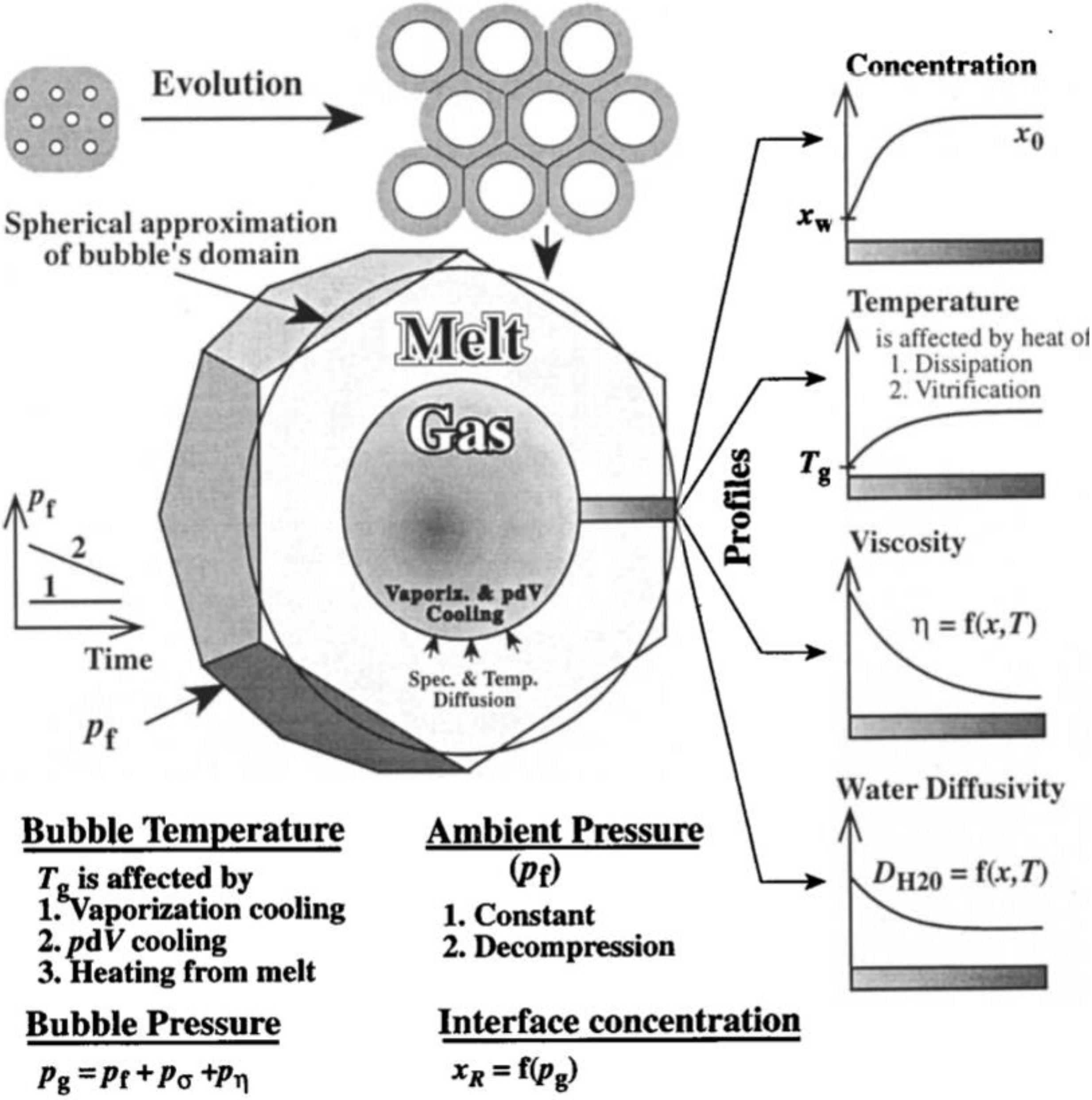

Figure 2.1 The Proussevitch and Sahagian (1998) model of a bubble. Initial bubbles are in a closely packed structure which define a unit cell which includes a single bubble surrounded by a finite volume of melt. The polygonal structure is approximated as spherical with a bubble at its centre thus reducing the 3D computational domain to 1D. The model accounts for interaction between parameters all of which are dependent on temperature and volatile content. T_g is the glass transition temperature, p_g is the pressure of the gas, p_f is ambient pressure, p_σ is pressure due to surface tension and p_η is pressure due to viscosity. The plots on the right side of the figure show the changing volatile concentration, temperature, viscosity, and water diffusion with time. It should be noted that for the conclusion Proussevitch and Sahagian (1998) are considering, the water diffusivity should decrease towards the bubbler wall.

The Proussevitch and Sahagian (1998) model allows for changing concentration, temperature, viscosity, and water diffusivity to be considered in relation to a water-saturated rhyolitic magma. The spherical coordinate system is used by Proussevitch and Sahagian (1998) and is expanded by Blower (2001) into Lagrangian coordinates.

2.2.2 Blower (2001) and Lagrangian Coordinates

Lagrangian coordinates are a more simple and accurate way to represent a system which changes geometrically over time. The Lagrangian flow field models show fluid motion as following an individual fluid parcel as it moves through space and time (Badin and Crisciani, 2018). This contrasts with the fixed coordinate system used by Proussevitch and Sahagian (1998), where the coordinates change with a changing bubble wall, making it difficult to identify where bubble boundaries lie. Blower (2001) uses Lagrangian coordinates as an improvement on the Proussevitch and Sahagian (1998) model.

The Blower (2001) model (figure 2.2.) contains equations for the diffusion of water into the bubble, hydrodynamics of motion of fluid, mass balance of water molecules, internal bubble pressure, solubility of water, viscosity, and diffusivity. These equations are based on the previous models discussed (Sparks, 1974; Proussevitch and Sahagian, 1998). The model finds that viscosity and diffusivity remain intertwined in bubble growth however Blower (2001) also finds that bubble growth is not affected by the choice of equation of state (EOS).

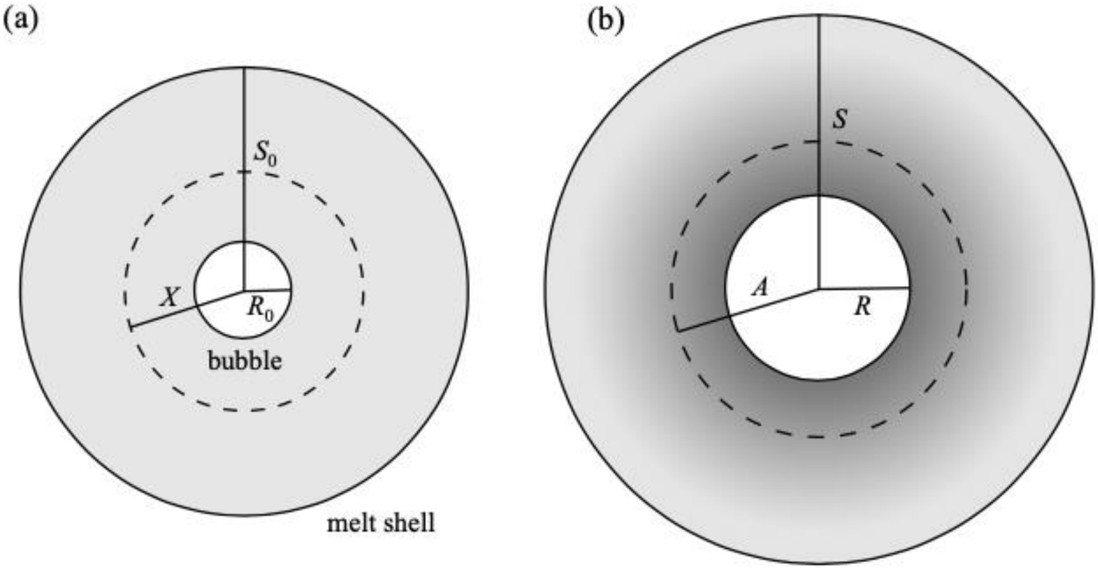

Figure 2.2 How Blower (2001) envisions the bubble growth model. A) initial conditions. The water concentration is uniform throughout the melt shell. B) conditions after time, t. The shading illustrates the increase in viscosity near the bubble wall due to volatile depletion. The bubble has grown from an initial radius, R_0 to a radius, R. The melt shell initially between R_0 and X is now contained in the region from R to A. S_0 is the initial radius of the shell.

Blower (2001) concludes that the bubble model is sensitive to boundary conditions at the bubble/melt interface. Small variations of these conditions have implications for the bubble growth rates due to the sensitivity of melt viscosity to water content at low concentrations. This importance is highlighted in the additions to the numerical model used in this study, whereby the pressure arising from surface tension of the bubble is included to calculate initial bubble conditions.

Bubble growth due to a linear pressure drop is also modelled by Blower (2001). In the case of the Burgisser and Gardner (2005) study the stage which creates a bubble population is a linear pressure drop (see section 2.5). However, Blower (2001) does not consider the process of resorption following bubble growth which is explored in the Coumans et al. (2020) model.

2.2.3 Coumans et al. (2020)

Coumans et al. (2020) discusses this issue of non-linear bubble processes and proposes a more complex model simulation of bubble growth to create a more flexible, accurate and numerically stable model. The Coumans model is purpose built to allow for any past decompression experiments to be applied to it.

Like Blower (2001), Coumans et al. (2020) uses Lagrangian coordinates. This is more computationally efficient when considering logarithmic spacing of nodes within the bubble wall which is used when computing bubble wall thickness in relation to its expansion and contraction.

Bubble growth is shown in figure 2.3 using the Coumans et al. (2020) model which has been validated against continuous in situ experimental data (Mourtada-Bonnefoi and Laporte, 2004; Burgisser and Gardner, 2005; Hamada et al., 2010), the experimental data being based on similar compositions but slightly different experimental procedures (continuous vs. discontinuous experiments). The aim of the model is to completely quantify the growth and resorption of a bubble, from equilibrium to the end of quench. Figure 2.3 displays one of the model outputs which plots gas volume fraction (ϕ) of a bubble against time. The model has been run for several different N_b to determine how this effects a growing bubble. The model allows for arbitrary temperature-pressure pathways and accounts for the impact of spatial variations in dissolved H_2O concentration on viscosity and diffusion.

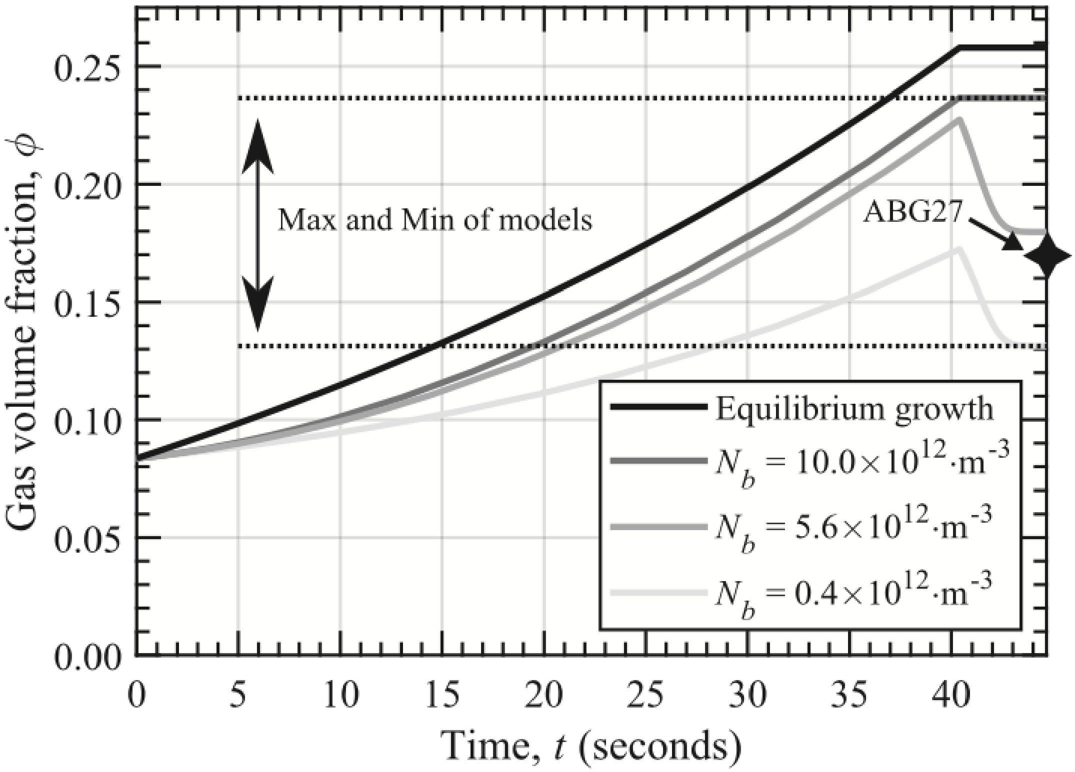

Figure 2.3 Output of the Coumans et al. (2020) model. The gas volume fraction (ϕ) changes as the experiment proceeds. Varying N_b influences the amount of bubble growth and resorption that occurs. From 0 – 40s the bubble grows by varying degrees while from 40-43s the bubble resorbs during quenching.

The Coumans et al. (2020) model uses the McIntosh et al. (2014) study to model and quantify how much of a change in bubble size there is. The McIntosh et al. (2014) study concludes that resorption occurs based on Fourier Transform Infrared (FTIR) and Back-Scatter Electron Microscope (BSEM) observations (see section 2.3) of the Burgisser and Gardner (2005) decompression experiments but the Coumans et al. (2020) model gives this resorption a numerical value. The model can confirm and quantify conclusions made by McIntosh et al. (2014) that bubble resorption has taken place.

The Coumans et al. (2020) model is used in this thesis due to its transferrable nature and application to many different types of experimental data sets. The model is created in MATLAB, a commercial programming and numerical computing platform, however the model script written by Coumans et al. (2020) is open-source and provided as supplementary material. This makes the production of plots and modelling relatively simple and is the best option for the study of a changing bubble environment. The numerical model acts as an accumulation of the work of Blower (2001), Verhoogen (1951), and Proussevitch and Sahagian (1998).

The modelling of bubble growth is built on several decades of research into what impact changing bubble size has on a volcanic system. Over time the input of factors such as diffusivity and EOS have been correlated with bubble growth to explain volcanic behaviour. Based on recent textural and geochemical findings, modelling is utilised to reveal a hidden resorption process in the final stages of a bubbles journey.

2.2.4 Using Bubble Textures to Understand Volcanic Behaviour

Aside from utilising numerical models to understand bubble behaviour and growth, bubble textures are also used. Using micro- and macroscopic images of a volcanic sample can reveal more about its formation. An example of this is Houghton et al. (2010) who uses binary images of pumices from the lower stratigraphic units of Taupo (Houghton et al., 2010; figure 2.4). These images reveal more diversity in the samples than expected based on density data and macroscopic textures. From these images, the heterogeneity of the clasts, in terms of vesicle distribution, size, shape, and elongation are inferred which is used to reflect strain localisation.

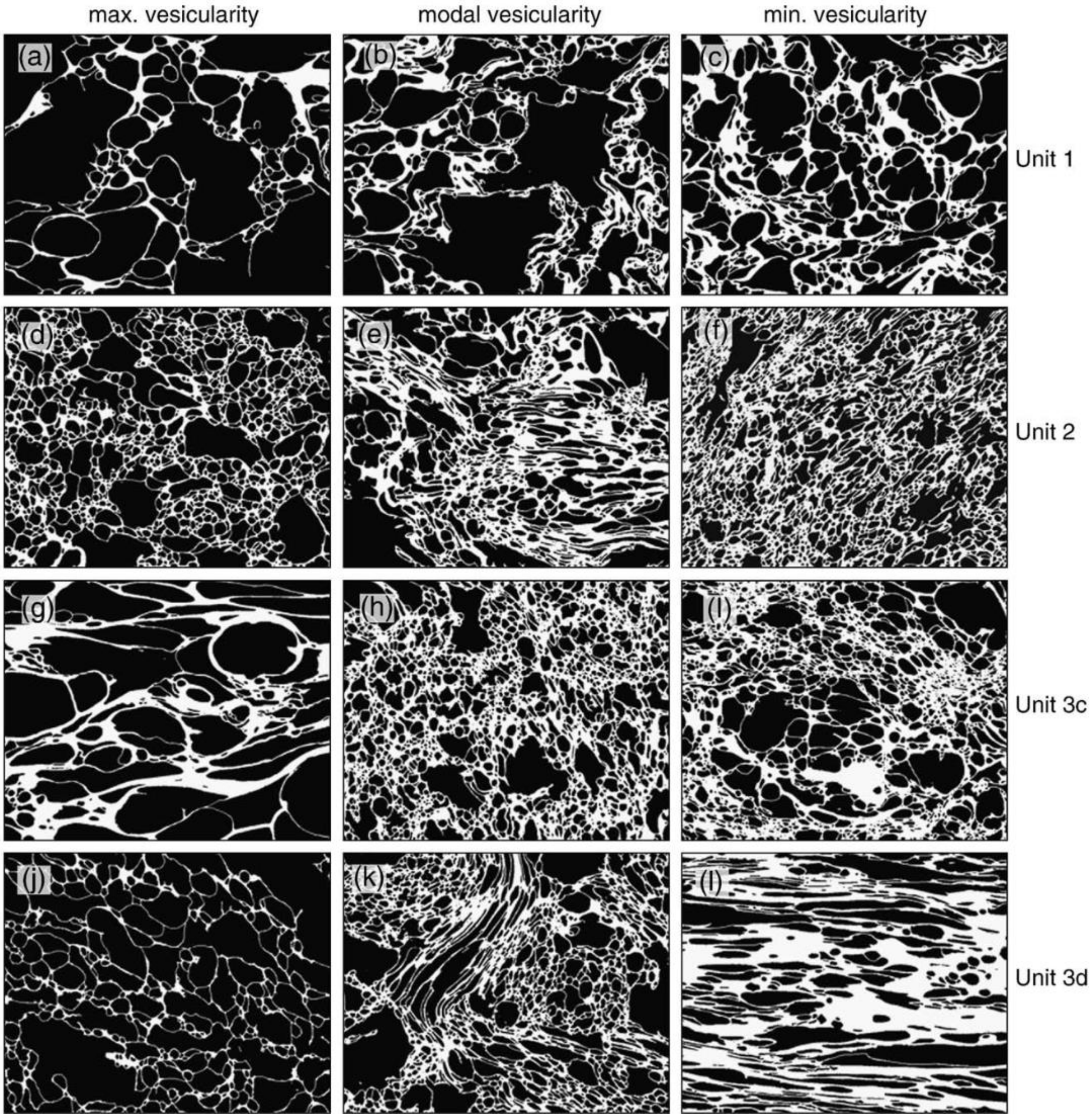

Figure 2.4 SEM images from clasts representative of the maximum (left), modal (middle), and minimum (right) vesicularity in samples from different units of the Taupo stratigraphic sequence (Houghton et al., 2010).

Pappalardo et al. (2018) use volume rendering showing 3D microstructures from Pomici di Base trachytic and latitic-shoshonitic rocks (Pappalardo et al., 2018; figure 2.5). The 3D rendering reveals that the trachytic pumices have a high degree of vesiculation and are characterised by large coalescent bubbles separated by thin glass walls. These features indicate that during decompression, bubble growth occurred for exsolution up to a certain vesicularity threshold.

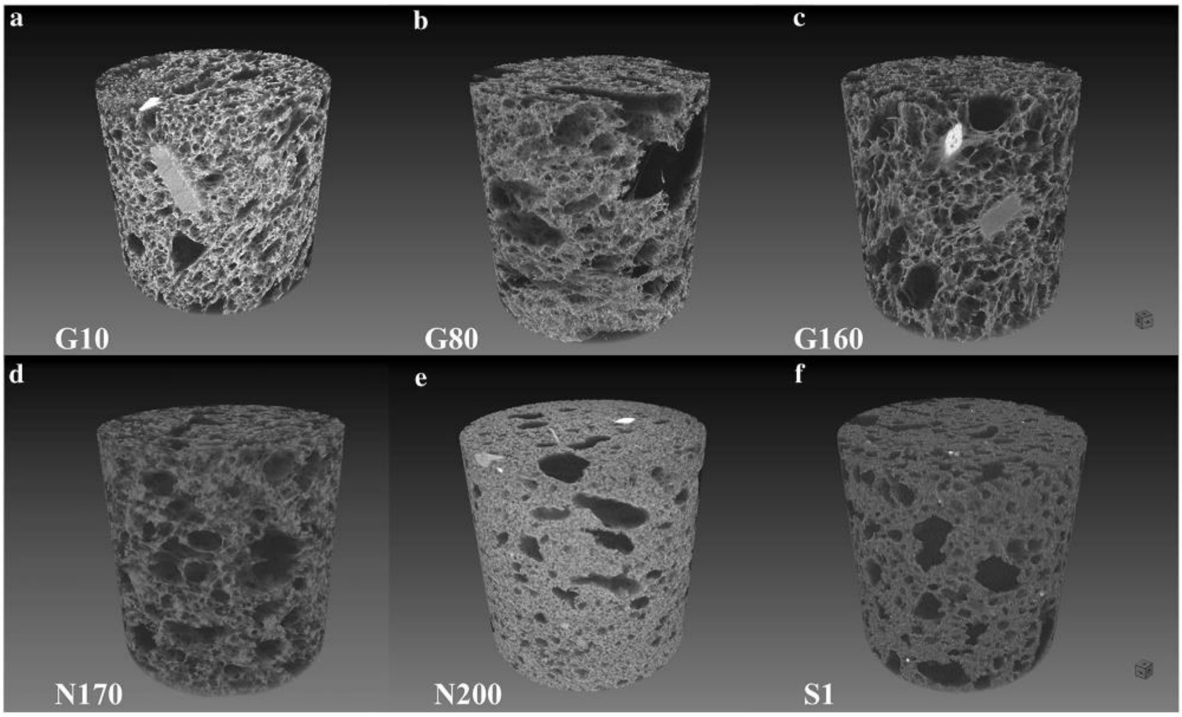

Figure 2.5 Volume rendering showing 3D microstructures of Pomici di Base trachytic (A-D) and latitic-shoshonitic (E-F) rocks. Cylinder diameter: 1000µm. Vesicles are black, melt/feldspars/pyroxenes are grey and oxides are white. The white numbers refer to the sample numbers (Pappalardo et al., 2018).

Bubble textures can reveal a wealth of information about a bubbles behaviour however there is currently a limited understanding on how bubble resorption presents itself in natural samples. In the next section, the process of bubble resorption will be outlined alongside the current evidence.

2.3 Bubble Resorption

2.3.1 The Understood Process

Resorption is driven by an increase in solubility of water due to a temperature decrease and/or a pressure increase. An increase in H_2O solubility causes the H_2O at the bubble wall to increase above the concentration of H_2O dissolved in the melt, and so H_2O diffuses from the bubble down the concentration gradient back into the melt (Watkins et al., 2012; McIntosh, 2013; McIntosh et al., 2014; Allabar et al., 2020a). Resorption varies depending on specific pressure-temperature conditions and the magmatic conditions as discussed in the introduction. It is an important process when considering volcanic history and when looking at a variety of experimental scenarios and natural products. Resorption can influence final bubble size and in turn any experimental conclusions that are drawn from analysing bubble textures. There are currently only a few studies which find evidence for and/or consider resorption (Watkins et al., 2012; Carey et al., 2013; McIntosh et al., 2014; Allabar et al., 2020a).

The modelling of continuous experimental data to quantify a change in bubble size against experimental parameters allows for a better understanding of resorption. Bubble size is evaluated by measuring ϕ which increases for a growing bubble. Burgisser and Gardner (2005) experiments, that have been unknowingly overprinted by resorption, are used in this thesis to investigate how easy it is for bubbles to resorb in magmas in experimental situations and how this may be quantified.

2.3.2 Textural Evidence for Resorption

Evidence for resorption has been provided with textural and geochemical data. Allabar et al. (2020a) and Carey et al. (2013) both use textural analysis to confirm resorption has taken place.

Allabar et al. (2020a) quantifies the extent to which vesicle shrinkage occurs during decompression experiments. A series of decompression experiments from Allabar and Nowak (2018) and Allabar et al. (2020b) are used to quantify resorption in Vesuvius phonolitic melts (VAD79). The Allabar et al. (2020a) study uses many aspects that the Coumans et al. (2020) numerical model is based on including equations for solubility, EOS, and viscosity. It is also acknowledged that vesicle shrinkage can only be analysed when the conditions prior to quench are known and properties such as porosity can be calculated. Resorption is quantified for measuring water content, using FTIR micro-spectroscopy and Raman micro-spectroscopy (RMS) observations.

RMS allows for the H_2O concentration between two bubbles to be measured and for the samples collected by Allabar et al. (2020a) a clear H_2O resorption halo can be seen around both bubbles. Distance profiles are measured between two bubbles under the surface and the H_2O concentration plotted along the profile. Allabar et al. (2020a) also provides experimental guidance on what the impact of different experimental quench techniques may have on bubble resorption (Allabar et al., 2020a; figure 2.6).

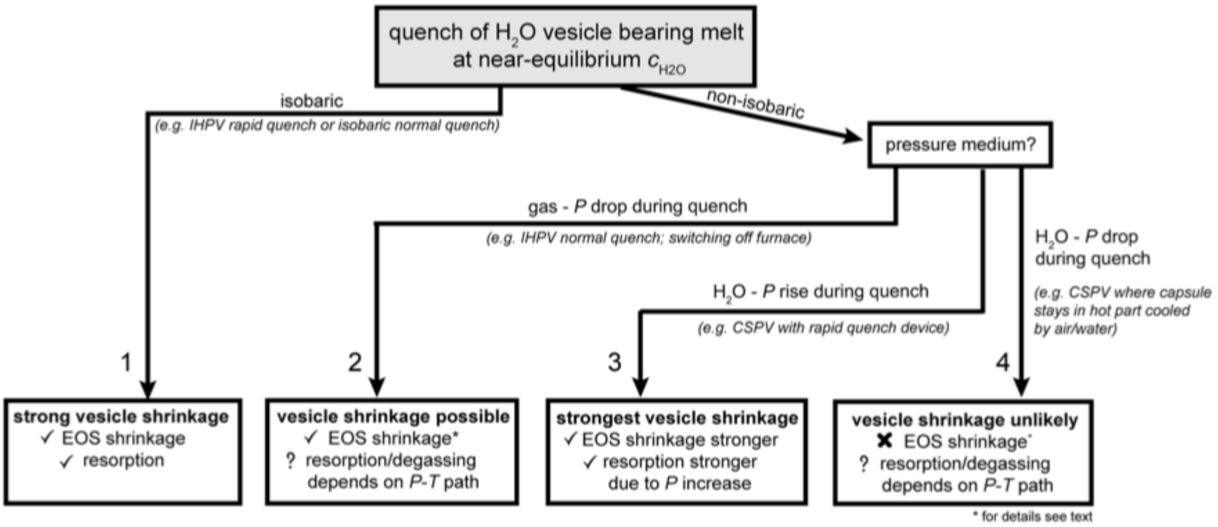

Figure 2.6 Experimental guidance by Allabar et al. (2020a) on conducting decompression experiments. Depending on the experimental pathway chosen, therefore, different possibilities for bubble resorption.

The Allabar et al. (2020a) study highlights the impact resorption has on experimental results, with the degree of resorption varying with experimental technique and quench style. However, additionally there is a need to provide detailed guidance on the correct experimental conditions to use to minimise resorption, which this thesis aims to produce.

In many ways the Allabar et al. (2020a) study is like the Coumans et al. (2020) study. The same resorption problem is addressed by both studies, and both manage to quantify any subsequent resorption results. With Allabar et al. (2020a) doing it via calculations for a large data set while Coumans et al. (2020) achieve it via a numerical model. A numerical model makes for faster generation of results and allows for a look at a broader range of compositions and scenarios simultaneously.

Textural evidence for resorption is also found by Carey et al. (2013) (figure 2.7). When considering the importance of resorption in experimental studies this can be extrapolated out to also consider the importance of resorption in natural scenarios such as indirect evidence found by Carey et al. (2013) in basaltic clasts from an eruption of the Halema'uma'u lava lake. The amount of bubble resorption is inferred from vesicle populations where large vesicles, surrounded by a halo of small vesicles, indicates a change in H_2O concentration in the large vesicles.

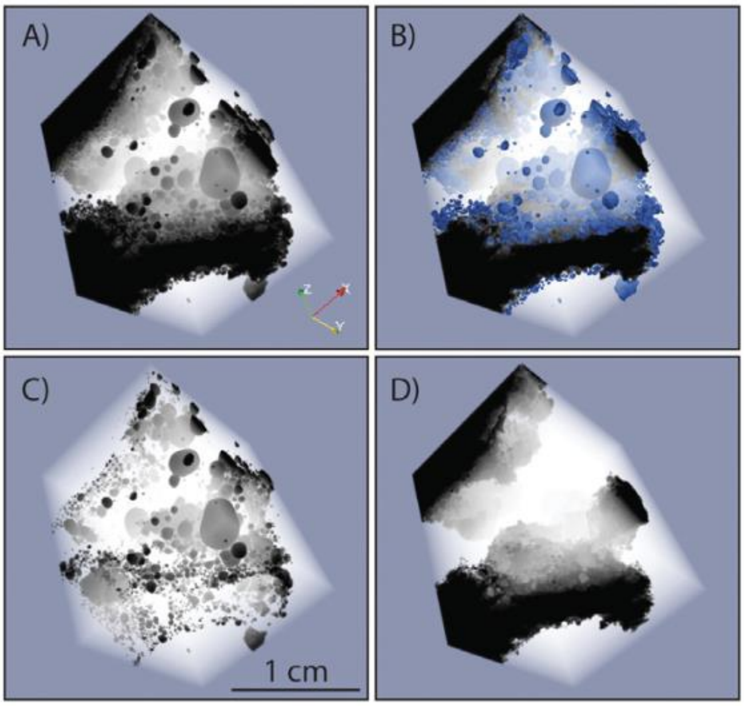

Figure 2.7 X-ray microtomographic renderings of segmented images from a clast erupted from the Halema'uma'u lava lake in 2008. In each image, haloes containing a high number of small, isolated round bubbles are used to indicate bubble resorption. A. 3D rendering where bubbles are black and glass is translucent, B. small bubble population. The blue bubbles are bubbles with a diameter of 180μm or less, C. spatial distribution of small bubbles within the volume, D. the large bubbles within the volume (Carey et al., 2013).

2.3.3 Geochemical Evidence for Resorption

McIntosh et al. (2014) and Watkins et al. (2012) both use geochemical results as evidence for changing bubble size. Despite resorption being an understood process, it has been difficult to find evidence of resorption occurring, as samples need to be analysed during the quench process. Watkins et al. (2012) generate a model on volatile concentration based on natural samples from the Mono Craters in California. H_2O and CO_2 concentrations in obsidian pyroclasts are analysed. By finding samples which have large, undeformed, and isolated bubbles that are preserved during the eruption this study represents one of the first studies where resorption is found to be occurring in natural samples, based on geochemical results with timescales being defined using model results. H_2O is enriched in glass surrounding the bubbles, indicated that there is an increase in H_2O solubility and resorption of bubbles just prior to the eruption. These observations are based on H_2O concentration profiles which provide evidence that the bubbles and surrounding melt are not in equilibrium with respect to H_2O at the time of quench. Possible resorption can be linked to magma cooling at depth (Liu et al., 2005), multiple episodes of pressure changes (Gonnermann and Manga, 2003; Tuffen et al., 2003) or an increase in CO_2 content (Rust et al., 2004). This represents a case where quantifying resorption can be used to infer eruption conditions.

The H_2O concentration profiles of the samples are used to quantify a timescale for pressure changes for a model of isothermal, diffusion-controlled bubble resorption (Watkins et al., 2012; figure 2.8). An expected concentration profile for a resorbing bubble aligns with the data collected. This model holds similarities to the Coumans et al. (2020) numerical model used in this study. The model proposed by Watkins et al. (2012) neglects the effects of CO_2 concentration on water solubility and assumes that water diffusion begins after compression of the bubble, based on pressure increase, and ceases upon quench. However, as the samples are not based on decompression experiments, but natural samples, the exact sample conditions are unknown and not applicable to be tested using the Coumans et al. (2020) model.

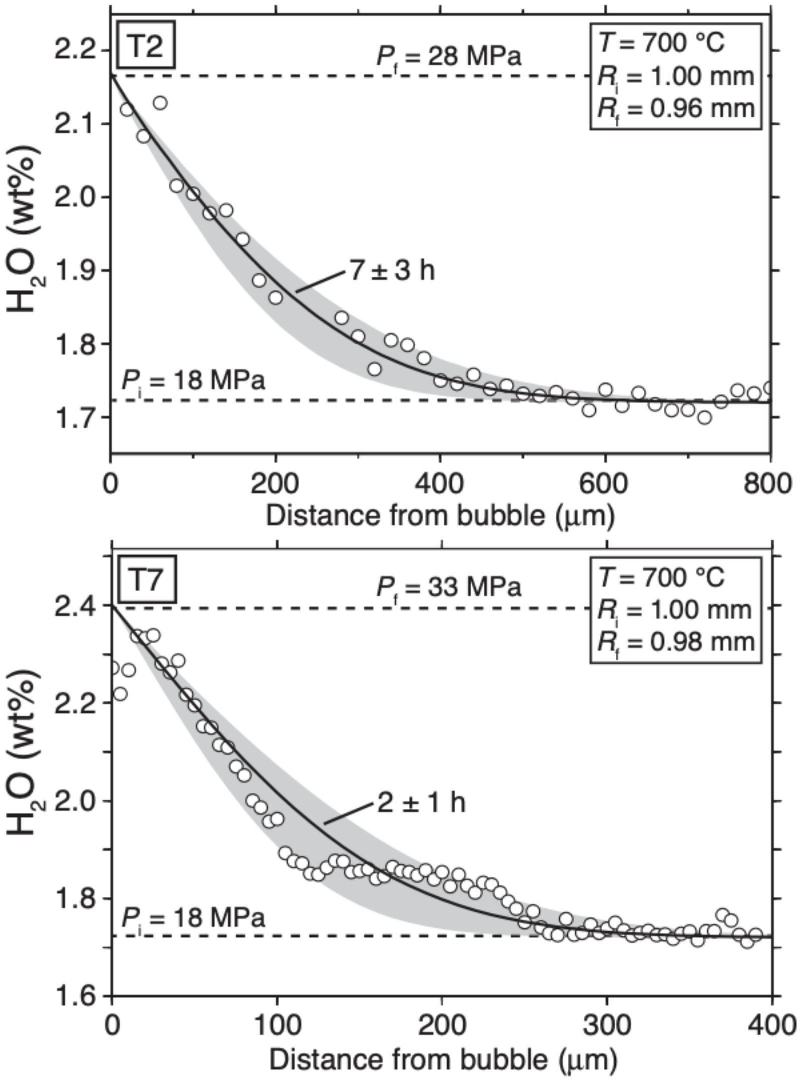

Figure 2.8 Outcome from a study by Watkins et al. 2012. Model results for diffusion of water away from resorbing bubbles. Decreasing H_2O (wt.%) away from the bubble indicates the migration of water from the bubble and into the melt. The comparison of the top and bottom plot indicates that bubble A is resorbing for 2-7hr prior to eruption.

The McIntosh et al. (2014) study measures water distribution around vesicles in experimentally vesiculated samples created by Burgisser and Gardner (2005) and several unpublished studies by Schipper, C.J. and Larsen, J.F. The sample characteristics are quantified within the study.

Secondary Ion Mass-Spectrometry (SIMS)-BSEM and FTIR imaging are used to quantify resorption rather than a numerical model. Infilled vesicles are revealed by grinding down the exposed surfaces and SIMDS total water (H_2O_t) data is used to calibrate BSEM images to extract quantitative H_2O data at a high spatial resolution. Resorption is seen in images and when plotting H_2O profiles (McIntosh et al., 2014; figure 2.9).

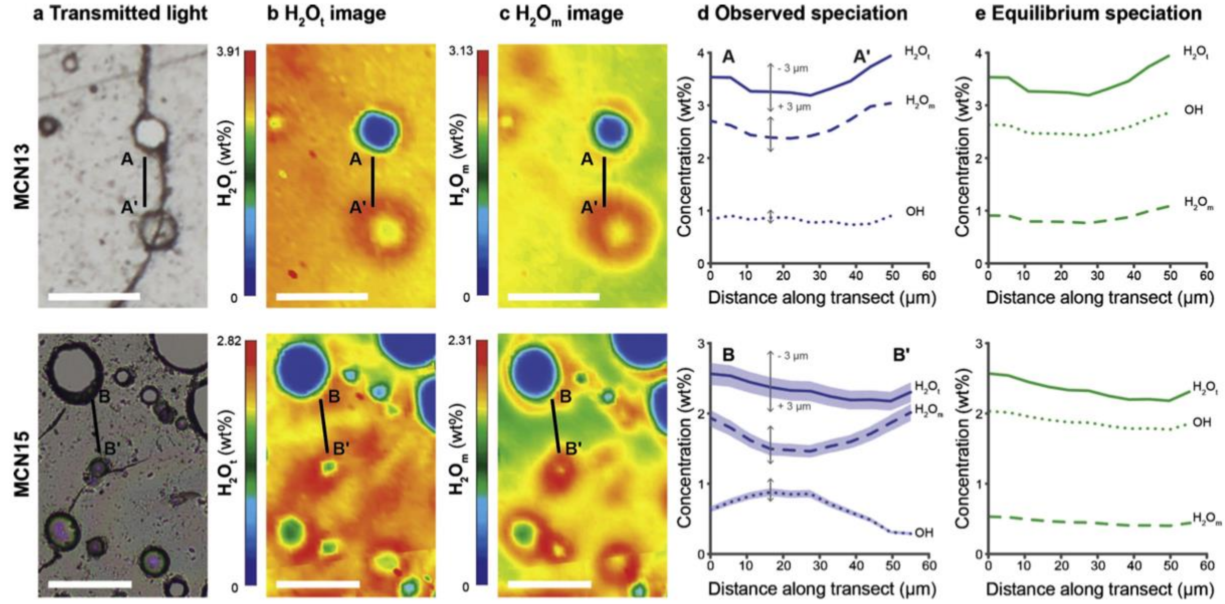

Figure 2.9 Images from McIntosh et al. (2014). Water speciation distributions for samples by Larsen, J.F. a) Transmitted light image of the sample, b) Total water (H_2O_t), and c) Molecular water (H_2O_m) distributions obtained by FTIR imaging. White bar is 100µm. Both samples show enrichment in H_2O_m and OH profiles for the observed H_2O_t profiles in d) assuming equilibrium speciation at the experimental run temperature.

H_2O concentration increases towards vesicles, indicating that water is resorbing from bubbles during cooling while textural evidence suggests that resorption occurs before the melt solidifies. This textural evidence includes samples containing cracks with thin water-rich margins, indicating that some hydration occurs. The cracks also terminate in the outer part of the resorption halo. However, what can be said about resorption being used to analyse eruption conditions?

The McIntosh et al. (2014) results challenge the conclusions proposed by Watkins et al. (2012) – that resorption indicates fluctuating pressure conditions. Based on experimental observations, McIntosh et al. (2014) indicate that temperature also needs to be considered. The Coumans et al. (2020) numerical model directly references the McIntosh et al. (2014) study to support the notion that studies that use the final vesicle size of experimental or natural samples to make inferences about bubble growth, degassing mechanisms or eruptive processes may need to be revised. Since McIntosh et al. (2014) the study of resorption has continued to evolve.

Although resorption has been quantified in the past, this thesis will expand upon previous observations to generate a deeper understanding of what influences resorption and to what degree. These results will be applicable to a variety of different studies of the same rhyolitic composition.

2.4 Decompression Experiments

Decompression experiments are used to study the growth of bubbles, mimicking what takes place in a volcanic conduit under different pressure-temperature conditions. The parameters of a decompression experiment are required inputs to the Coumans et al. (2020) numerical model. Theoretically any composition and conditions are applicable if the correct solubility, EOS, viscosity, and diffusivity functions are used.

The aim of the Coumans et al. (2020) model, to examine if bubble resorption is happening, does not require knowledge of resorption to be a pre-requisite. The model aims to look at studies which do not consider resorption but may have results that have been overprinted by it. The numerical model requires all pre-experimental conditions as inputs as well as stochastic variables such as N_b. This stochastic variable is usually published in the results for experimental studies, so it is likely that experiments must be completed before being applied to the model. However, it is rare to find a study which describes all the required variables of the model, and each study needs to be treated individually. Details of ideal studies for the numerical model are given below.

Larsen and Gardner (2000) study the interaction between bubbles in rhyolitic melts (from Little Glass Butte, OR, USA) which are experimentally decompressed between 80 – 200MPa. Bubble distances are measured, and size reduction is attributed to concentration gradients in the melt. Experimental conditions are supplied in table format which can be input into the Coumans et al. (2020) numerical model with ease. Larsen and Gardner (2000) make a distinction between 'hydration' bubbles and 'decompression' bubbles – this distinction is rarely made in other studies (Larsen and Gardner, 2000; figure 2.10). 'Hydration' bubbles refer to bubbles in the relevant experiments that use powders that are present before pressure is released (Gardner et al., 1999). Thus, experimental data such as porosity are provided for both bubble types whereas in other studies these bubble types may be grouped together and considered as only decompression bubbles.

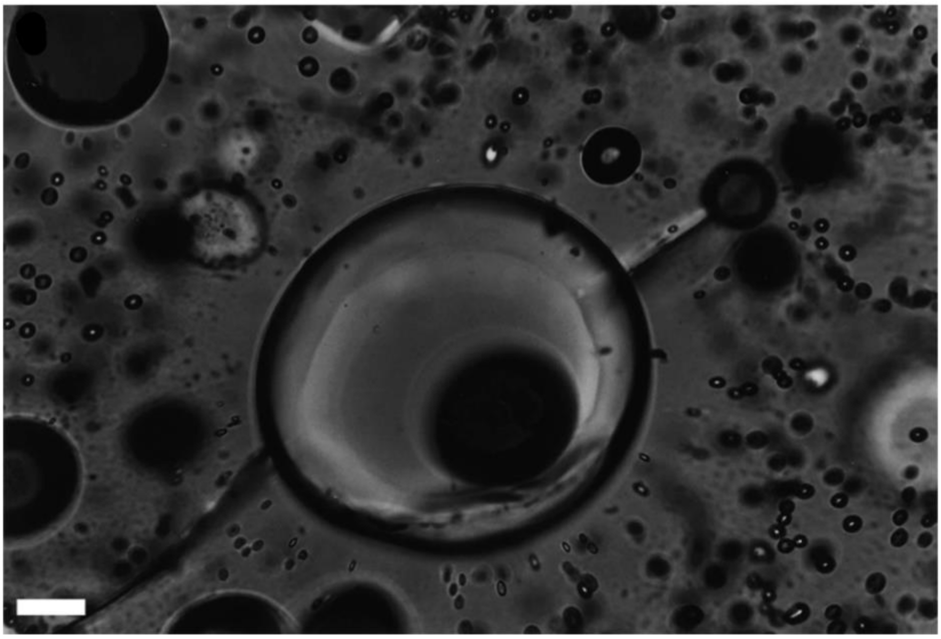

Figure 2.10 Images bubble by Larsen and Gardner (2000). Hydration bubbles in samples illustrating the environment surrounding large hydration bubbles. Around them are the elongation of much smaller decompression bubbles and a zone of fewer decompression bubbles next to the surfaces of the hydration bubbles. These bubbles appear in a similar fashion to other samples that have shown evidence for resorption (Watkins et al., 2012; Allabar et al., 2020a). The scale bar is 20μm.

Larsen and Gardner (2000) conclude that concentration gradients in the melt are responsible for bubble size reduction and depleted zones around them, even for the lowest of pressures, indicating that size distribution of small bubbles may be affected by concentration gradients in the depleted melt shell, surrounding large bubbles. As with most volcanological studies the decompression results are used to suggest processes in real world scenarios.

Larsen and Gardner (2000) state that large bubbles present in an ascending magma, prior to a subsequent nucleation event, can affect the growth of the smaller bubble population occurring within the depleted melt shell of the larger bubbles and produce a bimodal vesicle size distribution (VSD). VSD's in natural samples are often used to determine physical aspects of explosive eruptions with the distributions being interpreted as a product of continuous bubble nucleation (Blower et al., 2001a). It is important to understand the N_b of a melt to produce the final textures observed in the quenched pumice clasts. These conclusions may be altered when considering the full bubble growth path and subsequent resorption.

Decompression experiments usually take place using an externally heated argon pressure vessel with a rapid quench set up. The rapid quench set up captures the resorption process in action, such as in Marxer et al. (2015). In this set of experiments, H_2O-bearing phonolitic melts are decompressed at a super-liquidus temperature of $1323K$.

Marxer et al. (2015) uses a similar process to Larsen and Gardner (2000) and creates a fused powder mixture however Marxer does not consider 'hydration' bubbles, so it is not clear if they take them into account. These discrepancies between decompression experiments need to be normalised when used in the Coumans et al. (2020) numerical model. Marxer et al. (2015) reference McIntosh et al. (2014) in their study and state that significant H_2O concentration gradients around the bubbles are not detected (Marxer and Nowak, 2013) – so do not signify the process of resorption (Marxer et al., 2015; figure 2.11). Marxer et al. (2015) proposes that any change in H_2O gradient is due to a decrease of the molar volume of the exsolved water and the excess H_2O in the capsule during rapid quench. However, putting this experiment into the numerical model would be able to validate these findings and quantify if any resorption does occur.

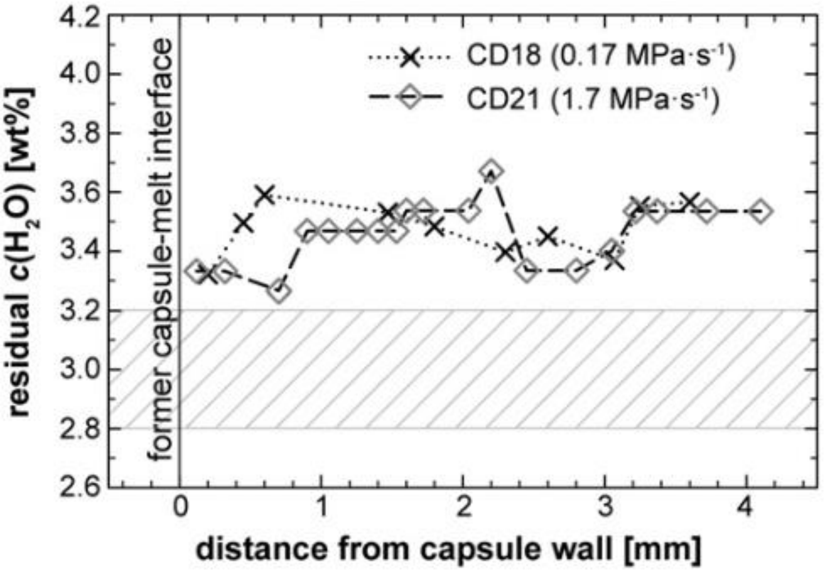

Figure 2.11 Results from Marxer et al., 2015. H_2O concentration distance profiles by FTIR measurements. The shaded area corresponds to the solubility at the final pressure (± analytical error). This trend does not display severe concentration gradients.

Another study applicable to the numerical model are 3 series of decompression experiments performed by Mourtada-Bonnefoi and Laporte (2004) with the aim of characterising the effect of ascent rates on the kinetics of bubble nucleation in a rhyolitic magma (Mourtada-Bonnefoi and Laporte, 2004; figure 2.12). Kinetics of bubble nucleation controls two parameters essential to determining eruption characteristics: critical nucleation pressure and N_b.

The samples used are crystal-free which is ideal for the Coumans et al. (2020) numerical model as a sufficient fraction of crystals present would otherwise interfere with the physics of the numerical model. The study also provides the required functions for the model parameters such as the composition quantities – a rhyolitic from Güney Dagi, Turkey.

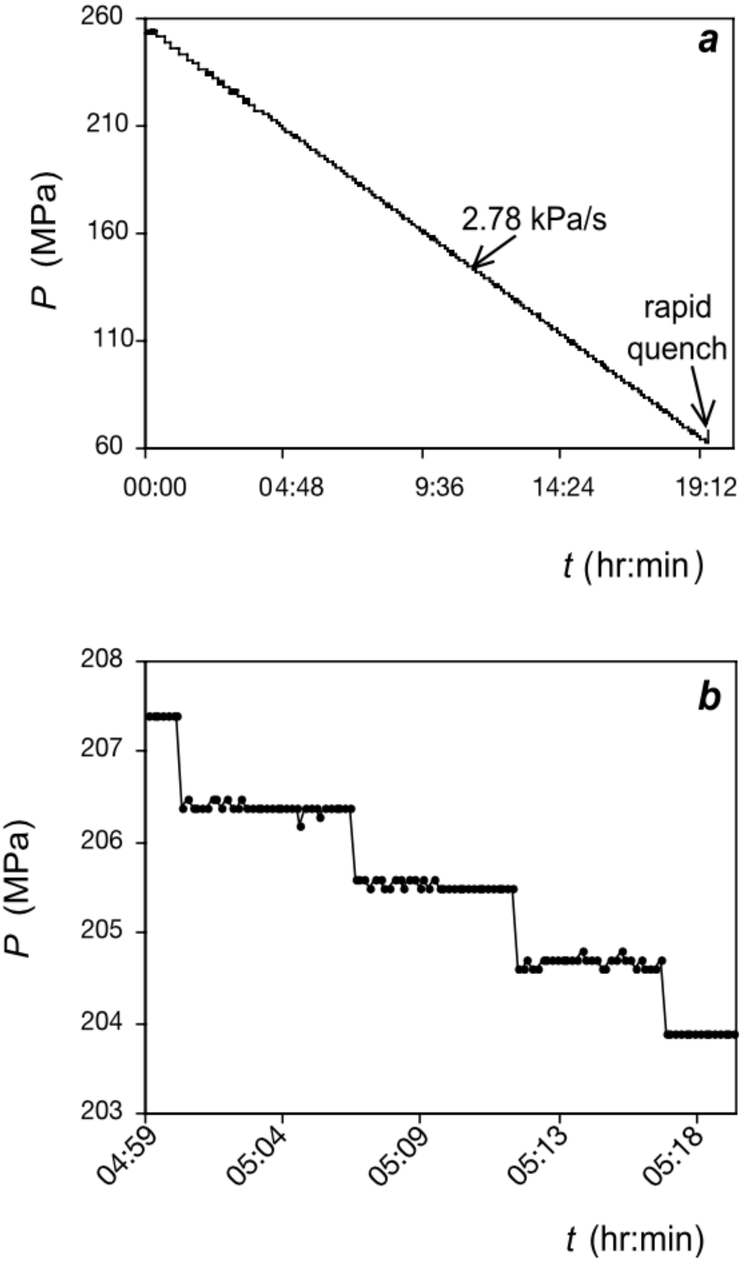

Figure 2.12 Experimental process of Mourtada-Bonnefoi and Laporte (2004). Illustration of the decompression device set up and its stepwise decompression. Stepwise decompression is how a linear rate can be generated when the steps are extended out into a single line.

Mourtada-Bonnefoi and Laporte (2004) make conclusions based on the decompression results and subsequent textural analysis (Mourtada-Bonnefoi and Laporte, 2004; figure 2.13). The textural analysis has the potential to be influenced by resorption and the study does measure water content so can be analysed further. The conclusion made by Mourtada-Bonnefoi and Laporte (2004) is that the values of N_b in silicic pumices may be due to two successive nucleation events.

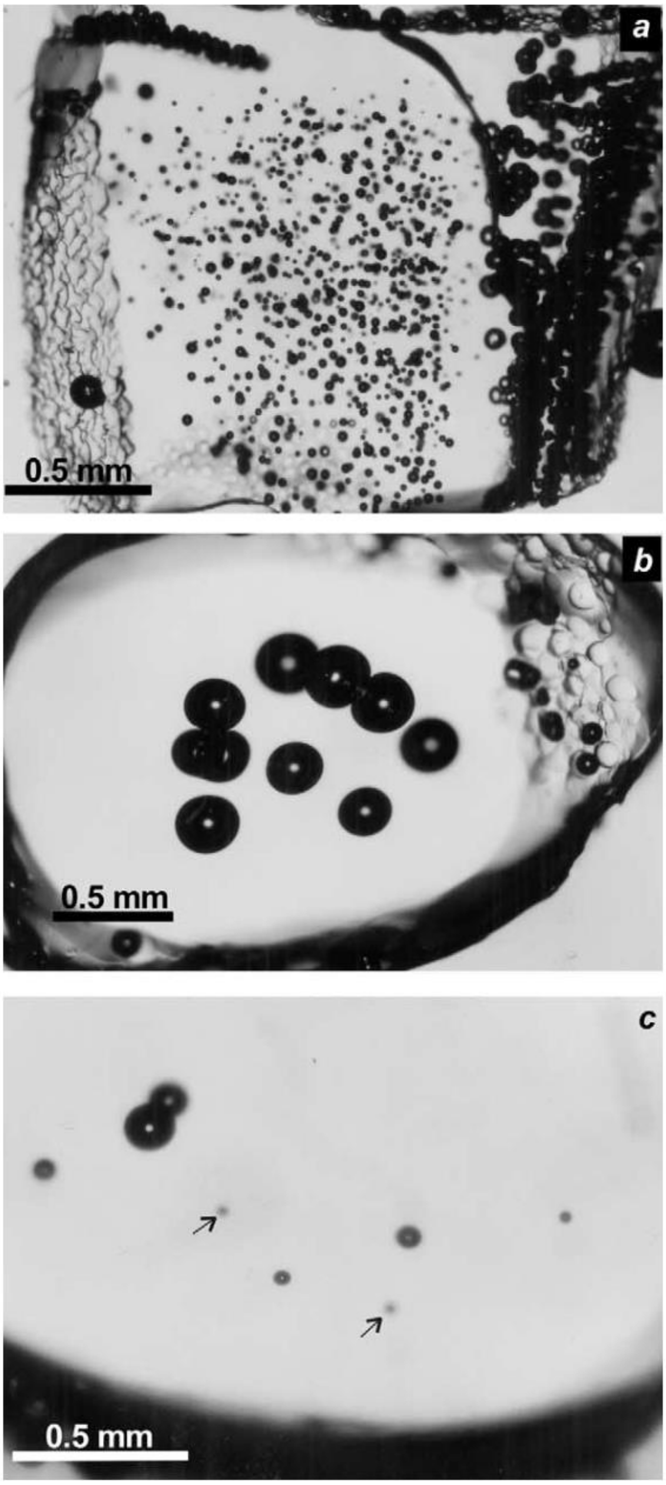

Figure 2.13 Imaged bubbles from Mourtada-Bonnefoi and Laporte (2004). Taken from cores of homogeneous bubble nucleation. Bubbly fractures can be seen in a) and are related to fractures that developed in the glass cylinders at the beginning of the experiment.

The above studies make conclusions based on sample textures and relevant functions such as solubility (Mourtada-Bonnefoi and Laporte, 2004) are provided. Where a function is not provided, for instance a diffusion function is not provided by Marxer et al. (2015), an appropriate function based on similar pressure and temperature conditions can be used. However, the intricacies of each experiment need to be considered and any appropriate adjustments made.

2.5 Burgisser and Gardner (2005)

2.5.1 Experimental Set-Up

McIntosh et al. (2014) carry out an investigation into several different decompression studies and find that they all show evidence for resorption. The Burgisser and Gardner (2005) study involves an experimental set up which provides all the necessary parameters and functions to be utilised by the Coumans et al. (2020) numerical model and thus this study. Burgisser and Gardner (2005) explore the relationship between bubble growth and decompression rate and how this process links to volcanic conduit dynamics, in particular two behaviours: degassing and permeability in magmas.

Hydrated rhyolitic glass from the Panum Crater Dome (PCD) is decompressed at high pressure ($60 - 150MPa$) and temperature ($573 - 1098K$) using an externally heated pressure vessel fitted with a rapid quench attachment (Suzuki et al., 2009; figure 2.14). The study follows a typical decompression set up for 22 'ABG' samples.

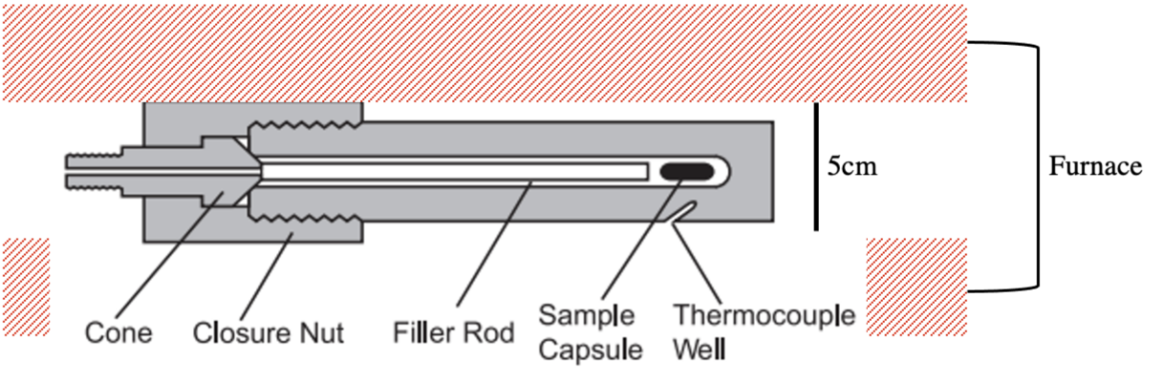

Figure 2.14 Cross section of a standard externally heated pressure vessel. The placement of the furnace is shown. The scale is indicated. The rapid quench attachment is not shown (Suzuki et al., 2009; Tuttle, 1948).

For 5 days the rhyolitic samples are held at $1098K$ and $150MPa$ to saturate with water, this creates a bubble-free hydrated sample. Following the 5-day hydration, samples are decompressed instantaneously to $100MPa$ and held for 15 minutes, creating a bubble population in equilibrium with the melt that is not influenced by nucleation kinetics. This 15-minute stage is essential to creating samples which grow bubbles at the right time and only after equilibrium has been reached. Burgisser and Gardner (2005) do not elaborate on why 15 minutes is the ideal time for an equilibrium population of bubbles to form. As the decompression rate is instantaneous, these 15 minutes must allow for the bubble population to develop before nucleation kinetics take effect. Gardner et al. (2018) state that there is a characteristic timescale over which the H_2O content of the particles approach equilibrium with the H_2O solubility at experimental conditions. This hydration timescale, λ_d, is:

$$\lambda_d = \frac{\bar{R}^2}{D}, \tag{1}$$

where $\bar{R}$ is the mean particle radius and D is the diffusivity of H_2O in the silicate melt. Equation (1) is used to estimate whether a particle is expected to be fully hydrated by comparing the hydration timescale with the time, t, for which the particle is held at experimental conditions.

It is possible to use the Coumans et al. (2020) numerical model to demonstrate if equilibrium bubbles are able to form before 15 minutes. For details on how the model works and an explanation on the figures displayed below, see section 3.3 and chapter 4. In figure 2.15, the bubble reaches does not reach equilibrium by 900 seconds, evidence that more time should have been allowed for equilibrium conditions to be reached.

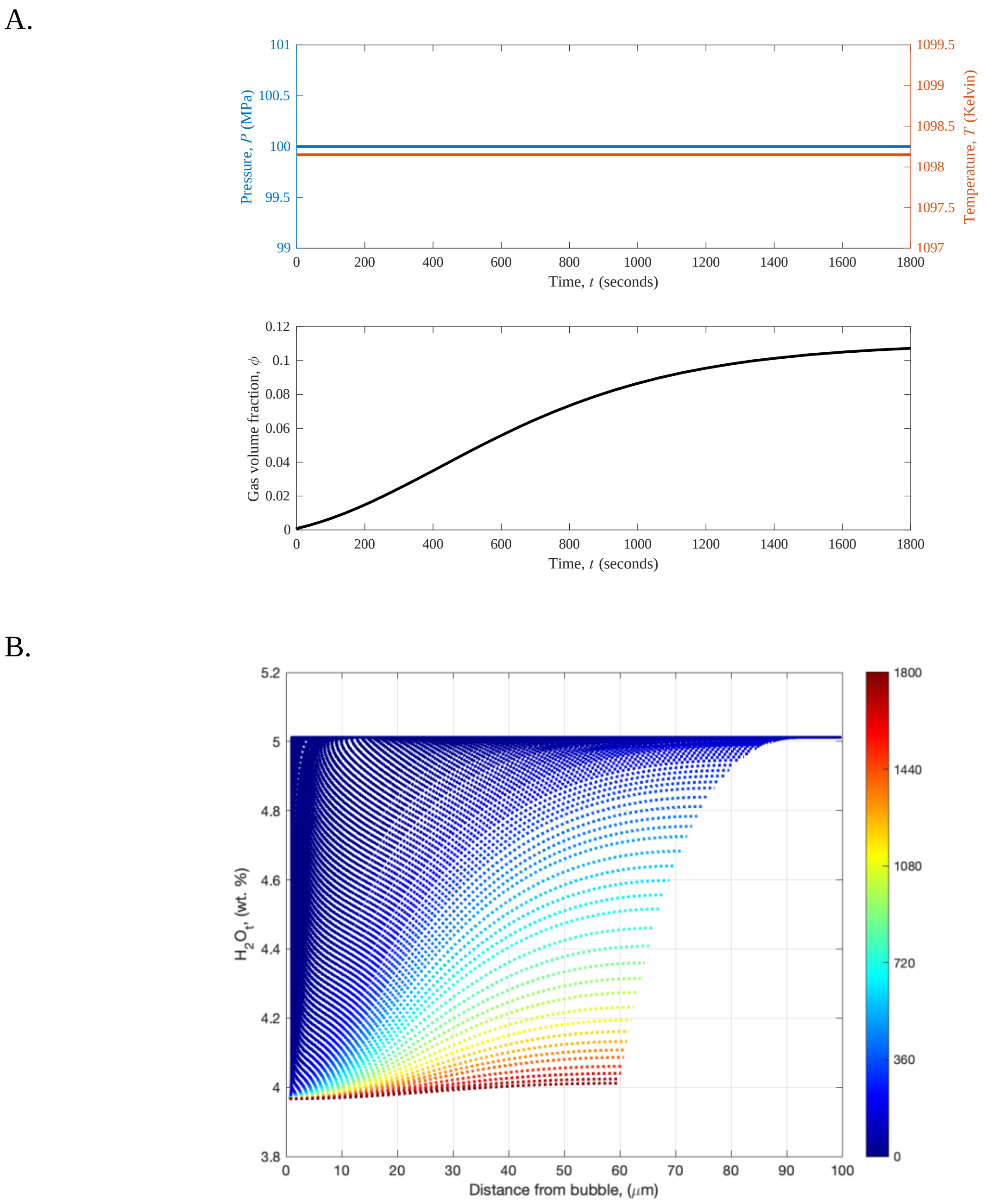

Figure 2.15 The Coumans et al. (2020) model outputs. A. The temperature and pressure pathways on the experimental run and the evolution of the bubble growth (represented by gas volume fraction). B. The H_2O_t content of the bubble. The bubble has not reached equilibrium by 900 seconds.

A final decompression step takes place for all samples, except ABG1 which is held at equilibrium, as a form of closed degassing (Burgisser and Gardner, 2005; figure 2.15). ABG1 acts as a control sample to validate the decompression experiment and the subsequent results. This decompression experiment allows the bubbles to grow and shrink, creating the experimental samples used in the McIntosh et al. (2014) study (experimental conditions seen in table 2.1). Quenching is achieved by lowering the samples into the water-cooled based of the sample vessel after the final decompression step. This allows the bubble process to be ‘frozen’ and analysed post-experiment.

Sample	T_{exp} (^{o}C)	P_{syn} (MPa)	P_i (MPa)	P_f (MPa)	$dPdt$ (MPas^{-1})
ABG1	825	150	100	100	N/A
ABG2	825	150	100	60	0.1
ABG6	825	150	100	80	0.1
ABG14	825	150	100	80	0.5
ABG15	825	150	100	60	0.5

Table 2.1 Details of the experimental conditions for the Burgisser and Gardner (2005) samples. T_0 *is initial temperature,* P_{syn} *is pressure of sample synthesis,* P_i *is intermediate pressure,* P_f *is final pressure and* $dPdt$ *is decompression rate (table simplified from McIntosh et al., 2014).*

Burgisser and Gardner (2005) assume that the samples quench instantaneously however they must cool over a finite time interval. Due to conductive limits, it is arguably impossible to achieve an instantaneous quenching. The effect of the cooling rate on each sample is investigated in further detail in chapters 4 and 6. Sample ABG1 is used as an equilibrium indicator as it is decompressed from $150MPa$ to $100MPa$ to ensure a bubble population at equilibrium and is not decompressed further so does not incur bubble growth and resorption, except when temperature drops.

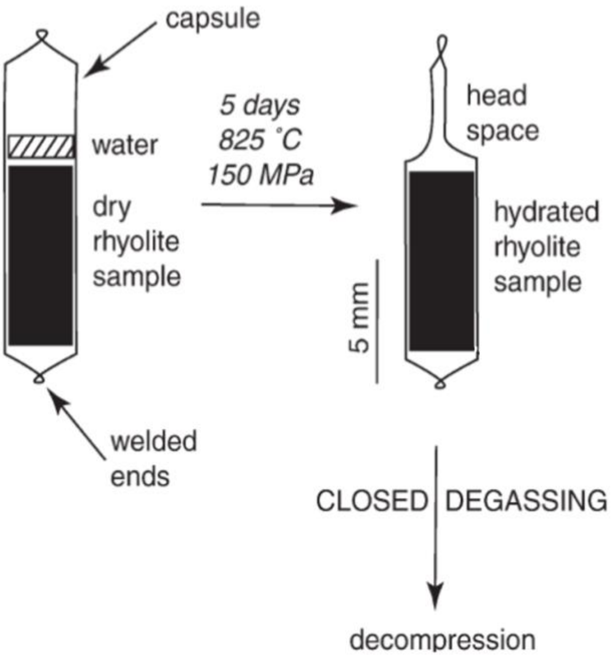

Figure 2.16 The experimental set up for closed degassing. In this thesis, closed degassing will be the focus as it involves the decompression of samples with water present, allowing for resorption to take place.

Using thin section images, the bubble size distribution (BSD), N_b and porosities are measured and used to make conclusions based on the parametric trends. Diameters of the bubbles are measured using digital images acquired in transmitted light. While N_b is calculated based on BSD observations. Results from Burgisser and Gardner (2005) are used by McIntosh et al. (2014) to look at water distributions around vesicles, with high spatial resolution. McIntosh et al. (2014) finds evidence for resorption in these samples and one of the goals of this thesis is to quantify the amount of resorption taking place.

2.5.2 Findings

Porosity levels in this study are important as it links to magma permeability and a transition to an effusive eruption. If magma can become permeable and lose part or all of its gas without fragmenting, it reduces its porosity, thus limited further acceleration and possibly leading to an effusive eruption (Eichelberger et al., 1986).

By looking at how much porosities of samples deviate from the porosities at equilibrium, two distinct disequilibrium bubble growth regimes are defined, and these regimes are used to divide the path of bubble growth within the conduit (Burgisser and Gardner, 2005; figure 2.16). These regimes are split into a slow growth rate, a fast growth rate and an equilibrium regime. The first disequilibrium regime of degassing is based on the findings that equilibrium bubble growth occurs when the decompression rate is slower than $0.1 MPas^{-1}$ and porosity increasingly deviates from equilibrium as pressure decreases but the magnitude of deviation does not change with decompression rate. Higher rates cause porosity to deviate rapidly from equilibrium. In this regime the faster pressure decreases, the faster the bubbles grow.

The assignment of these regimes is used to provide an indirect measure of the amount of water super-saturation, because super-saturation increases with the difference between equilibrium porosity and sample porosity.

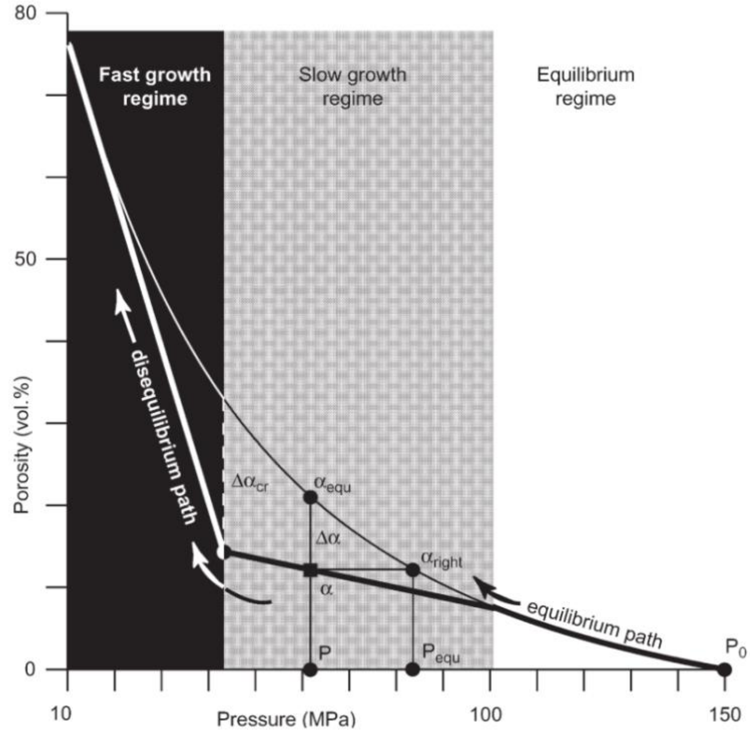

Figure 2.17 The division into the different decompression regimes, as designated by Burgisser and Gardner (2005), α and P are porosity and pressure at the point of interest, α_{equ} is the equilibrium porosity at a given P, $\Delta\alpha$ is the difference between α_{equ} and α, α_{right} and P_{equ} are the respective equilibrium porosity and pressure at a given α and $\Delta\alpha_{cr}$ corresponds to the critical super-saturation that delimits the fact and slow growth regimes.

Burgisser and Gardner (2005) use these results to support the established relationship between super-saturation and growth: the amount of excess water drives bubble growth because the rate of water diffusion into bubbles increases with the concentration gradient between the melt and the bubble (Sparks, 1978; Proussevitch and Sahagian, 1998). However, in this understanding, the additional process of resorption is not considered.

Using the designated disequilibrium and equilibrium regimes, the growth of bubbles caused by a constant decompression rate are approximated by Burgisser and Gardner (2005). What would happen to these disequilibrium regimes when factoring in the process of resorption?

2.5.3 Application to the Coumans et al. (2020) Model

Burgisser and Gardner (2005) use textural evidence to support their conclusions which are used to support the idea of separate disequilibrium regimes. These regimes are based on porosity measurements from samples that undergo decompression.

There is also a link made to the natural environment which the results of the Burgisser and Gardner (2005) study support. It must be assessed whether fragmentation criterion controlled by flow conditions, occurs at different porosities. This can be done by looking at the regimes defined (Burgisser and Gardner, 2005). Links to the natural environment should be made for a study to be used in the Coumans et al. (2020) numerical model as resorption results have the potential to influence any conclusions and links to the natural environment that are made.

Based on the disequilibrium regimes, Burgisser and Gardner (2005) conclude that fragmentation depth is highly sensitive to the rate at which the different processes that control degassing occur in the conduit (Burgisser and Gardner, 2005; figure 2.17). Knowing how much resorption occurs can constrain these conditions.

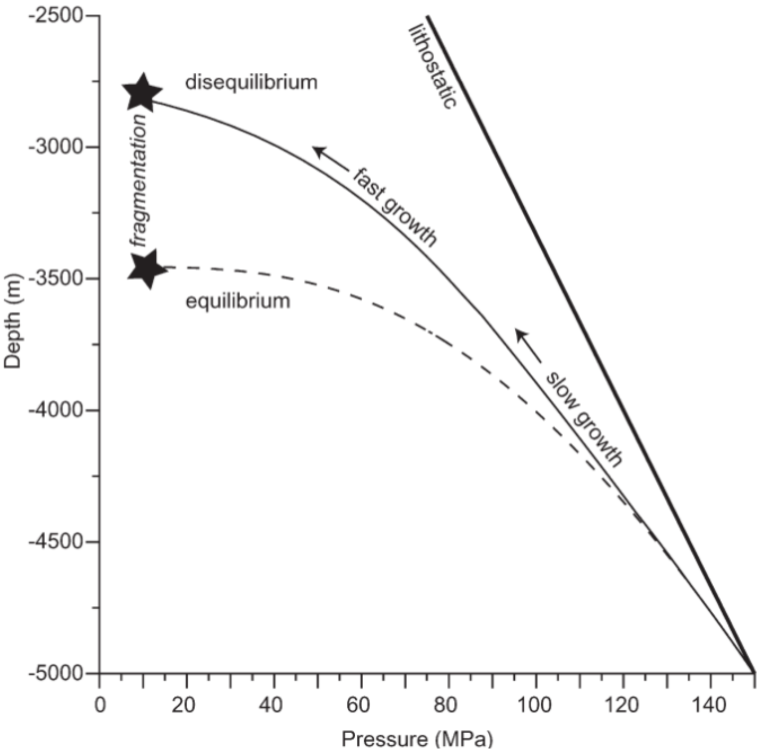

Figure 2.18 The simulation used by Burgisser and Gardner (2005) involves the comparison of pressure-depth variations of 1D conduit flow simulations with and without equilibrium degassing. The stars represent fragmentation depths for each run/ As magma rises in a steady state in the conduit, its porosity increases and the run stops when the magma reaches fragmentation at a fixed porosity of 64vol%.

With these concluding statements considered, this study is applicable to the numerical model. McIntosh et al. (2014) choose this study to investigate resorption because the Burgisser and Gardner (2005) experiments are manufactured under controlled pressure and temperature conditions and the experiments are designed to produce bubble populations with either equilibrium or bubble growth profiles.

2.6 Conclusion

Bubble growth has been a topic of interest for decades with models being used to explain conduit processes and to describe the natural phenomena seen. Resorption only recently became of interest, especially its potential impact on past research.

Decompression experiments are used to mirror the processes that occur in the natural world and by looking at past decompression studies; how bubble growth is measured and understood is evaluated. Burgisser and Gardner (2005) investigate bubble growth and its influence on effusive eruptions however their results could have been overprinted by resorption. This highlights the importance of using the Coumans et al. (2020) numerical model to assess this study and if resorption does occur and if so, to what extent.

Several questions have been posed in this chapter; this thesis aims to answer these questions via various means of numerical investigation. The Burgisser and Gardner (2005) study is used as a roadmap for looking into how resorption is influenced and its impact on decompression studies.

3. A Theoretical Understanding

3.1 Introduction

This chapter introduces the background necessary to understand how the Coumans et al. (2020) model works. The implementation comprises of three components: 1) the script the user mainly interacts with where data is input; 2) a script which contains all the necessary functions for solubility, viscosity, composition, diffusivity, and equation of station (EOS), and 3) the script equipped to carry out the relevant modelling. The model is designed to be easily adapted for different research aims by allowing editing in all three scripts and including descriptive comments throughout the code.

In this chapter, I give an overview of the structure and mathematical basis of the model. I also add detail of the modifications and additions that are made to add specific functionality required for this study, including a newton cooling path, and calculations of equilibrium starting conditions (see section 3.4).

Several features are added to the model during this study including an additional newton cooling path and a function to calculate equilibrium bubble conditions which is necessary to compute initial conditions for the Burgisser and Gardner (2005) samples.

3.2 Model Theory

The shell model (section 2.2) from Proussevitch et al. (1993) assumes that the bubbly melt can be idealised as a collection of identical single-bubble-melt-shell units, and hence the evolution of the physical properties of the bubble are identical to that of the bulk magma. The growth of a spherical bubble in a finite incompressible shell of liquid needs to be computed and the shell model understanding forms this basis for the geometric relationships within the numerical model. Coumans et al. (2020) uses an equation which includes the influence of capillary pressure on the bubble:

$$p_g = p_\infty + \frac{2\gamma}{R} + 4\eta \frac{dR}{dt}\left(\frac{1}{r} - \frac{r^2}{S^3}\right), \tag{2}$$

where p_∞ is the ambient pressure, $\frac{2\gamma}{R} = p_c$ is the capillary pressure, and γ is the gas-liquid interfacial tension, R is the present bubble radii, t is time, S is the radius of the shell, and η is the dependent melt viscosity. These terms represent the different variables at play in the shell model (figure 3.1) with the gas pressure, p_g being the pressure of the gas in the bubble which is acting against p_c which is acting to shrink the bubble, which the viscous term is resisting any change in bubble size. The ambient pressure, or far-field pressure is acting inwards, thus a positive far-field pressure acts to shrink the bubble.

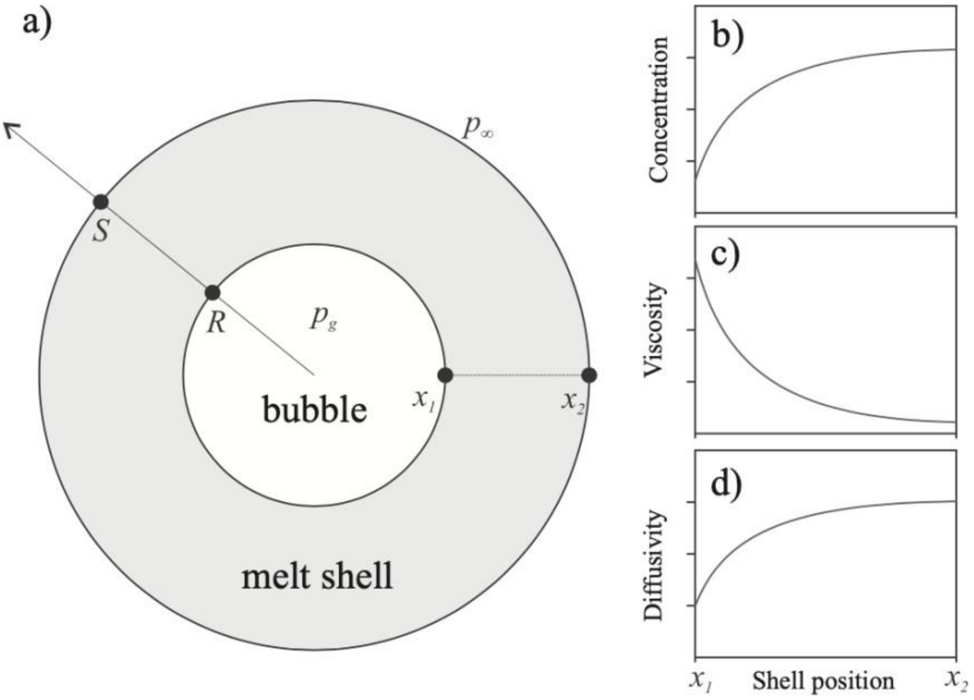

Figure 3.1 The geometry of the shell model. A) A single unit cell, the line $x_1 \rightarrow x_2$ *is a radial transect across the melt shell, b-d) schematic representation of spatial variation in concentration of dissolved* H_2O *melt viscosity, and diffusivity of* H_2O *across the radial transect* $x_1 \rightarrow x_2$ *during bubble growth (Coumans et al., 2020).*

The Lagrangian coordinate system is used because the radial position, x of any infinitesimal shell of melt does not change as the bubble grows or shrinks. The Lagrangian radial coordinate x is related to the Eulerian radial coordinate A by conservation of volume:

$$A^3 - R^3 = x^3 - R_0^3, \tag{3}$$

Evaluating equation (3) allows for the calculation of the spatial distribution of H_2O concentration in the melt $C(x)$ at time t. This is calculated by solving Fick's second law in the Lagrangian coordinate system (Braithwaite et al., 1999; Blower et al., 2001b):

$$\frac{\partial C}{\partial t} = \frac{1}{x^2}\frac{\partial}{\partial x}\left(D\frac{A^4}{x^2}\frac{\partial C}{\partial x}\right), \tag{4}$$

D is the diffusivity of H_2O in the melt, A is the Eulerian radial coordinate, and C is in wt.%. The radial H_2O concentration distribution is used to compute the mass m of gas in the bubble at time t by assuming conservation of mass of H_2O within the bubble shell unit:

$$m = m_0 + \frac{4\pi\rho_m}{100}\left(\int_{R0}^{S0} C(x,0)x^2dx - \int_{R0}^{S0} C(x,t)dx\right), \tag{5}$$

m_0 is the initial mass of gas in the bubble, ρ_m is the density of the melt. Calculating the mass of gas is imperative for further calculation of mass $m(t)$ and the bubble radius $R(t)$ at any given pressure and temperature, it is also essential in calculating the bubble pressure via the EOS. These are the fundamental questions which the numerical model is based upon.

3.3 Model Components

The general model requires constituent models for composition, diffusivity, solubility, viscosity, and the EOS. The models included by Coumans et al. (2020) are the most comment and most likely to be suitable to a wide range of decompression experiments. The constituent models, relevant to this study are used by Burgisser and Gardner (2005), are discussed below.

The composition of the Burgisser and Gardner (2005) samples are natural crystal-free rhyolitic glass from the Panum Crater Dome, CA. This composition is displayed in table 3.1:

	Glass (wt.%)	Bulk (wt.%)
SiO_2	75.64	76.10
Al_2O_3	12.38	12.66
MgO	0.03	0.03
FeO	0.94	1.03
TiO_2	0.08	0.07
CaO	0.54	0.59
K_2O	4.72	4.68
Na_2O	4.17	4.07
P_2O_5	0.01	0.03
MnO	0.07	0.05
Cl	0.06	0.07
H_2O^+	NA	0.27
H_2O^-	0.17	NA
CO_2	ND	NA
Total	98.81	99.65

Table 3.1 The Panum Crater Dome composition. From Westrich and Eichelberger, 1994; Mangan and Sisson, 2000. NA = not applicable, ND = not determined.

The Giordano (2008) viscosity function predicts the viscosity of silicate melts as a function of temperature and melt composition. To input the composition into the model, the values for: $SiO_2, TiO_2, Al_2O_3, FeO, MgO, CaO, Na_2O, K_2O, P_2O_5, H_2O$ and F_2O and must be listed in the same order for each composition. It is input as wt.% and these values are used for further calculations in relation to the composition.

For the solubility function, the Liu et al. (2005) model is used. This function is not directly discussed in the Burgisser and Gardner (2005) paper, but it is chosen because of the function’s pressure and temperature constraints. Liu et al. (2005) carry out experiments into H_2O solubility on synthetic haplogranitic and natural rhyolitic melts and measures the changing H_2O concentration in samples as the temperature and pressure decreases. Combining these results with other literature, an empirical model is developed for H_2O and CO_2 solubility, however only the H_2O equation is used for the Burgisser and Gardner (2005) study:

$$H_2O_t = \frac{354.94P_W^{0.5} + 9.623P_W - 1.5223P_W^{1.5}}{T} + 0.0012439P_W^{1.5}, \tag{6}$$

where H_2O is total dissolved H_2O content (wt.%), $P_W = X_W^f P$ where X_W^f is the mole fraction of H_2O in the fluid, T is temperature and P is pressure in MPa. The Liu et al. (2005) solubility model is valid over the range of $973 - 1473$K and $0 - 500$MPa. These conditions align with those used by Burgisser and Gardner (2005) and include pressure dependence, unlike the alternative solubility model by Ryan et al. (2015) which is also included in the numerical model:

$$H_2O_t = \frac{92.3}{T} + 0.0287, \tag{7}$$

A pressure dependence in the solubility function is important for the Burgisser and Gardner (2005) study because of the varying pressures used when carrying out a parametric sweep. A wide range of pressure values are investigated (see chapter 6).

The diffusion model used is from a study by Zhang and Ni (2010), specifically equation 15 which is applicable for a simple metaluminous sample. Zhang and Ni (2010) carry out a review of H_2O, CO_2 and O_2 diffusion to develop several different equations for simple and non-simple compositions. The simple equation is best suited in this instance because it neglects what the species are and is suitable when the main objective of Burgisser and Gardner (2005) is to track textural changes. The Zhang and Ni (2010) experiments have similar experimental conditions to Burgisser and Gardner (2005): $676 - 1900$K, $0 - 1900$MPa and $0 - 8$wt.% total H_2O.

$$D_{H2Ot}^{rhyolite} = C_W \exp\left(-18.1 + 1.888P - \frac{9699 + 3626P}{T}\right), \tag{8}$$

P is pressure in GPa and C_W is wt.% of H_2O_t. $D_{H2Ot}^{rhyolite}$ is the diffusivity of H_2O_t in rhyolite. The non-simple equations that Zhang and Ni (2010) develop are suitable for looking at different species concentrations such as in Buono et al. (2020) which examines the presence of CO_2.

The viscosity function used for the Burgisser and Gardner (2005) study is the Giordano et al. (2008) equation which has been calibrated for a range of melt compositions – including rhyolite. Giordano et al. (2008) base their model on > 1770 viscosity measurements of multicomponent anhydrous and volatile-rich silicate melts. The experimental conditions used are $798 - 1978$K and $0 - 0.8$wt.% total H_2O.

$$log_{10}\eta = J_1 + \frac{J_2}{T - J_3}, \tag{9}$$

where J_1, J_2 and J_3 represent adjustable parameters. The Giordano et al. (2008) equation for temperature dependence of viscosity (η) is modelled by the Vogel-Fulcher-Tammann (VFT) equation. The VFT equation is used to describe the behaviour of temperature-dependent viscosity upon approaching the glass transition (Vogel, 1921; Fulcher, 1925).

$$V_g = \frac{nR_gT}{P}, \tag{10}$$

Where V_g is volume of gas, n is amount of moles and R_g is the ideal gas constant (8.3144Jmol^{-1}K^{-1}). The Ideal Gas Law is chosen because of its simplicity and ability to apply it to most, if not all, experimental scenarios. It is found by Coumans et al. (2020) that there is minimal difference between outcomes when using the Ideal Gas Law and the Pitzer and Sterner (1994) EOS models. EOS gives the pressure in the gas (or supercritical fluid) phase and is important if considering different stages of the melt during the experiment. Pitzer and Sterner (1994) develop an EOS for a wide range of pressures where the Ideal Gas Law would fail, including fluids which include both H_2O and CO_2.

The Coumans et al. (2020) model includes three pressure-temperature-time pathways: 1) Constant pressure and constant temperature, 2) constant pressure and decreasing temperature, and 3) decreasing pressure and decreasing temperature. These three pathways are applicable to different experimental scenarios based on the experimental set up. The constant pressure, decreasing temperature pathway is applicable to the Burgisser and Gardner (2005) experiment sample ABG1 which, as it is under equilibrium conditions does not experience a pressure change but does experience a temperature change. The decreasing pressure and decreasing temperature are applicable to the remaining samples as it describes a decrease in pressure and a steady temperature before transitioning into a steady pressure and a temperature quench. The time at quench (t_{quench}) is calculated with the initial and final temperatures while the time at which pressure decreases (t_{Press}) is calculated using the initial and final pressure:

$$t_{quench} = \left|\frac{(T_f - T_0)}{dTdt}\right|, \tag{11}$$

$$t_{Press} = \left|\frac{(P_f - P_0)}{dPdt}\right|, \tag{12}$$

Where T_f and T_0 are the final and initial temperature (K), $dTdt$ is the cooling rate (Ks^{-1}), P_f and P_0 are the final and initial pressures (MPa) and $dPdt$ is the decompression rate (MPas^{-1}).

To improve model functionality, a new pressure-temperature-time pathway is built into the model for the purpose of this study – a newton cooling pathway (see section 3.4.2). To analyse the results of a newton cooling pathway, comparisons between linear and newton cooling are carried out (see section 4.2.2).

3.4 Model Development

3.4.1 Introduction

The numerical model constructed by Coumans et al. (2020) contains many components that are applied to the Burgisser and Gardner (2005) decompression experiments. However, some additions need to be made.

A newton cooling pathway makes for a more realistic cooling environment that samples will experience both in experimental and the natural environment. How a newton cooling pathway is applied and what difference it makes to resorption profiles is investigated in chapter 4.

To compute bubble growth and resorption, the initial gas volume fraction (ϕ_i), initial bubble radius (r_i), and the initial H_2O (H_2O_i) concentrations are required. The Burgisser and Gardner (2005) study does not provide these values for their experimental samples so for the purpose of this study, a code is developed to calculate these values based on the data provided. This development also has the possibility to be used for other similar studies.

3.4.2 Newton Cooling

The Burgisser and Gardner (2005) study uses a linear cooling pathway which follows a simple linear decrease.

$$Q = \frac{dT}{dt}, \tag{13}$$

where dT is change in temperature (K), dt (s) is change in time and Q is a constant.

A newton cooling pathway follows newton's law of cooling which states that the rate at which an object cools is proportional to the difference in temperature between the object and the object's surroundings. The ambient temperature is used in newton cooling to represent the temperature of the surroundings.

$$\frac{dT}{dt} = k(T - T_a), \tag{14}$$

where k is a newton cooling constant and T_a is the ambient temperature of the surroundings (K). An exponential form is written as:

$$T(t) = T_a + (T_0 + T_a)e^{kt}, \tag{15}$$

A newton cooling pathway is implemented into the numerical model (see appendix) to compare the different cooling pathways – linear and newton – under otherwise identical conditions.

These changes are made to the code to explore a more accurate cooling pathway for the Burgisser and Gardner (2005) experiments. The differences this cooling pathway makes to resorption are explored in section 4.2.2.

3.4.3 Equilibrium Bubble Growth Conditions

Burgisser and Gardner (2005) ensure the samples reach equilibrium conditions before being decompressed. The data provided by Burgisser and Gardner (2005) details the pressures used for sample synthesis (P_{syn}[MPa]) and the pressures reached for the equilibrium (P_i[MPa]) and decompression (P_f[MPa]) degassing runs. This data, combined with melt composition information, makes it possible to calculate the initial gas volume fraction (ϕ[-]) and initial water concentration (H_2O_t[wt.%]) of the bubble-bearing melt in the samples at equilibrium conditions. Initial bubble radius (r[m]) can also be calculated but requires additional inputs such as N_b and surface tension. The equilibrium conditions refer to closed system degassing whereby equilibrium is reached between the bubble population and the melt. These equilibrium conditions are necessary as inputs into the numerical model which requires these values prior to final model calculations.

Burgisser and Gardner (2005) provide an equation to calculate the initial gas volume fraction:

$$\phi = \frac{\beta}{WP + \beta} \tag{16}$$

$$\text{where } \beta = R_g T \rho_m k\left(\sqrt{P_0} - \sqrt{P}\right),$$

where ρ_m is density in the melt (kgm^{-3}), k is Henry's constant (3.44×10^{-6}kg$^{-0.5}$m$^{0.5}$s), P_0 is solubility pressure for the H_2O content in the melt when no bubbles are present (Pa), P is equilibrium pressure (Pa) and W is molecular mass of gas (18×10kgmol^{-1}). Equation (16) is adapted to include the effects of surface tension and can then be used to retrieve bubble equilibrium conditions for the ABG samples. All equation variables will be defined below.

In this section, equation (16) will be re-derived as Burgisser and Gardner (2005) do not derive the equation in their paper. Derivation will allow the equation to be assessed for its validity in terms of its assumptions, approach, and how it fits into the numerical model. The Burgisser and Gardner (2005) equation does not include the surface tension term which is used when calculating initial bubble radius so to add in this new term, the calculation needs to be revised and thus, must be examined from first principles.

The equation to calculate gas volume fraction, ϕ is defined as:

$$\phi = \frac{V_g}{V_g + V_m}, \tag{17}$$

where V_g is volume of gas (m^3) and V_m is volume of melt (m^3). V_g and V_m need to be calculated separately, using the ideal gas law, V_g equals:

$$V_g = \frac{nR_gT}{P}, \tag{18}$$

where n is number of moles of exsolved gas in the bubble, n equals:

$$n = \frac{M_g}{W}, \tag{19}$$

M_g is mass of gas (g). It is possible to calculate M_g as:

$$M_g = \frac{(X_o - X)M_m}{100}, \tag{20}$$

where X_0 is the wt.% of dissolved gas in the melt before any bubbles form, X is wt.% of dissolved H_2O at equilibrium pressure and M_m is mass of melt (g). Combining equations (18), (19), and (20):

$$V_g = \frac{(X_0 - X)M_mR_gT}{100WP}. \tag{21}$$

The solubility of H_2O in a bubble is defined using Henry's Law which states that the amount of dissolved gas in a liquid is proportional to its partial pressure above the liquid. In this instance, this is represented by the pressure in the pressure:

$$X = k\sqrt{P_b}, \tag{22}$$

where P_b is the pressure in the bubble. Including equation (22) in equation (21) produces:

$$V_g = \frac{k(\sqrt{P_0} - \sqrt{P})\rho_mV_mR_gT}{100WP}, \tag{23}$$

P is the partial pressure in the gas phase at equilibrium so for the case of a single gas phase, and in the absence of surface tension, this is the same as the confining pressure at equilibrium thus $P_b = P$.

Referring to equation (17), V_m equals:

$$V_m = \frac{M_m}{\rho_m}. \tag{24}$$

The volume of the gas in the bubble and the volume of the melt are not known. Putting equation (23) and (24) into (16) produces:

$$\phi = \frac{\frac{k(\sqrt{P_0} - \sqrt{P})\rho_m V_m R_g T}{100WP}}{\frac{k(\sqrt{P_0} - \sqrt{P})\rho_m V_m R_g T}{100WP} + \frac{M_m}{\rho_m}}, \tag{25}$$

which can be simplified to:

$$\phi = \frac{\beta}{\beta + 100WP} \tag{26}$$

$$\text{where } \beta = R_g T \rho_m k\left(\sqrt{P_0} - \sqrt{P}\right).$$

Equation (26) is equivalent to equation (16) but with an additional multiplication of 100. The factor of 100 is present in equation (16) because of the chosen solubility law where the units of X are wt.%.

Equation (16) does not consider the effect of the pressure arising from surface tension on the bubble, which is described by the Young-Laplace equation. The effect is due to surface tension creating a pressure difference between the inside and the outside of the bubble. The Young-Laplace equation relates this pressure difference to the shape of the bubble (Butt et al., 2006). Pressure arising from surface tension is defined as:

$$P_{ST} = \frac{2\gamma}{R}, \tag{27}$$

where γ is surface tension (-) and R is radius of the bubble (m). This influence of surface tension should be included in equation (26), as radius is the denominator in the equation. The result is that the P_{ST} term is very large for very small bubbles thus when looking at very small bubbles at equilibrium the P_{ST} term will become important.

In equation (26) P becomes P_b however these terms are not equal when considering surface tension as equation (26) includes an additional term from the Laplace stress:

$$P_b = P + \frac{2\gamma}{R}. \tag{28}$$

The β term in equation (26) changes because of the amount of exsolved gas calculated via the solubility law which depends on P_b rather than P:

$$\beta = R_g T \rho_m k\left(\sqrt{P_0} - \sqrt{P_b}\right). \tag{29}$$

As P_b is a function of r, which depends on the exsolved gas volume, which in turn depends on P_b, equation (26) now becomes implicit and can be solved numerically. Thus, equation (26) can be rewritten as, and solved as:

$$\phi = \frac{\beta}{\beta + 100P_bW} \qquad (30)$$

$$\text{where } \beta = R_gT\rho_m k\left(\sqrt{P_0} - \sqrt{P_b}\right).$$

The solubility law in equation (22) is only applicable for certain compositions and studies. To calculate the initial water concentration of the bubble-bearing melt, the solubility law used in the Burgisser and Gardner (2005) study must be defined. The Liu et al. (2005) solubility law is:

$$H_2O_t = \frac{354.94P^{0.5} + 9.623P - 1.5223P^{1.5}}{T} + 0.0012439P^{1.5}. \qquad (31)$$

To calculate the initial water concentration, the initial temperature (T_0) and initial pressure (P_0), including the effect of surface tension, is used (P_b).

There is a relationship between r and V_g when assuming a spherical bubble:

$$V_g = \frac{4\pi R^3}{3}. \qquad (32)$$

This relationship allows the radius of the bubble to be calculated based on its known V_g and can be utilised in equation (30) as the radius term is held within the unknown P_b:

$$V_g = \frac{\beta V_m}{\beta + P_bW} \qquad (33)$$

$$\text{where } \beta = R_gT\rho_m \Big[\Big(\frac{354.94P_0^{0.5} + 9.623P_0 - 1.5223P_0^{1.5}}{T_0}\Big) + 0.0012439P_0^{1,5}\Big] - \Big[\Big(\frac{354.94P_f^{0.5} + 9.623P_f - 1.5223P_f^{1.5}}{T_f}\Big) + 0.0012439P_f^{1.5}\Big].$$

To calculate the radius, the unknown P_b must be solved, which can be done numerically. V_m, another unknown, can be estimated because of bubble number density (N_b). N_b is the number of bubbles per unit volume of melt, so its reciprocal is the volume of melt per bubble, V_m. Equation (33) can be rewritten as:

$$V_g = \frac{\beta\left(\frac{1}{N_b}\right)}{\beta + P_bW} \qquad (34)$$

$$\text{where } \beta = R_gT\rho_m \Big[\Big(\frac{354.94P_0^{0.5} + 9.623P_0 - 1.5223P_0^{1.5}}{T_0}\Big) + 0.0012439P_0^{1,5}\Big] - \Big[\Big(\frac{354.94P_f^{0.5} + 9.623P_f - 1.5223P_f^{1.5}}{T_f}\Big) + 0.0012439P_f^{1.5}\Big].$$

To make this equilibrium function compatible with the rest of the numerical model, the solubility functions used (Liu et al., 2005; Ryan et al., 2015) must be included in equation (34). This will allow equation (34) to be applied to any decompression experiment, regardless of its chosen solubility function. The equilibrium function allows equilibrium bubble conditions to be calculated and then put into the numerical model to create a fully automated calculation (see appendix).

3.5 Conclusion

The Coumans et al. (2020) model is an accumulation of many different relevant and useful functions in relation to solubility, viscosity, EOS, diffusivity, and composition. Additions are made to the model including a newton cooling pathway to represent a more accurate cooling pathway and a new function which calculates equilibrium bubble conditions, based on the input for the initial pressure and temperature conditions. These additions are what make the Coumans et al. (2020) numerical model fit for purpose for this research and why it can answer the questions posed in chapters 1 and 2.

4. Importance of Resorption

4.1 Introduction

A MATLAB numerical model is used to understand the conditions under which bubble resorption may be important and how that influences experiments that aim to understand bubble growth pathways. Burgisser and Gardner's (2005) study has been chosen to evaluate bubble growth conditions for a typical rhyolitic composition.

Under controlled pressure and temperature conditions, rhyolitic samples are decompressed and then rapidly quenched to draw conclusions on the volcanic environment under which the samples formed. The experiments involve 22 samples, titled 'ABGx'. 'ABG1' acts as a control sample and does not experience a second stage of decompression and is in a state of equilibrium. How resorption of an equilibrium bubble is computed using the numerical model is discussed. Resorption of a growing bubble, from sample ABG14 is also discussed in comparison to ABG1.

The difference between a linear and newton cooling pathway is investigated. Two aims are drawn up to investigate how newton cooling progresses and differs compared to a linear cooling pathway.

4.2 Resorption of a Bubble at Equilibrium

4.2.1 Experimental Conditions of ABG1

The composition, solubility, diffusivity, viscosity, and Equation of State (EOS) functions applicable to the Burgisser and Gardner (2005) study are based on the pressure and temperature conditions of the decompression experiments (Coumans et al., 2020). These functions are the Panum Crater Dome composition (Mangan and Sisson, 2000), the Liu et al. (2005) solubility model, the Zhang and Ni (2010) diffusivity model, the Giordano et al. (2008) viscosity model, and the Ideal Gas Law EOS model. These functions are described in detail in chapter 3.

Sample synthesis takes place at 825°C (1098K) and 150MPa. Pressure is dropped to 100MPa to generate an equilibrium bubble population; this pressure is maintained throughout the run to ensure no bubble growth takes place. The temperature is lowered to 300°C during rapid quenching of the sample (table 4.1) at a cooling rate ($dTdt$) of 100Ks^{-1}. It is assumed that the bubble goes out of equilibrium as soon as the temperature drop begins. The pressure is held constant, allowing the bubble to get further out of equilibrium and shrink.

Sample	T_{exp} (°C)	P_{syn} (MPa)	P_i (MPa)	P_f (MPa)	$dPdt$ (MPas^{-1})
ABG1	825	150	100	100	N/A

Table 4.1 The temperature, pressure, and decompression rate conditions for sample ABG1.

To validate the conditions, inputs, and the accuracy of the numerical model, sample ABG1 is used to act as an equilibrium indicator when calculating the initial gas volume fraction (ϕ_i), initial water concentration (H_2O_i) and initial bubble radii (r_i) (section 3.4.3). Using the equilibrium calculation discussed in the previous chapter, ϕ_i is 0.1108, r_i is 25.6µm, and H_2O_i is 3.97wt.%.

Some required inputs in the numerical model such as the value for surface tension and melt density are not specified by Burgisser and Gardner (2005) so values for a typical rhyolite composition are used (0.22Nm^{-1} (McBirney and Murase, 1978; Hajimirza et al., 2019) and 2350kgm^{-3} (Lesher and

Spera, 2015) respectively). 40 seconds is the time input into the numerical model as resorption of an equilibrium bubble occurs quickly.

Resorption of an equilibrium bubble follows the constant pressure, decreasing temperature pathway because the pressure remains constant throughout the experiment while the temperature decreases. The bubble stops shrinking when the melt is unable to move anymore because the temperature is too low. At the end of the simulation, we find disequilibrium in the water profile of the experimental run (figure 4.1B).

4.2.2 Quenching of ABG1

The model results for ABG1 are shown in figure 4.1. Figure 4.1A is split into two panels, the top panel shows the decrease in temperature from 1098K to 573K while the pressure is held constant at 100MPa. The second panel shows the change in gas volume fraction, $\Delta\phi$ which is the difference between the maximum ϕ encountered by the bubble at any point during the experiment, and the final ϕ after quench. For ABG1, the bubble undergoes a decrease in ϕ by 0.0214 before remaining constant. Figure 4.1B is the water profile of the bubble. The water content is measured against the distance from the bubble (in μm) in incremental time steps, represented with the different coloured lines. The water profile shows that the bubble is frozen in a state of disequilibrium by the final time stamp (40s).

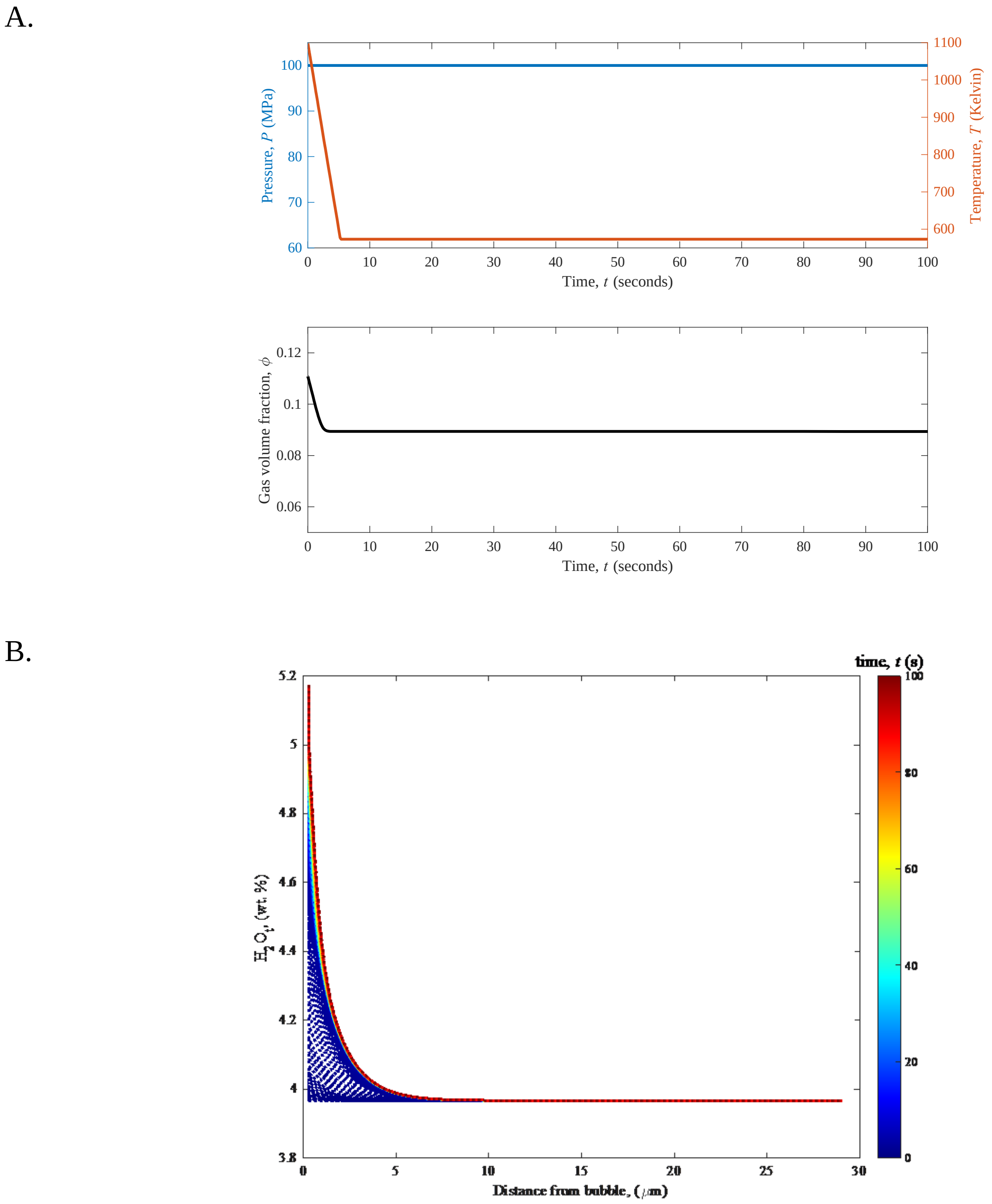

Figure 4.1 The model output for sample ABG1. A: There is a decrease in ϕ from 0.1108 to 0.0894 as temperature is decreasing but by 5.4s when the final temperature has been reached, ϕ remains constant. B: As the bubble size remains constant after 5.4s, there is a lack of water movement in and out of the bubble following this time stamp. The exponential curve seen is due to the process of initial bubble shrinkage.

4.2.3 Lessons from ABG1: Implications and Interpretations

Based on figure 4.1, when ABG1 quenches this causes a small amount of bubble resorption. The bubble resorption only stops because the viscosity of the melt is too high for further shrinkage and diffusivity becomes too low for further resorption. The cooling rate of 100Ks^{-1} is provided by Burgisser and Gardner (2005) and follows a linear cooling pathway. Alternative cooling pathways are explored in section 4.4.

At a constant pressure of 100MPa and an initial temperature of 1098K, the bubble is in equilibrium with the melt, however following a temperature decrease, solubility increases and water moves from the bubbles into the melt, only stopping when the temperature drop is too low for the melt and water to move anymore. Figure 4.1B is used to support this movement of water. In the earliest experimental timestep ($00 - 05$s) as quench begins, the water migrates from the bubble into the melt from 5.10wt.% to 3.97wt.%.

Based on figure 4.1, it is understood that resorption of a bubble initially at equilibrium does happen, but only by a small amount. The bubble begins in a state of equilibrium, so no bubble growth takes place, however if there is a temperature decrease then resorption will always happen to some extent. It is important to understand how a bubble experiencing equilibrium conditions such as ABG1 may behave before looking at how a bubble experiencing decompression may grow and resorb. In the natural environment ABG1can be represented with a bubble which undergoes a rapid quench such as cooling of a tephra clast (figure 1.2).

4.3 Resorption of a Growing Bubble

4.3.1 Experimental Conditions of ABG14

To examine a growing bubble, sample ABG14 is used. The composition, solubility, diffusivity, viscosity, and EOS functions remain the same as those used for the equilibrium sample. The typical rhyolitic values for surface tension and melt density are also used for ABG14 (0.22Nm^{-1} (McBirney and Murase, 1978; Hajimirza et al., 2019) and 2350kgm^{-3} (Lesher and Spera, 2015) respectively). The sample synthesis conditions also remain the same, taking place at 825°C and 150MPa. The pressure decreases to 100MPa to generate an equilibrium bubble population; this pressure is then decreased to 80MPa at a rate of 0.5MPas^{-1}, populating the sample with growing bubbles. When the pressure reaches 80MPa, decompression is stopped and temperature is lowered to 300°C during rapid quenching of the sample (table 4.2) at a $dTdt$ of 100Ks^{-1}.

Sample	T_{exp} (°C)	P_{syn} (MPa)	P_i (MPa)	P_f (MPa)	$dPdt$ (MPas^{-1})
ABG14	825	150	100	80	0.5

Table 4.2 The conditions used on sample ABG14.

It is expected that during decompression of ABG14, bubble growth will occur, followed by resorption during quench, ϕ_i is 0.1109, r_i is 23.8μm, and H_2O_i is 3.97wt.%. The final gas volume fraction reached following bubble growth is known as peak gas volume fraction (ϕ_p).

4.3.2 Quenching of ABG14

The model results for the decompression and quenching of sample ABG14 are shown in figure 4.2. As the pressure decreases from 100 to 80MPa, solubility decreases and water moves from the melt into the bubble, driving bubble growth and leading to a decrease in water content towards the bubble. However, the rapid quench results in a solubility increase and the water moves from the bubble back into the melt – causing resorption.

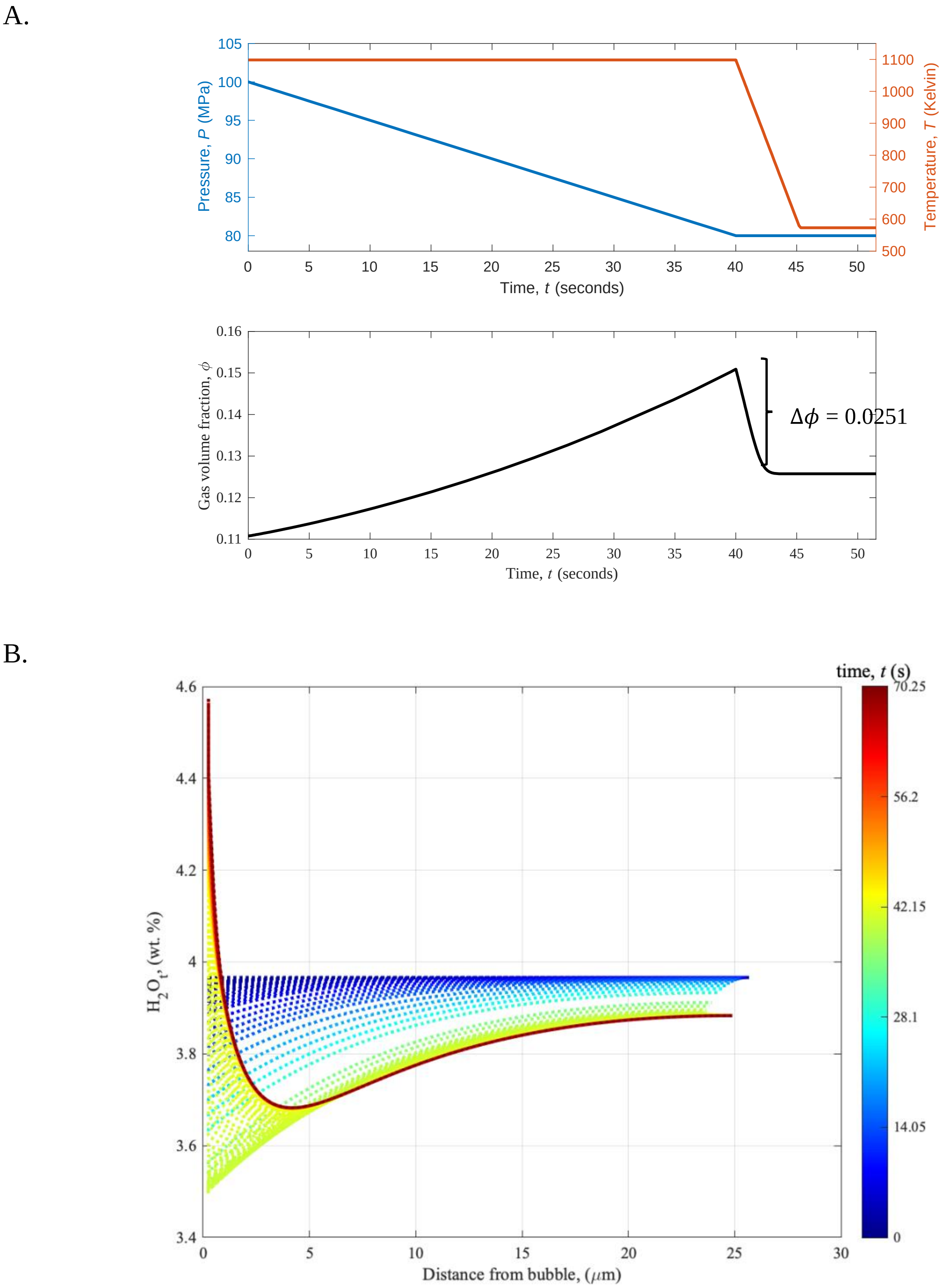

Figure 4.2 The model output for sample ABG14. A: From $0 - 40$s, the bubble increases in size from a ϕ_i of 0.1109 to a ϕ_p 0.1509 before resorbing from $40 - 43$s to a ϕ_f of 0.1258. B: The water profile supports the growing and resorbing process. At the beginning of the experiment, a constant water content of 3.96wt.% is maintained before the water content increases with an increasing distance from the bubble. The profile ends with the water moving back into the melt.

4.3.3 Lessons from ABG14 vs. ABG1: Implications and Interpretations

In comparison to ABG1, the bubble experiences a growth period prior to quench. The bubble in ABG14 grows by 0.04 before resorbing, however when factoring in the decrease in size due to resorption, the bubble only increases in size by 0.015. When evaluating ABG1, it is a process of bubble shrinkage due to rapid quench. ABG14 represents a more complex scenario – where the beginning and end ϕ are known but the full extent of the bubble growth is not, and this is where the numerical model plays a critical role in decompression experiments. The $\Delta\phi$ that the model calculates must be reliant on certain parameters. What potential parameters control the movement of water in and out of the bubble at such a rapid pace?

The rapid quench process is what causes resorption to occur so the $dTdt$ that this takes place at should affect how much water is able to move into the bubble, causing its shrinkage. At a slower $dTdt$ (figure 4.3), more water can leave the melt and move back into the bubble, creating a larger amount of resorption.

At a cooling rate of 50Ks^{-1}, compared to the 100Ks^{-1} that Burgisser and Gardner (2005) use, a substantial amount of growth and resorption still occurs but resorption occurs to a greater extent with the bubble displaying the same level of growth (0.04) but a larger amount of resorption – representing only a growth of 30%.

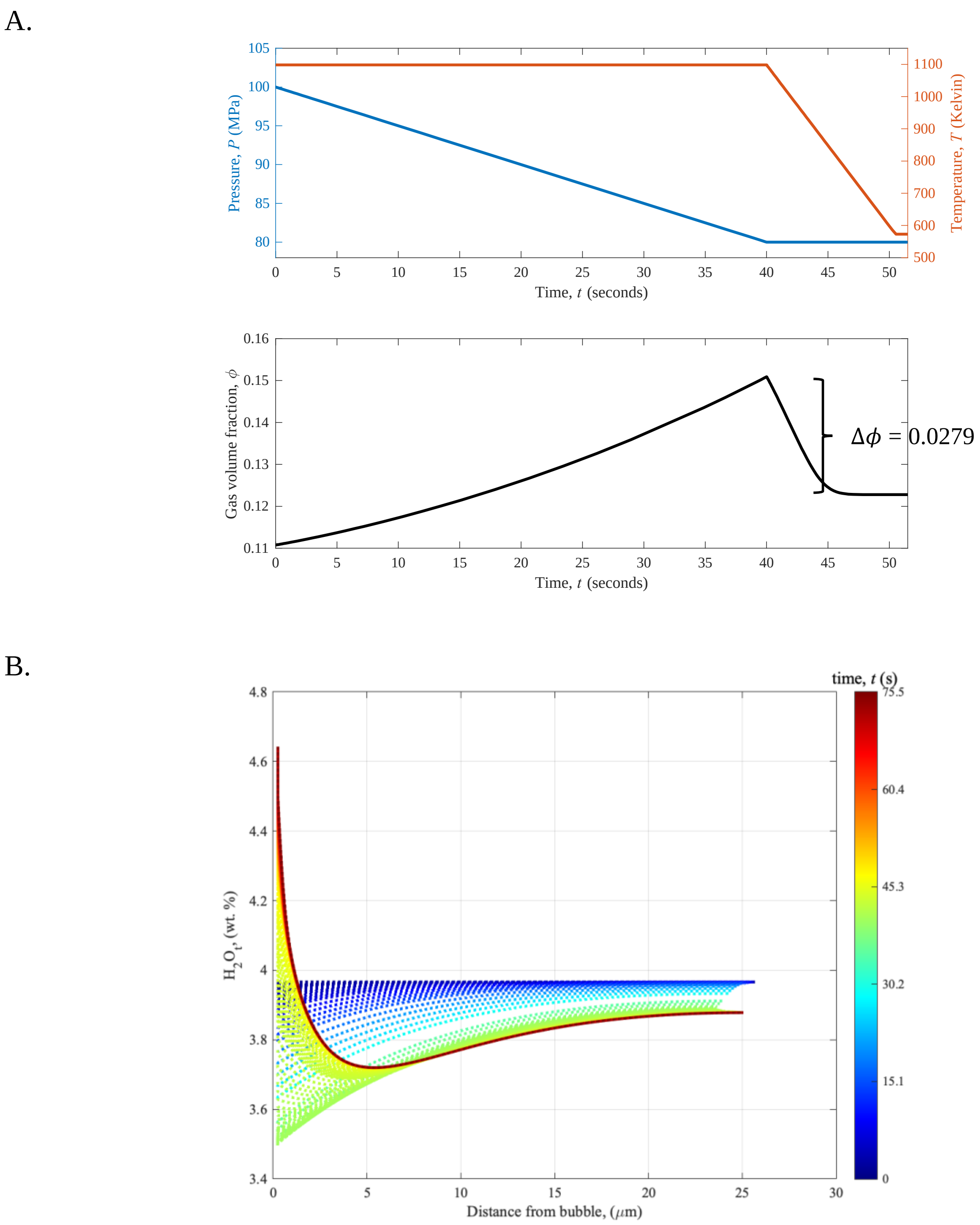

Figure 4.3 The model output for sample ABG14, at a lower $dTdt$ *of* $50Ks^{-1}$*. The bubble grows from* $0.4s$ *from* 0.1107 *to* 0.1507*. The slower* $dTdt$ *of* $50Ks^{-1}$ *results in resorption happening from* $40 - 47s$ *and the* ϕ *decreasing from* 0.1507 *to* 0.1228*. B: A similar profile to that of figure 4.2 with a larger amount of water moving closer to the bubble at a slower rate.*

Resorption has the potential to be influenced by cooling rate and hence any conclusions made about final bubble textures are affected. How much can resorption be influenced by different cooling rates and are there different cooling pathways a bubble may take?

4.4 Effect of Cooling Rate on Resorption of a Growing Bubble

4.4.1 The Different Styles of Cooling

There are two different types of cooling pathways which are investigated here. A linear cooling pathway is what has been used in sections 4.2 and 4.3, displaying a linear quench from initial (T_0) to final temperature (T_f). A newton cooling pathway is investigated in this section to see if different resorption results are produced. A newton cooling pathway for samples not at equilibrium are displayed in figure 4.4.

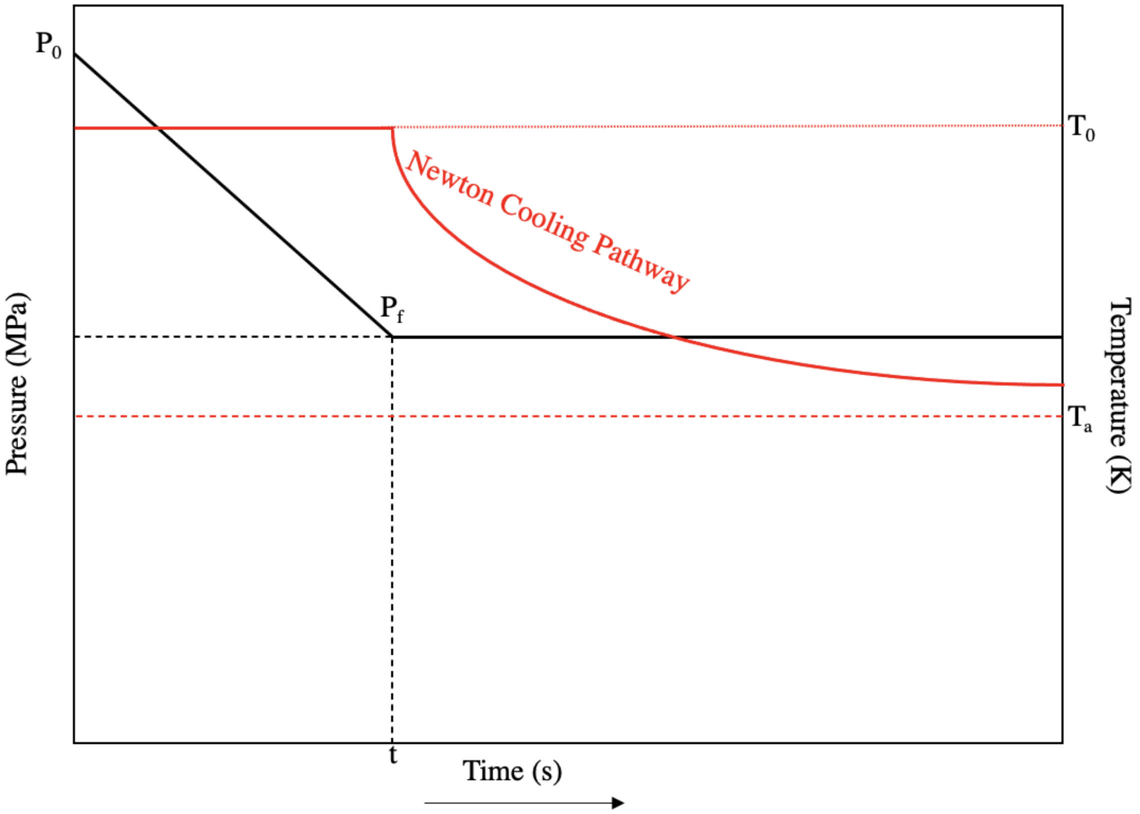

Table 4.4 The pressure and temperature pathways of newton cooling for sample ABG14. P_0 is initial pressure (MPa), P_f is final pressure (MPa). T_0 is initial temperature (K), and T_a is ambient temperature (K). Following a decrease, quenching begins at an experimental rate, never reaching the temperature of its surroundings (the ambient temperature).

4.4.2 Linear vs. Newton

Sample ABG14 is used to investigate differences between the cooling pathways by comparing the numerical model outputs. Two sets of plots are produced for ABG14 (figure 4.5) with the same conditions and parameters as discussed in section 4.3.1 with the only difference being that one of them is following a newton cooling pathway. Details of how the newton cooling pathway is input into the model is provided in the appendix.

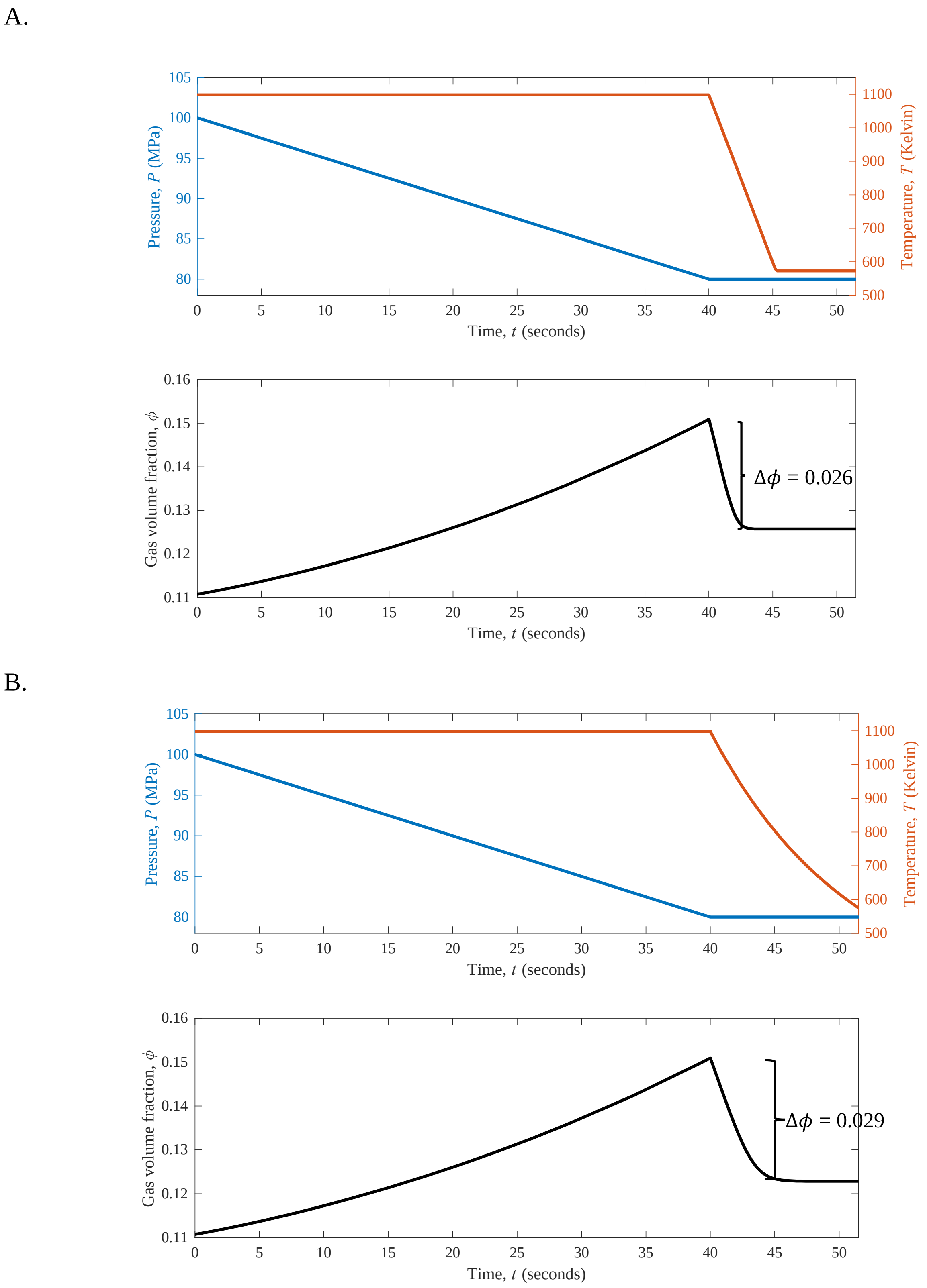

Figure 4.5 A. Linear Cooling. B. Newton Cooling. Both pathways follow an identical growth following the same decompression rate. However, following quench, the bubbles resorb by different amounts. Newton cooling only reaches its ϕ_f *after* 45s *while* ϕ_f *is reached more rapidly with linear cooling. Linear cooling experiences less resorption by 0.003.*

From this initial investigation, the different cooling pathways have negligible differences between $\Delta\phi$. However, an important parameter in calculating the cooling pathway is the cooling rate, as mentioned in section 4.3.3. When looking at the results of figure 4.4 and figure 4.5, it is apparent that the cooling rate may be the more influential factor in the amount of resorption and not the actual style of cooling. To investigate this further, the initial cooling rate is varied in several ways while also comparing results from both linear and newton pathways.

4.4.3 Different Cooling Rates with Different Pathways

Cooling rate is varied between $0.0001 - 200$Ks^{-1}. This range represents the typical experimental cooling rates used as well as cooling rates found in the natural environment. Slow cooling rates are recorded in nature (Huppert et al., 1984; Manley, 1992; Nichols et al., 2009; Wright et al., 2010; Browning et al., 2020) while faster, sometimes instantaneous, cooling rates tend to be used in experimental scenarios (Burgisser and Gardner, 2005; Befus and Andrews, 2018; Buono et al., 2020). Faster cooling rates are used in experiments because it allows for the preservation of the experimental material and to prevent further growth and diffusion. It is also difficult to control how slowly a sample can be cooled.

To investigate how cooling rate effects bubble resorption, three different types of cooling are modelled: 1. Linear cooling with a set initial $dTdt$, 2. Newton cooling with a set initial $dTdt$, and 3. Newton cooling with a set time to the glass transition temperature (T_g). The range of $dTdt$ values used are the same throughout.

1. Linear cooling with a set initial $dTdt$

This following the equation:

$$dTdt = \left|\frac{\left(T_f - T_0\right)}{t_{quench}}\right|, \tag{35}$$

where $dTdt$ is calculated based on the initial (T_0) temperature, the final (T_f) temperature, and the time of quench (t_{quench}), a linear relationship is then constructed from T_0 to T_f.

2. Newton cooling with a set initial $dTdt$

The relationship between $dTdt$ and k (newton constant) are set so that the cooling rates used are the same for linear and newton cooling. It is investigated whether there is a cooling rate at which the style of cooling is the primary control. Newton cooling is represented with the equation:

$$k = -\frac{dTdt}{T_0}. \tag{36}$$

3. Newton cooling with a set time to the glass transition temperature (T_g)

The glass transition temperature is the temperature at which the sample will transform into glass. This method sets $dTdt$ based on the time it takes to reach T_g:

$$t_g = \frac{(T_0 - T_g)}{dTdt}, \tag{37}$$

where t_g is the take taken to reach T_g (s). Based on t_g the new newton cooling constant (k) is given by:

$$k = \frac{1}{t_g} In\left(\frac{\left(T_g - T_a\right)}{\left(T_0 - T_a\right)}\right). \tag{38}$$

It can be argued that models 2 and 3 are similar as T_g is in itself a function of $dTdt$, however, they remain distinctly different. This is because model 2 only considers $dTdt$ and T_0 when calculating k while model 3 considers T_0, T_g, $dTdt$, t_g, and T_a – considering the temperature of its surroundings, which are not influenced by $dTdt$ and remain constant throughout the experimental run. It is seen in section 4.4.5 how models 2 and 3 produce different resorption results.

4.4.4 Different Cooling Rates: Results

When looking at linear cooling for sample ABG14, for cooling rates $0.0001 - 0.001$Ks^{-1} the bubble resorbs completely and ‘bubble too small’ is the model output. This cooling rate is too slow and 100% of the water in the bubble moves back into the melt, causing the bubble to disappear out of existence. In figure 4.6A, a cooling rate of 0.01Ks^{-1} results in a much longer experimental timescale of $\times 10^{-4}$s. The amount of resorption results in the bubble undergoing an overall reduction in size, compared to its original size.

$\Delta\phi$, the difference between the maximum ϕ and final ϕ, is plotted in figure 4.6B. For $0.01 - 200$Ks^{-1} $\Delta\phi$ decreases with increasing cooling rate. The faster the cooling rate, the less resorption occurs as less water can move from the melt shell into the bubble. A decreasing curve develops from 0.01Ks^{-1} where the higher the cooling rate, the smaller the difference between $\Delta\phi$ values. This suggests that following an infinite cooling rate, $\Delta\phi$ will eventually reach 0. In figure 4.6C, a typical resorption pathway is seen, although it is smaller than those recorded for lower cooling rates (figure 4.5), confirming that resorption decreases with increasing cooling rate.

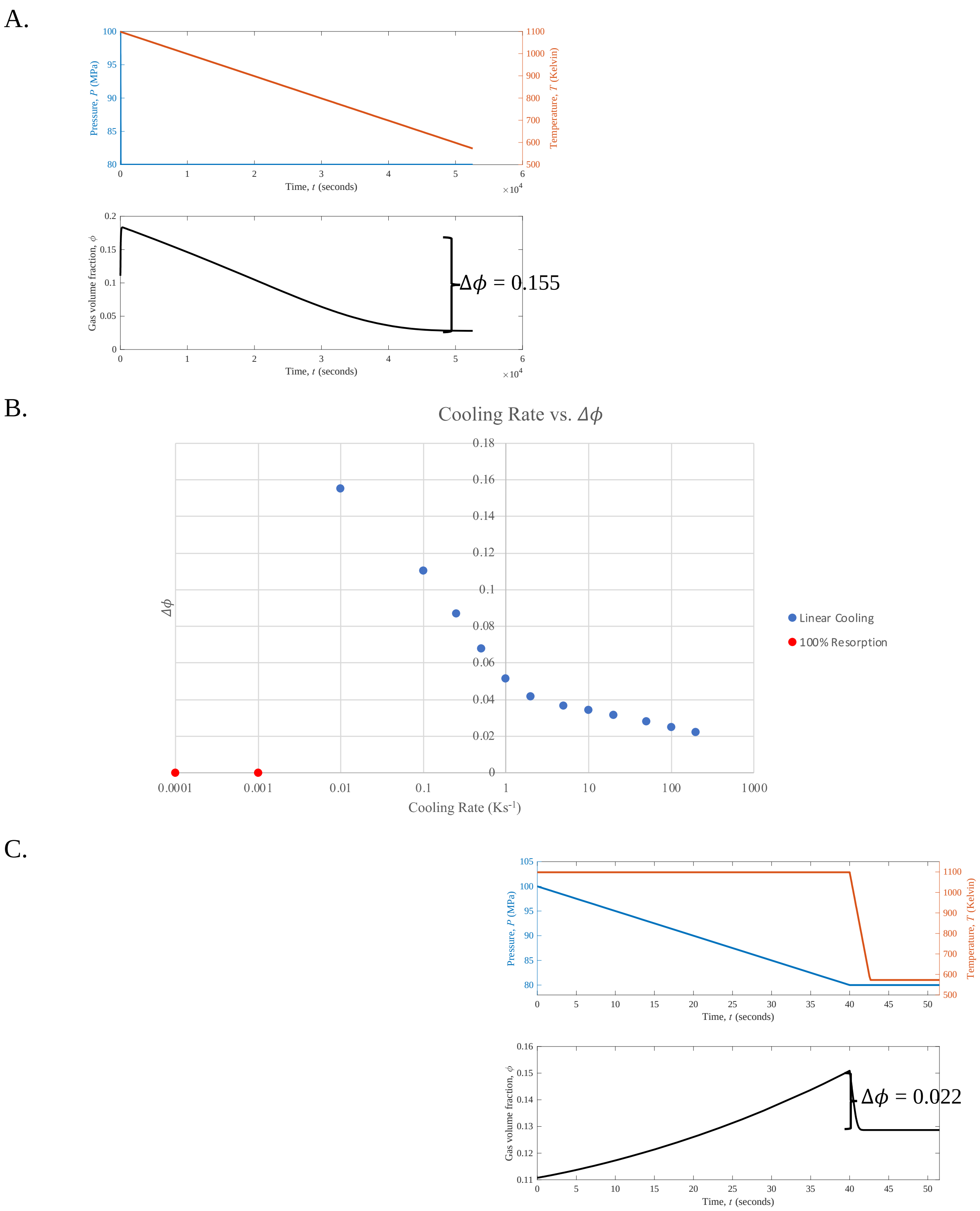

Figure 4.6 A. The ϕ profile of sample ABG14, following a linear cooling rate of $0.01Ks^{-1}$*. B. The changing $\Delta\phi$ with increasing cooling rate for sample ABG14. C. The ϕprofile of sample ABG14 following a linear cooling rate of* $200Ks^{-1}$*.*

4.4.5 Different Cooling Pathways: Results

When looking at the different cooling pathways: linear cooling with a set initial $dTdt$, newton cooling with a set initial $dTdt$, and newton cooling with a set time to T_g the amount of resorption that occurs at the same cooling rate (or newton constant), differs (figure 4.7). Each pathway has a similar ϕ profile but the time the experiment takes and the $\Delta\phi$ depends on the pathway selected. Linear cooling with a set initial $dTdt$ (figure 4.7A) defines a clear linear pathway in which resorption takes place. Newton cooling with a set initial $dTdt$ is an unusual case because it takes over 250 seconds more to complete the experimental run. This is because equation (36) only considers the initial temperature while equation (35) considers initial and final temperature as well as time at quench. Figure 4.7B also displays the greatest $\Delta\phi$ but this could be due to the bubble having more time to resorb. Figure 4.7B appears to show growth continuing for a while after decompression has finished. This is because the bubble remains out of equilibrium, and so water continues to exsolve from the melt into the bubble after decompression stops. If the temperature were held constant here, the bubble would continue to grow until it reached a new equilibrium at the final pressure. However, because the quench starts immediately once the pressure drop finishes, the solubility of the water starts to increase. Initially, this effect is less important that the remaining disequilibrium that persists beyond the end of the decompression, but as temperature continues to fall, the increased solubility starts to dominate, and the bubble growth first slows, then reverses as the water moves back into the melt from the bubble, causing the bubble to shrink via resorption. This is also the reason behind why the ϕ_p in the very slow quench experiments (figure 4.6B) is so high. These slow quench experiments would likely have reached (or nearly reached) equilibrium at the final pressure before the cooling started to have an appreciable effect on solubility.

Newton cooling with a set time to T_g (figure 4.7C) has the smallest $\Delta\phi$ but takes over a similar experimental time to figure 4.7A, only differing by 50s. This is because equation (37) and (38) consider initial temperature, glass transition temperature and ambient temperature values which are close to the final temperature values used in equation (35).

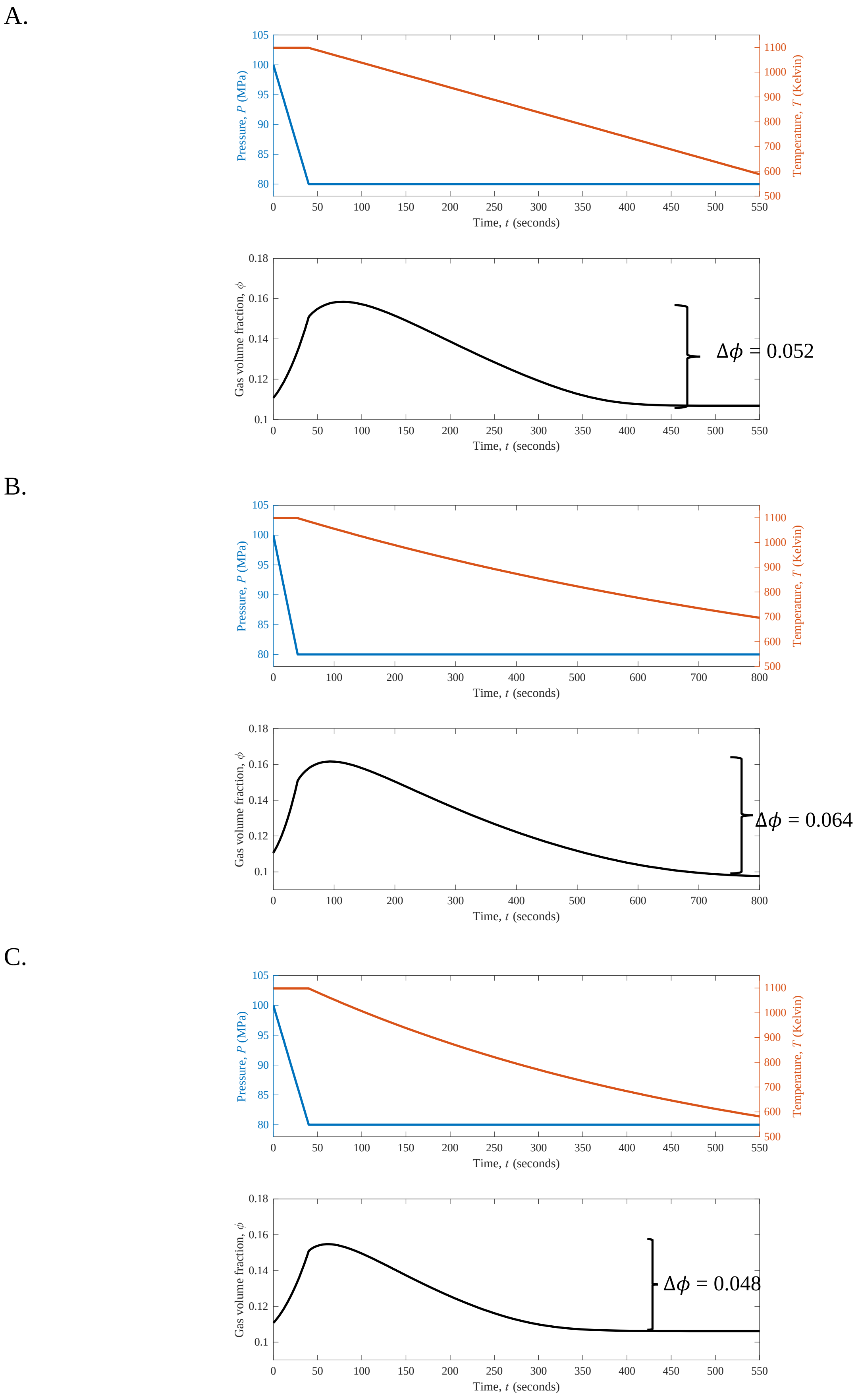

Figure 4.7 The pressure-temperature-time (P-T-t) profiles and ϕ*profiles for sample ABG14 following three different cooling pathways at a cooling rate of* $1Ks^{-1}$*. A. Linear cooling with a set initial* $dTdt$*, B. Newton cooling with a set initial* $dTdt$ *and, C. Newton cooling with a set time to* T_g*.*

When comparing $\Delta\phi$ for every cooling pathway, there are clear disparities between $0.01 - 10$Ks^{-1} however from 25Ks^{-1} the $\Delta\phi$ values begin to converge (figure 4.8).

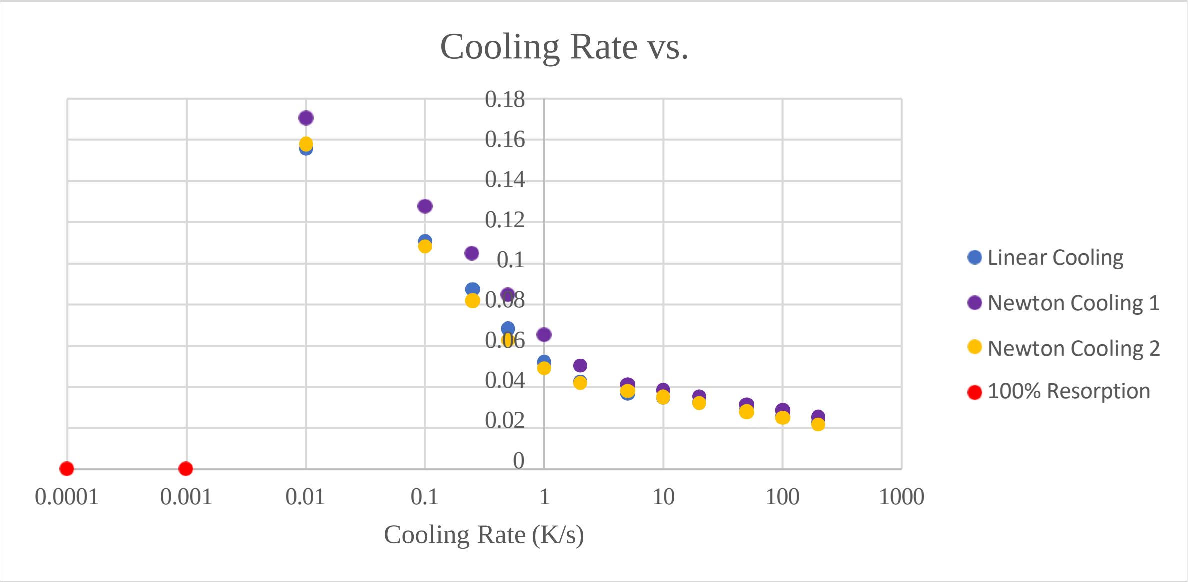

Figure 4.8 The $\Delta\phi$ *calculated for linear cooling with a set initial* $dTdt$*, newton cooling with a set initial* $dTdt$ *(newton cooling 1), and newton cooling with a set time to* T_g *(newton cooling 2). Cooling rates* $0.0001Ks^{-1}$ *and* $0.001Ks^{-1}$ *create bubbles which completely resorb for all cooling pathways.*

4.5 Discussion

4.5.1 Progression with other ABG samples

The numerical model has been tested on sample ABG1 to look at resorption of a bubble at equilibrium and ABG14 to look at resorption of a growing bubble. This study can proceed by analysing the other ABG samples collected by Burgisser and Gardner (2005) and recording any resorption results. It is expected that resorption will be seen as the other samples undergo similar conditions to ABG14.

Only four out of the 22 ABG samples will be evaluated – ABG2, ABG6, ABG14, and ABG15. There four samples are the same samples McIntosh et al. (2014) look at when investigating evidence for resorption. The use of these samples will allow for corroboration with the conclusions made by McIntosh et al. (2014). The investigation of these samples will be undertaken in chapter 5.

4.5.2 The Ideal Cooling Rate for the Numerical Model

To minimise resorption a high cooling rate is preferred and recommended. Burgisser and Gardner (2005) use 100Ks^{-1} which is already a high $dTdt$, however there is the potential to use higher cooling rates. There is, however, a limit where it is not experimentally possible to create a controlled instantaneous cooling. A bubble that grows and then does not resorb at all may not be possible as it is impossible to carry out a decompression experiment without the final rapid quench process.

If resorption can vary by up to 0.14 when changing the cooling rate, other factors which might influence resorption should also be considered and investigated. These factors include bubble number density (N_b) and pressure, as well as a combination of these factors. These influences will be evaluated in chapter 5 and 6.

4.5.3 The Ideal Cooling Rate in Nature

Burgisser and Gardner (2005) use a cooling rate of 100Ks^{-1} for their experimental samples and this is the cooling rate used in the numerical model in this thesis. However, is it correct to assume that this is an appropriate cooling rate to apply to nature? As mentioned in section 4.4.3, slow cooling rates are often recorded in nature, in comparison to faster rates which are used in laboratory environments.

Figure 4.8 reveals that a high amount of resorption occurs at the slowest cooling rates and in some cases ($0.0001 - 0.001$Ks^{-1}) the bubbles resorb so much that the bubble disappears, and the numerical model does not compute a growth path for it. This may suggest that this is an unrealistic cooling rate to expect in experiments and in nature. Previous studies show that cooling in nature can take place at a wide range of cooling rates ranging from slow values such as 0.035Ks^{-1} (Huppert et al., 1984) to fast cooling with values such as 72.2Ks^{-1} (Nichols et al., 2009) with a range of cooling rates in between (Huppert et al., 1984; Flynn and Mouginis-Mark, 1992; Nichols et al., 2009; Browning et al., 2020).

Studies that aim to determine cooling rates in nature use a range of methods including melting of natural samples in the laboratory (Nichols et al., 2009), using numerical models (Manley, 1992), and remote sensing (Wright et al., 2010). Understanding the cooling rate of lava is important in determining thermal history. Nichols et al. (2009) uses the cooling rates of basaltic glasses at different depths of a submarine volcano to determine quenching at different distances from the basalt-seawater interface. Degassed blocky hyaclastite clasts cool at a rate of $0.1 - 72.2$Ks^{-1} while undergassed pillow rims cool at $0.2 - 46.4$Ks^{-1}. Figure 4.8 shows that resorption does happen between these values so it can be suggested that resorption as high as 0.15 occurred when the basaltic material quenched at depth. These values also suggest that the 100Ks^{-1} used in the numerical model in this thesis can occur in nature and is not an unrealistic value to represent eruption processes.

4.5.4 The Ideal Cooling Path

When comparing linear and newton cooling there only appears to be a clear difference of $\Delta\phi$ in relation to the lower cooling rates, however the difference is still very small. For the rest of this study, the newton cooling pathway with a set initial $dTdt$ is applied because of its more realistic representation of cooling in the laboratory and the natural environment. However, the numerical model is still equipped for both linear and newton cooling pathways (see appendix) to allow the user to decide with pathway is more applicable to their study.

4.6 Conclusion

Burgisser and Gardner (2005) include experimental data for a bubble at equilibrium (ABG1). To investigate if the equilibrium bubble calculations (equation 16 – 33) from section 3.4 work, and to validate the numerical model, resorption results for ABG1 are produced. The results from ABG1 suggest that the numerical model works as there is no bubble growth seen in the output. Subsequently, this study can proceed with investigating the other ABG samples.

Sample ABG14 is examined. This sample experiences bubble growth and resorption as shown in figure 4.2, how much this resorption can be influenced is analysed by lowering $dTdt$ from 100Ks^{-1} to 50Ks^{-1}. Resorption increases.

There are several different cooling pathways a decompression experiment can take. Linear and newton with newton being split into controlled by $dTdt$ or by T_g. Linear cooling and newton cooling controlled by T_g produce similar values for $\Delta\phi$ for a range of cooling rates however newton cooling controlled by $dTdt$ produce higher values for $\Delta\phi$. The newton cooling pathway based on $dTdt$ is used for the remaining investigations of this thesis.

5. Resorption Driven by Quench

5.1 Introduction

It is important to understand the extent to which resorption occurs in the Burgisser and Gardner (2005) samples. Quantifying resorption allows for improved analysis and interpretation of the data from their studies as well as similar studies. Each ABG sample is modelled individually and then compared to the resorption results reported by McIntosh et al. (2014) for the same samples. In this chapter the results from ABG2, ABG6, ABG14, and ABG15 confirm that resorption is happening, and that resorption is influenced by various experimental parameters.

Bubbles grow when they experience a pressure drop and then resorb due to the quenching process. This process is essential to decompression experiments and the numerical model this thesis utilises captures this process mathematically. This chapter will look at how changing experimental parameters influence resorption values in relation to the Burgisser and Gardner (2005) experiments.

The degree of disequilibrium and the configuration of the bubble/melt/H_2O system is different for each sample as the different pressure-temperature conditions represent different stages a bubble may be at in the volcanic conduit. These differences will be investigated in this chapter.

5.2 Methods and Approach

5.2.1 Burgisser and Gardner (2005)

The conditions used for the ABG samples can be found in chapter 2, section 2.5. Each sample has the same initial temperature (T_i), and initial pressure (P_i) to match the Burgisser and Gardner (2005) requirement to investigate bubble textures post-equilibrium. The samples vary in terms of final pressure (P_f) and the decompression rate ($dPdt$).

The composition, solubility, diffusivity, viscosity, and Equation of State (EOS) function all follow the same functions applied to sample ABG1 and ABG14 in chapter 4. These functions are the Panum Crater Dome composition (Mangan and Sisson, 2000), the Liu et al. (2005) solubility model, the Zhang and Ni (2010) diffusivity model, the Giordano et al. (2008) viscosity model and the Ideal Gas Law (EOS) model. Identical values are used for surface tension and melt density as determined for a typical rhyolitic composition (0.22Nm^{-1} (McBirney and Murase, 1978; Hajimirza et al. 2019) and 2350kgm^{-3} (Lesher and Spera, 2015)). The cooling rate is kept constant at 100Ks^{-1} which is standard for a decompression investigation (Berndt et al., 2002).

Other required variables for the numerical model are reported below. Bubble Number Density (N_b) is recorded by Coumans et al. (2020) and varies for each sample (table 5.1). Initial gas volume fraction (ϕ_i), initial bubble radius (r_i) and initial water content (H_2O_i) are all calculated using the equilibrium calculations discussed in chapter 3. These values are listed in table 5.1.

Sample	N_b (× 12m^{-3})	ϕ_i (-)	r_i (μm)	H_2O_i (wt.%)
ABG2	1.7	0.11075	26.0	3.97
ABG6	1.0	0.11076	31.0	3.97
ABG14	2.2	0.11075	23.8	3.97
ABG15	1.4	0.11076	27.7	3.97

Table 5.1 Experimentally observed N_b as reported by Burgisser and Gardner (2005). Initial gas volume fraction (ϕ_i), initial bubble radius (r_i), and initial H_2O content (H_2O_i) are calculated using the equilibrium calculation discussed in chapter 3.

N_b is a stochastic variable for Burgisser and Gardner (2005) and is recorded based on thin section images and is different for each sample, implying that a change in N_b may also alter the amount of resorption that occurs in each sample. N_b is an important influence in resorption because it determines the length scale of diffusion of H_2O, the evolution of the volume fraction of bubbles, and of the degree of H_2O supersaturation during magma ascent (Mourtada-Bonnefoi and Laporte, 2004). With increasing N_b, bubbles may become more tightly packed and the shell of melt surrounding each bubble thins (Chouet et al., 2006).

Newton cooling with a set initial $dTdt$ is chosen as the most appropriate cooling path. This is because newton cooling is a more realistic representation of experimental cooling conditions (Balmforth and Craster, 2000; Deschamps et al., 2014; Chaussard, 2016). The reason the newton cooling path with a set $dTdt$ is chosen over newton cooling with a set time to the glass transition temperature (T_g) is because newton cooling with a clear link to the cooling rates as described with the linear cooling is better and simplifies the process while still creating a more accurate pathway.

The changing pressure and temperature variables for the decompression experiments are displayed in figure 5.1. The Burgisser and Gardner (2005) experimental is divided into four stages of bubble growth and resorption.

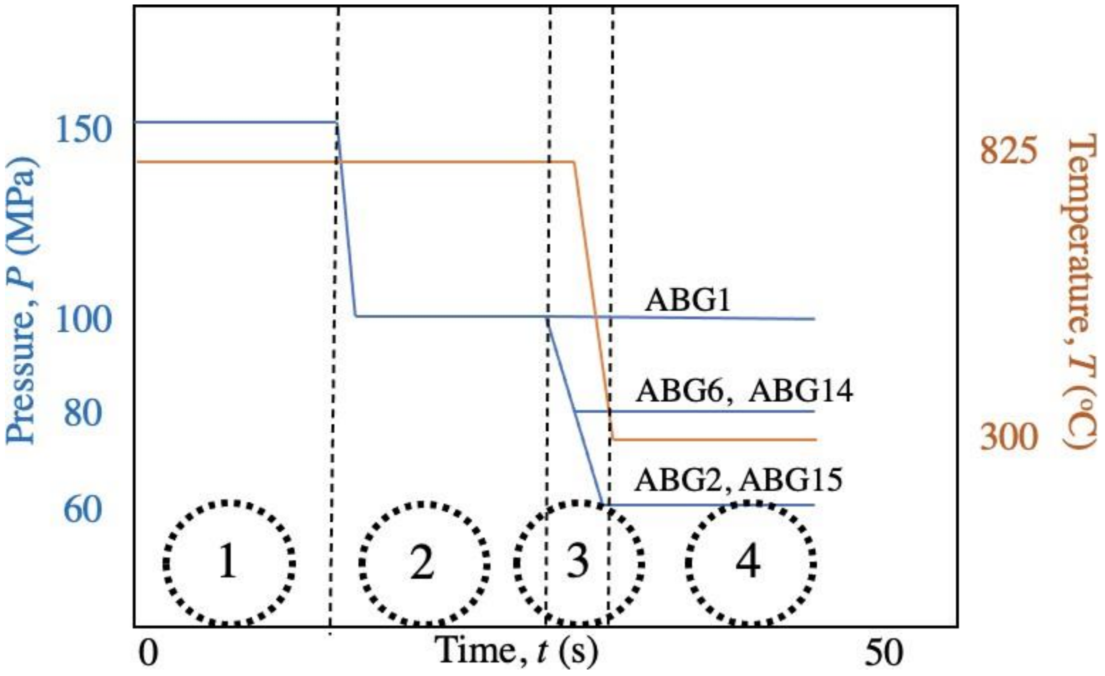

Figure 5.1 *The four stages of the Burgisser and Gardner (2005) decompression experiment. Stage 1: Bubbles are formed in equilibrium with the surrounding melt at* $150MPa$*. Stage 2: Pressure is decreased to* $100MPa$ *as bubbles form due to a decrease in solubility. The bubbles are then held in equilibrium to allow an equilibrium population of bubbles to stabilise. Stage 3: As pressure is decreased to* $100MPa$*, solubility also decreases, this is where ABG1 is held. However, ABG2, ABG6, ABG14 and ABG15 experience a further decrease in pressure. Temperature is also decreased from* 825℃ *to* 300℃ *during quench. The quench pathway occurs in the form of the newton cooling with a set to initial* $dTdt$*. Stage 4: Due to the rapid quench, there is an increase in the* H_2O *content. By the end of the decompression experiment, the* H_2O *content has stabilised and no more bubble growth/resorption occurs.*

5.2.2 McIntosh et al. (2014)

McIntosh et al. (2014) use the Burgisser and Gardner (2005) samples to obtain H_2O data following Humphreys et al. (2008): Secondary Ion Mass Spectrometry (SIMS) H_2O analyses is used to calibrate greyscale values in Backscatter Scanning Electron Microscope (BSEM) images. This H_2O data is used to make conclusions about resorption levels in the ABG samples.

Samples are prepared for BSEM images by embedding in epoxy resin and grinding to expose a flat surface to expose glass and infilled vesicles. Qualitative H_2O variations can then be seen in greyscale images where dark glass represents H_2O-rich and light glass represents H_2O-poor content.

For SIMs analysis, $^{1}H^{+}$, $^{23}Na^{+}$ and $^{28}Si^{+}$ are analysed in radial profiles and H_2O concentration is calculated from a working curve of $^{1}H^{+}/^{28}Si^{+}$. For each sample, multiple radial profiles are extracted around multiple vesicles and a composite dataset of H_2O as a function of distance from the vesicle wall is created.

Fourier Transform Infra-Red (FTIR) analysis is also undertaken. Samples are prepared as free-standing wafters and individual spectra are extracted from images and H_2O concentration is calculated by entering the height (absorbance) of the relevant peak above a linear background into the Beer-Lambert law (Stolper, 1982).

These methods allow McIntosh et al. (2014) to calculate the H_2O content of the ABG samples. These results will be used as a comparison to the model results later in this chapter.

5.3 Results

5.3.1 ABG Samples

For each sample which experiences bubble growth, the sample also experiences some level of resorption (figure 5.2). There is a change in ϕ after the maximum ϕ (ϕ_p) is reached and the water content profiles demonstrate a curvature which illustrates how the water has diffused into and then out of the bubble. There are two quantities that vary across the runs: final pressure (P_f) and decompression rate $(dPdt)$.

5.3.2 Changing Final Pressure

The samples ABG2 and ABG6 are subject to different P_f but have the same decompression rate (0.1MPas^{-1}). Based on the model outputs (figure 5.2), ABG2 which has a P_f of 60MPa, experiences more bubble growth over double the amount of time that sample ABG6 takes to grow. ABG2 has the larger pressure drop and grows to a ϕ_p of 0.276 (figure 5.2A) before resorbing at 400 seconds. In comparison, ABG6 (figure 5.2C) grows to a ϕ_p of 0.164 before resorbing at 200 seconds. When looking at the water content profiles, ABG2 (figure 5.2B) displays a greater decrease in water concentration at the far edge of the shell, at 0 seconds the water content is at 3.96wt.% before decreasing to 3.10wt.% by 400 seconds. ABG6 (figure 5.2D) displays a much smaller decrease in water concentration, from 3.96wt.% at 0 seconds to 3.68wt.% at 200 seconds.

ABG2 resorbs more than ABG6, with a $\Delta\phi$ of 0.036 (figure 5.2A) while ABG6 only resorbs by 0.029 (figure 5.2C), this is also reflected in the water concentration closest to the bubble wall where ABG2 displays a more gradual gradient as the water concentration increases back up from 3.10wt.% to 3.86wt.% in 7.6 seconds. ABG6 experiences a steeper gradient during resorption, as water concentration increases from 3.68wt.% to 4.44wt.% in 5.7 seconds.

ABG2

A.

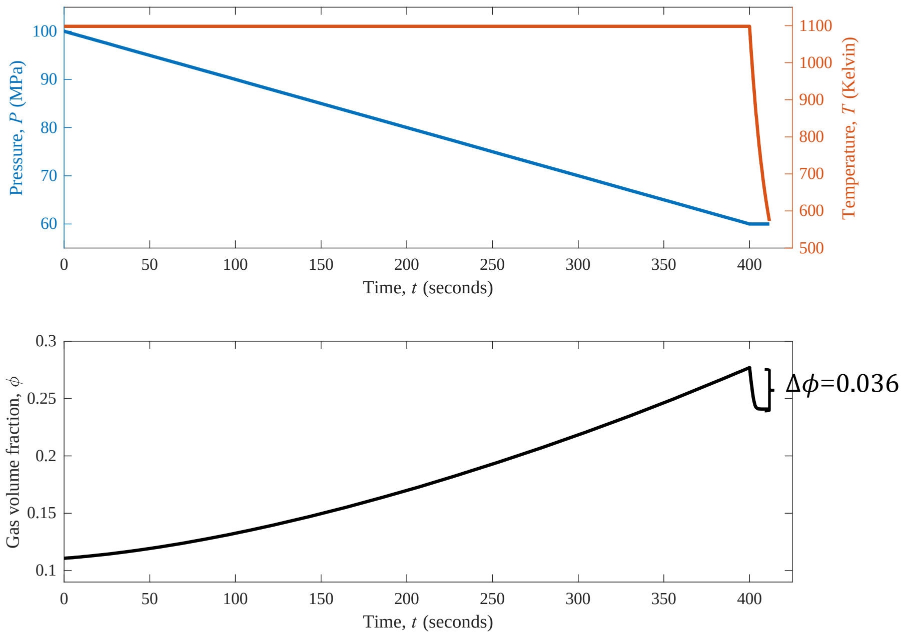

Pressure, P (MPa)
100
90
80
70
60
Temperature, T (Kelvin)
1100
1000
900
800
700
600
500
0
50
100
150
200
250
300
350
400
Time, t (seconds)
Gas volume fraction, ϕ
0.3
0.25
0.2
0.15
0.1
$\Delta\phi$=0.036
0
50
100
150
200
250
300
350
400
Time, t (seconds)

B.

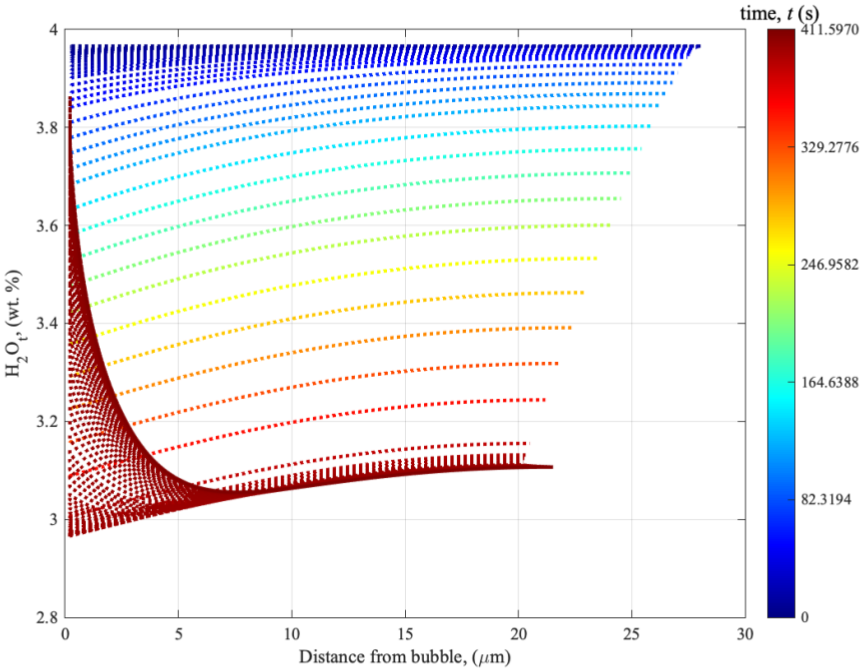

time, t (s)
411.5970
329.2776
246.9582
164.6388
82.3194
0
H_2O_t, (wt. %)
4
3.8
3.6
3.4
3.2
3
2.8
0
5
10
15
20
25
30
Distance from bubble, (μm)

ABG6
C.

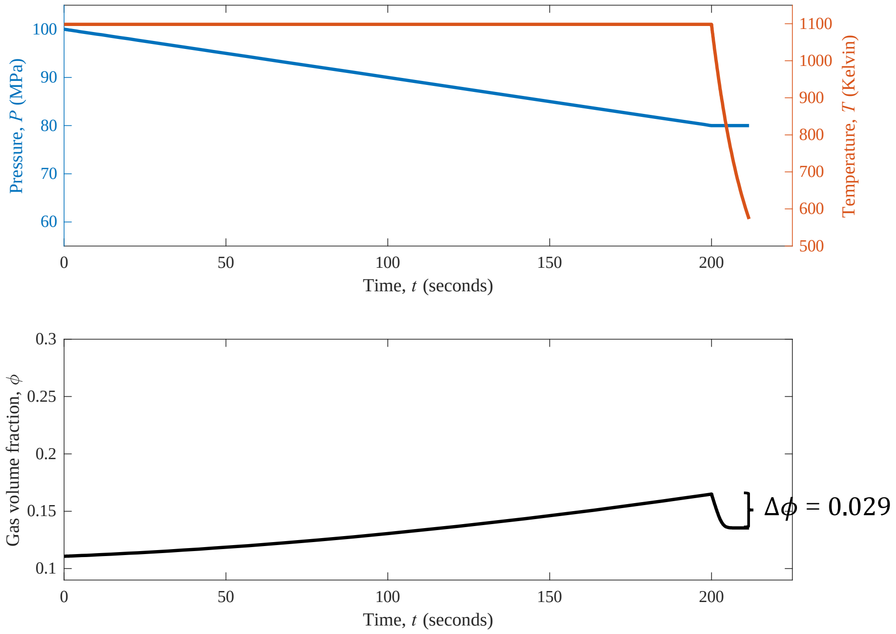

D.

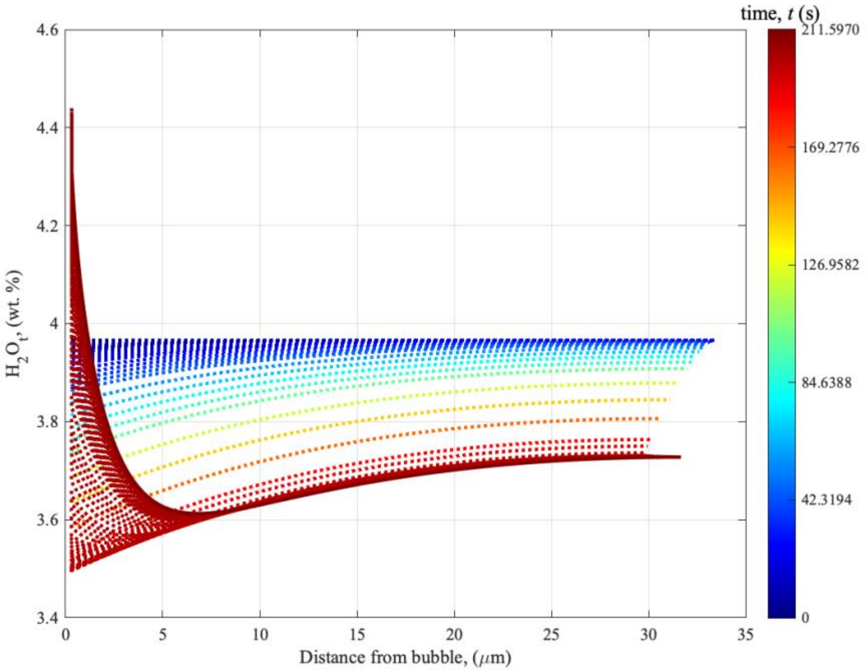

Figure 5.2 The gas volume fraction (ϕ) and water concentration profiles for samples ABG2 and ABG6. The $\Delta\phi$ is displayed on each gas volume fraction profile.

5.3.3 Changing Decompression Rate

ABG15 and ABG14 have a decompression rate of 0.5MPas^{-1} while ABG2 and ABG6 have a decompression rate of 0.1MPas^{-1}. ABG15 and ABG14 also have similar final pressure values of 60MPa and 80MPa respectively. A notable difference is that the experiments complete in a much shorter time, with ABG15 (figure 5.3A) growing and resorbing within 85 seconds while ABG14 (figure 5.3C) grows and resorbs within 47 seconds. This is expected with a higher decompression rate. In terms of growth, ABG2 and ABG15 which share the same P_f experience similar levels of growth, with ABG15 (figure 5.3A) growing by 0.117 before resorbing at 80 seconds. ABG14 grows by 0.040 before resorbing at 40 seconds. The water concentration profiles display similar patterns to figure 5.2, ABG15 experiences a larger decrease of water concentration (figure 5.3B) (0.323wt.%) than ABG14 (figure 5.3D) (0.081wt.%).

In terms of resorption, again there is a clear alignment of final pressure values with the ϕ of ABG15 decreasing by 0.032 from $80 - 85$ seconds. ABG14 experiences a $\Delta\phi$ of 0.028 between $40 - 45$ seconds. When looking at the water concentration values during resorption, ABG15 displays a shallower gradient, increasing from 3.610wt.% to 3.864wt.% while ABG14 displays a steeper gradient as the water concentration increases from 3.859wt.% to 4.490wt.%.

A faster decompression rate (0.5MPas^{-1}) leads to a more curved water concentration profile during growth compared to the slower decompression rate (0.1MPas^{-1}).

ABG15

A.

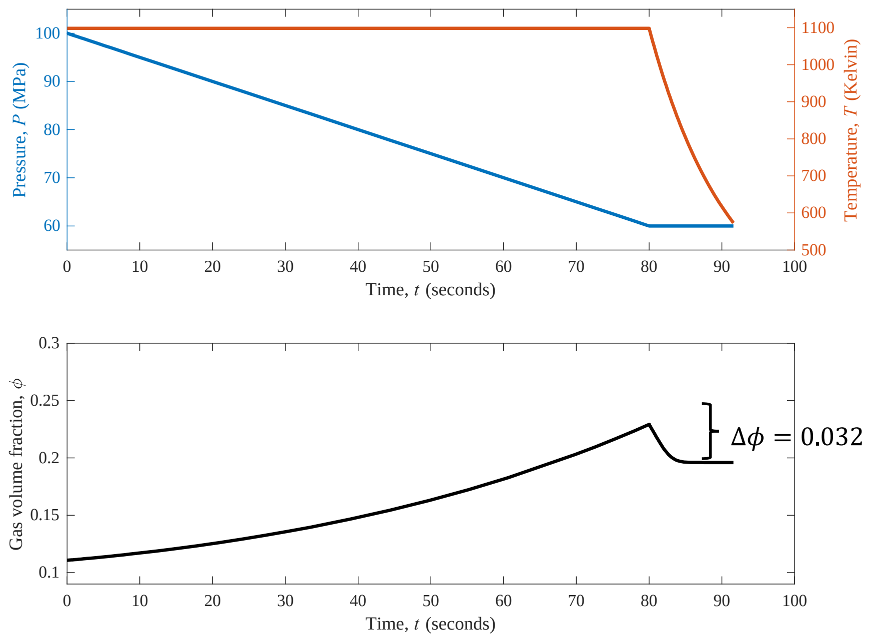

Pressure, P (MPa)
100
90
80
70
60
1100
1000
900
800
700
600
500
Temperature, T (Kelvin)
0
10
20
30
40
50
60
70
80
90
100
Time, t (seconds)
Gas volume fraction, ϕ
0.3
0.25
0.2
0.15
0.1
Δϕ = 0.032
Time, t (seconds)

B.

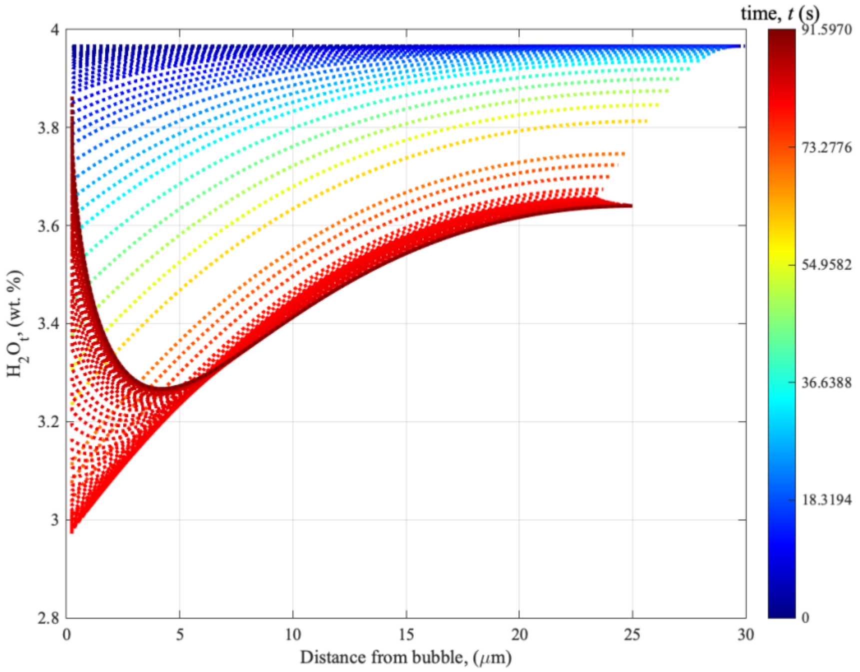

time, t (s)
91.5970
73.2776
54.9582
36.6388
18.3194
0
H2Ot, (wt. %)
4
3.8
3.6
3.4
3.2
3
2.8
0
5
10
15
20
25
30
Distance from bubble, (μm)

ABG14

C.

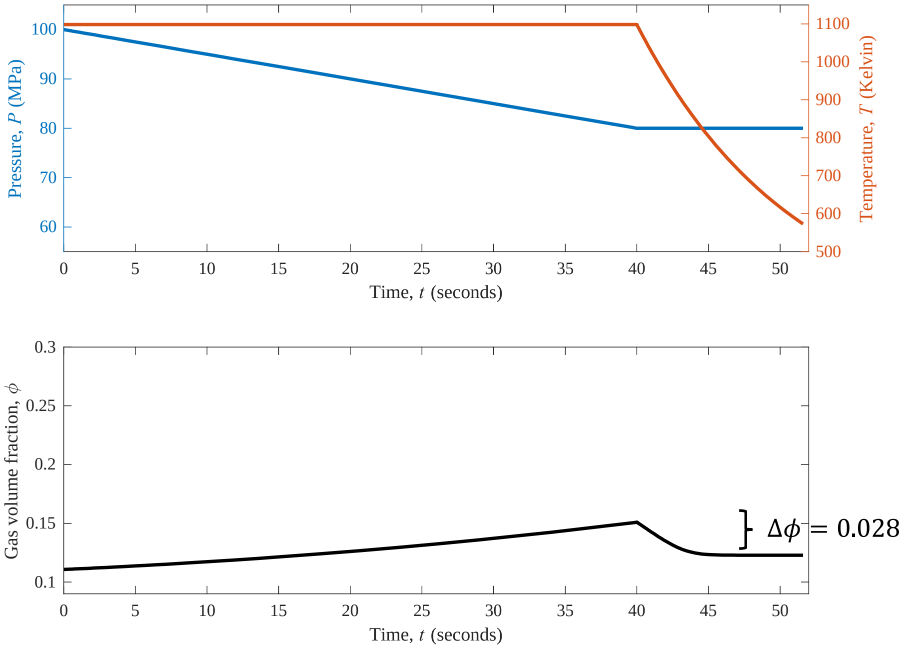

D.

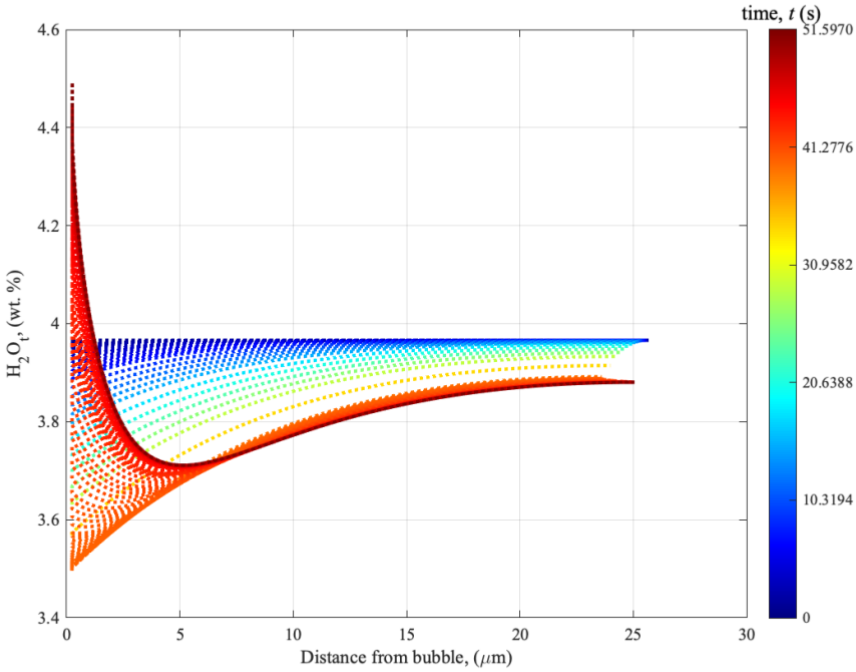

Figure 5.3 The gas volume fraction (ϕ) and water concentration profiles of samples ABG15 and ABG14. $\Delta\phi$ is displayed in each gas volume fraction profile.

5.3.4 Final Pressure vs. Decompression Rate

It is important to consider if a change in P_f plays a more important role in levels of growth and resorption compared to decompression rate. The results of ABG2 and ABG6 are very similar to ABG15 and ABG14 but a higher decompression rate is associated with a smaller increase in ϕ during growth. This will be expanded upon in the discussion.

5.4 Discussion

5.4.1 Changing Final Pressure

The degree is which quench modifies the change in ϕ depends on the different conditions each sample experiences. The experimental conditions for the ABG samples are varied by Burgisser and Gardner (2005) to look at the effect on bubble textures but, in this instance, it is important to look at how these conditions affect resorption.

The larger the pressure drop the greater the amount of gas exsolved, the greater the bubble growth, and the higher the ϕ (figure 5.2). Bubble growth is non-linear with time, increasing as the pressure continues to drop – even as the pressure drop itself remains linear – this is due to several reasons:

1) as the bubble grows, the melt shell thins and so the viscous resistant to growth drops,
2) as the melt shell thins, the distance the water has to diffuse to reach the bubble also drops,
3) as the bubble grows, the surface area available for exsolution of water increases and,
4) as the solubility progressively drops, the concentration gradients in the water profiles get steeper, driving water more rapidly into the bubble.
5) In figure 5.2B and D, the bubbles are still growing at the point that the temperature starts to drop but then rapidly shrink. The timing of the temperature drop is directly associated with the increase in solubility at the bubble wall and the reversal of the concentration profile as water moves back into the melt, driven by thermal resorption.

When comparing decompression rates, for faster decompression, the bubbles are further out of equilibrium as evidenced by the more strongly curved water profiles and thus grow more rapidly. As the final pressure is reached the fast decompression bubbles do not grow as much at the end of decompression as the slower decompression bubbles do. This is also seen in the water profiles, as the total amount of water still dissolved in the melt is much higher. The bubbles have grown less during faster decompression, so the total resorption is less as there is less water to resorb.

To investigate how important P_f values are on bubble growth and resorption, a sweep of P_f values ranging from $25 - 95$MPa are used when running simulations of sample ABG14. The ϕ profiles with changing P_f are displayed in figure 5.4. Bubble growth decreases with increasing P_f (figure 5.4A), 25MPa has a ϕ_p of 0.56 while 95MPa has a ϕ_p of 0.093. This decrease is in a non-linear shape, as the smaller final pressures have the greatest differences in ϕ_p between them. This follows the trend seen in figure 5.2A and C, as the larger the pressure drop, the greater the amount of gas exsolved and so the greater the bubble growth.

The lowest and highest final pressures create the least amount of bubble resorption (25MPa has a $\Delta\phi$ of 0.023 (figure 5.4B and 5.5A) while 95MPa has a $\Delta\phi$ of 0.025) this is because at high pressure drops the bubbles have grown by a large amount due to the greater amount of exsolved gas. There is also evidence for more growth in the water profiles as there is a large decrease of water content as water moves away from the melt due to a larger increase in solubility. Despite there being a huge amount of growth, there is a very small amount of resorption which is contrary to what is seen in figure 5.2. This suggests that there is a point where there can be too much of a pressure drop to cause substantial resorption. This is due to the change in volume being non-linear, when considered in terms of ϕ.

The highest $\Delta\phi$ occurs at 50MPa with a value of 0.036 (figure 5.4B and 5.5C). The bubble grows rapidly as P_f is reached, as evidenced by the higher reversal of the concentration gradient in figure 5.5D. Although the bubbles have grown less during the smaller pressure drops, a higher total resorption is recorded.

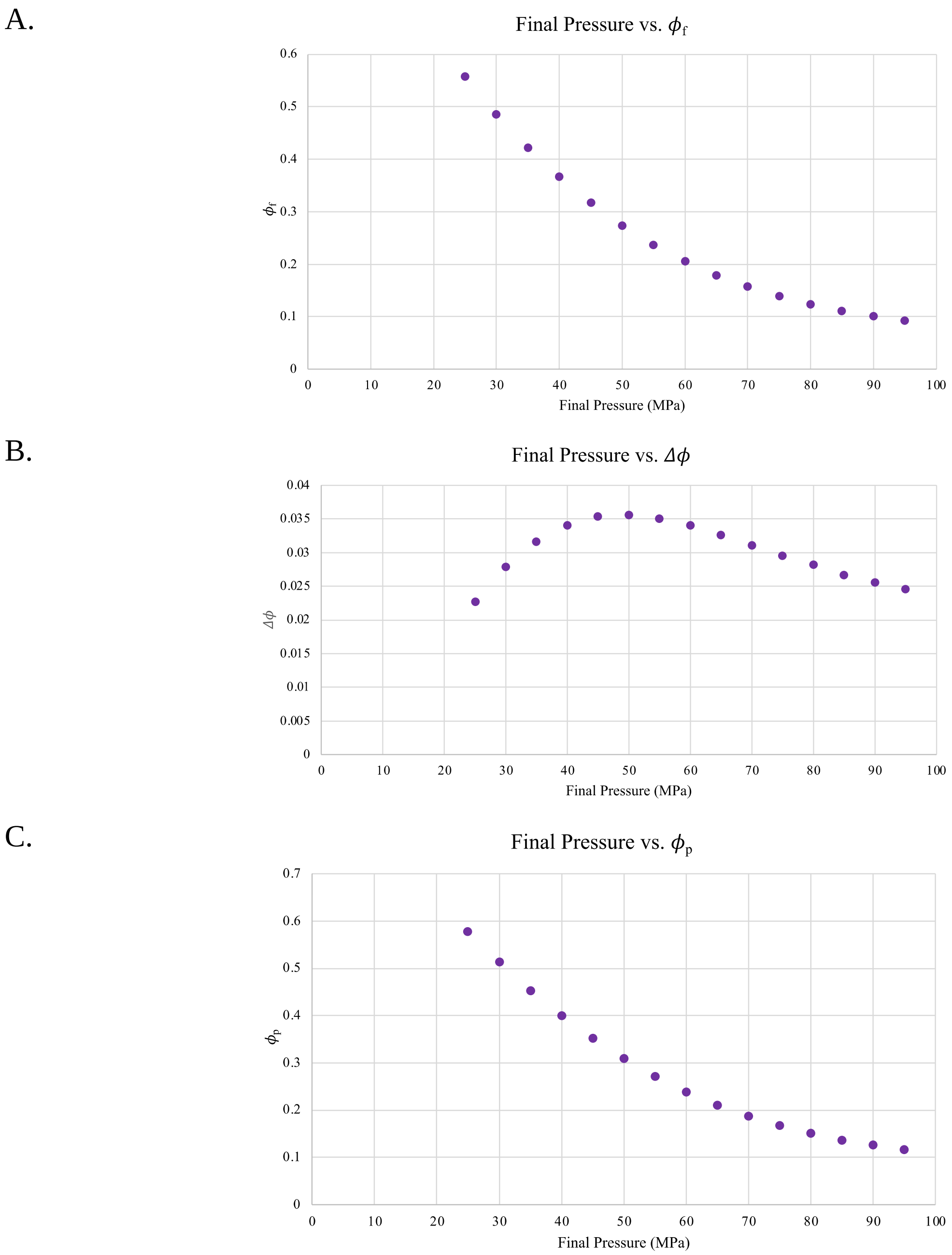

Figure 5.4 The changing ϕ with varying final pressures for sample ABG14. A. Final pressure vs. the final gas volume fraction reached. B. Final pressure vs. $\Delta\phi$, and C. final pressure vs. the peak gas volume fraction reached during growth.

A.

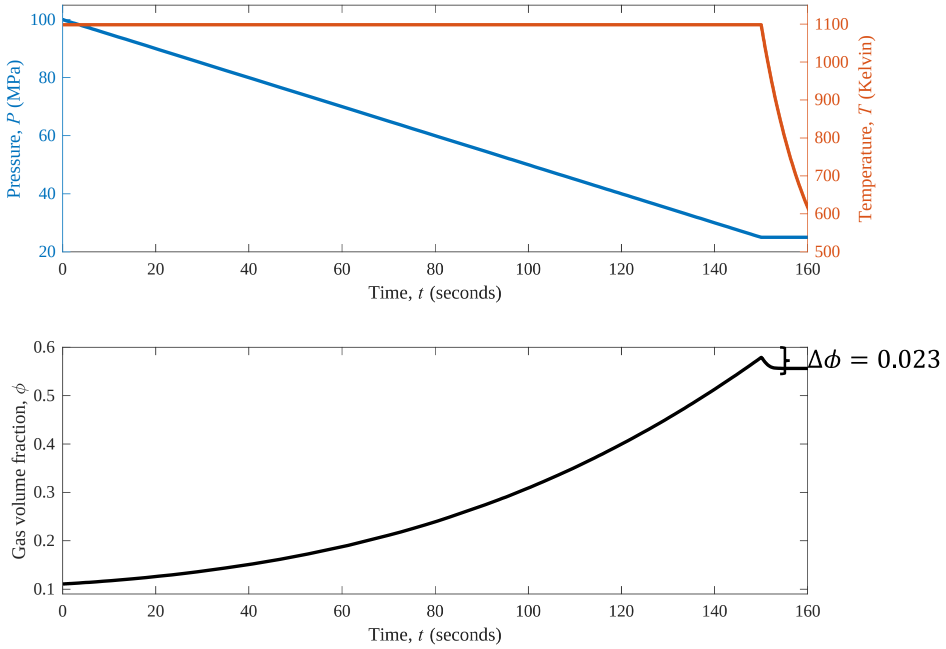
Pressure, P (MPa)
Temperature, T (Kelvin)
Time, t (seconds)
Gas volume fraction, ϕ
$\Delta\phi = 0.023$
100
80
60
40
20
1100
1000
900
800
700
600
500
0.6
0.5
0.4
0.3
0.2
0.1
0
20
40
60
80
100
120
140
160

B.

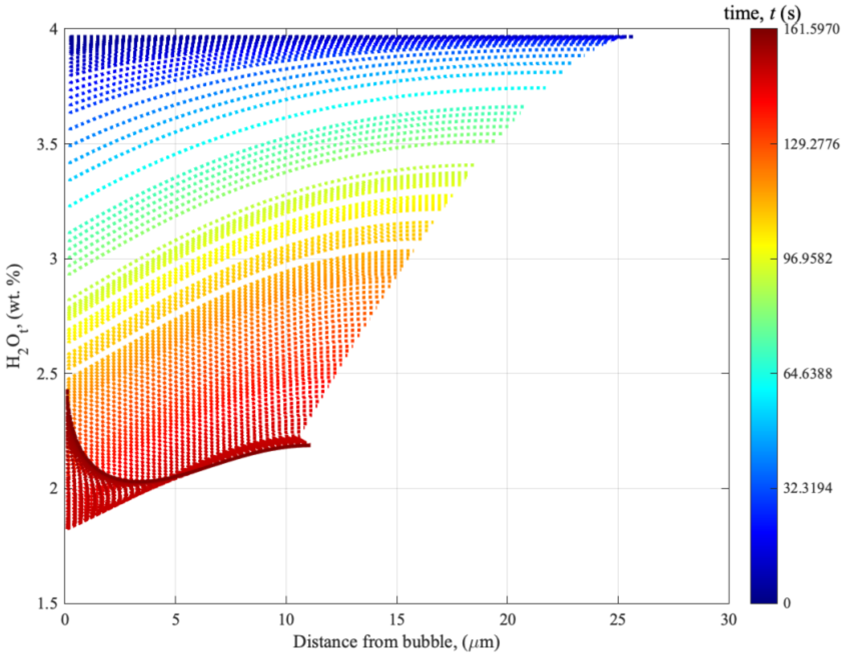
time, t (s)
161.5970
129.2776
96.9582
64.6388
32.3194
0
H_2O_t, (wt. %)
4
3.5
3
2.5
2
1.5
Distance from bubble, (μm)
0
5
10
15
20
25
30

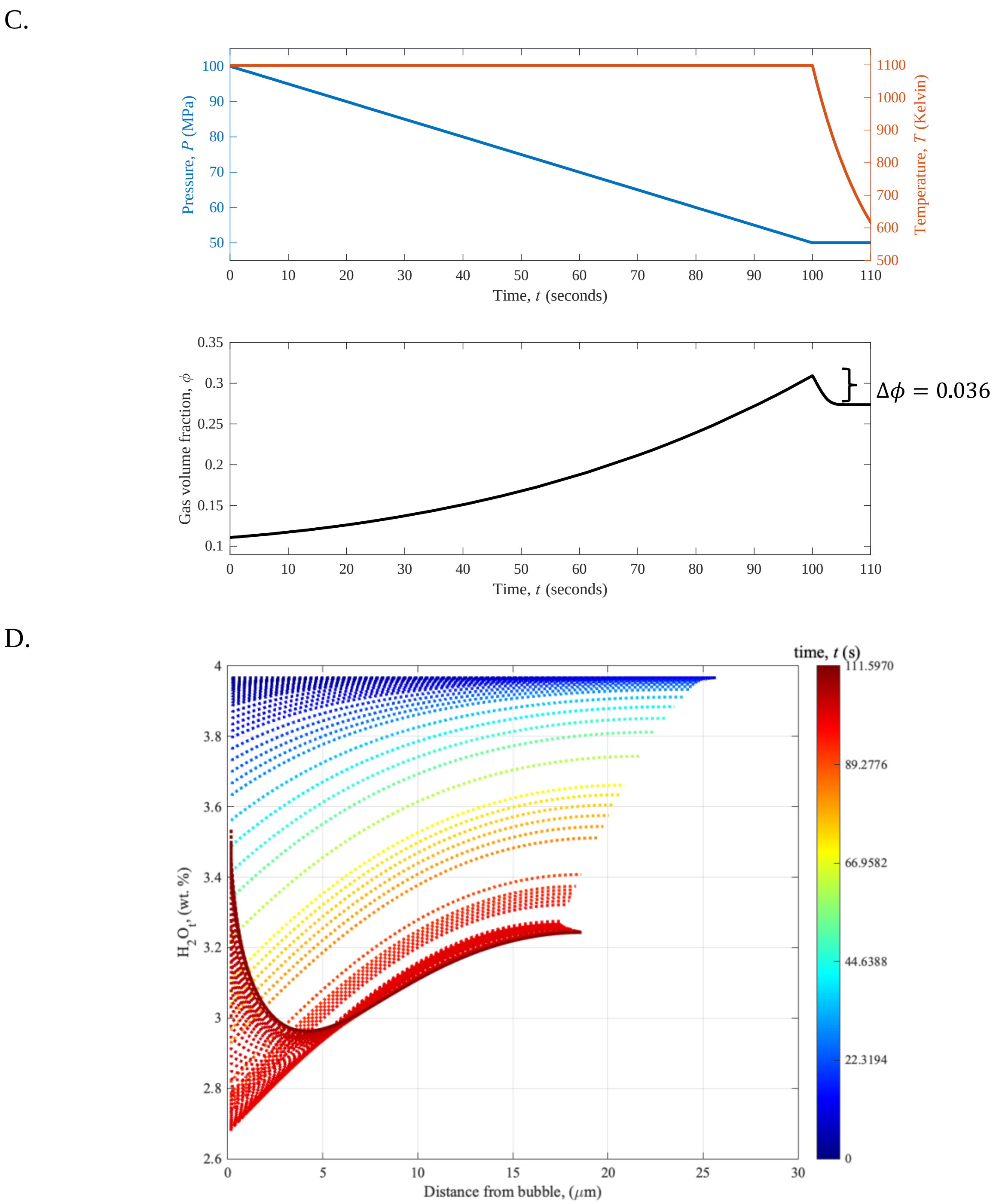

Figure 5.5 Sample ABG14 at different final pressures. A and B ABG14 with a P_f of $25MPa$ and C and D ABG14 with a P_f of $50MPa$

The steeper curve seen in figure 5.4A-C, suggests that at low and high pressures the level of resorption is reduced.

5.4.2 Changing Bubble Number Density

The N_b values for samples ABG2, ABG6, ABG14, and ABG15 are varied from $1.7 - 2.2 \times 10^{12}$m^{-3}. In decompression experiments, N_b values are based on the experimental pressure and temperature values chosen. Here, a range of N_b values will be run using the numerical model, investigating how much of a difference changing N_b values have on bubble growth and resorption. A large range of N_b values are chosen because N_b values of $> 10^{16}$m^{-3} have been typically recorded in experimental investigations (Mangan and Sisson, 2000; Martel and Schmidt, 2003; Hajimirza et al., 2019).

High and low N_b values should be accounted for in experimental investigations to take into consideration the various possible natural phenomena that may occur. Higher N_b values may suggest two successive nucleation events (Mourtada-Bonnefoi and Laporte, 2004) or a singular major nucleation event (Hamada et al., 2010). Low N_b values suggest minimal resorption which aligns with the current understanding of bubble densities. For a low N_b, the average distance between adjacent bubbles and the diffusion timescale is large (Toramaru, 2006; Martel and Iacono-Marziano, 2015; Hajimirza et al., 2019).

In this sweep following the conditions of ABG14, N_b values range from $9.8 \times 10^{10} - 2.8 \times 10^{15}$m^{-3} to investigate how they may influence bubble growth and resorption. The values increase in log-spaced increments. In general, there is a very small amount of bubble growth in these simulations due to the small pressure drop (20MPa) used.

Initially, an increase in N_b results in increased bubble growth (figure 5.6A), due to the diffusion length scale being shorter and because of the effect of thinning of the bubble wall as the bubble grows (Mangan and Cashman, 1996; Carey et al., 2013). However, this increase is only seen up to a N_b of 1.8×10^{14}m^{-3} and at this point the ϕ_f also decreases. Resorption increases at a steep rate (figure 5.6B) with an increasing N_b as the thinning of the bubble wall allows an increased volume of water to move back into the wall. For the smallest N_b value of 9.8×10^{10}m^{-3} there is a very small amount of growth of 0.028. Bubbles are out of equilibrium, as evidenced by the strongly curved water profiles and bubble growth increases as P_f is reached, as seen by the higher reversal of the concentration gradients. The bubble almost completely resorbs and as bubble growth was very small, there is less water to resorb. In comparison, the highest N_b value of 2.8×10^{15}m^{-3} experiences a bubble growth of 0.073 but also experiences more resorption. However, there is a much gentler water profile in figure 5.7D as equilibrium is reached much faster. Overall, the fractional amount of resorption compared to the growth is very similar for both N_b samples with the higher N_b value resorbing by 82% compared to its original bubble growth while the smallest N_b value resorbs by 90% compared to its original bubble growth. This is seen in figure 5.6C as the ϕ_p initially increases but once a N_b of 1.8×10^{14}m^{-3} is reached, has a very small rate of increase. ϕ_p increases as N_b increases because the bubble walls get thinner, so the bubbles get closer to equilibrium during decompression. These final ϕ_p values level off at high N_b because they are reaching (or very nearly reaching) equilibrium, so they cannot grow further. The amount of resorption always increases as N_b goes up because the thin walls mean that more of the water in the bubble can resorb over the quench interval. The result is that ϕ_f initially increases with an increasing N_b (because of the additional growth of the bubbles during decompression dominates), then, at higher N_b, it decreases with increasing N_b because the enhanced resorption effect dominates.

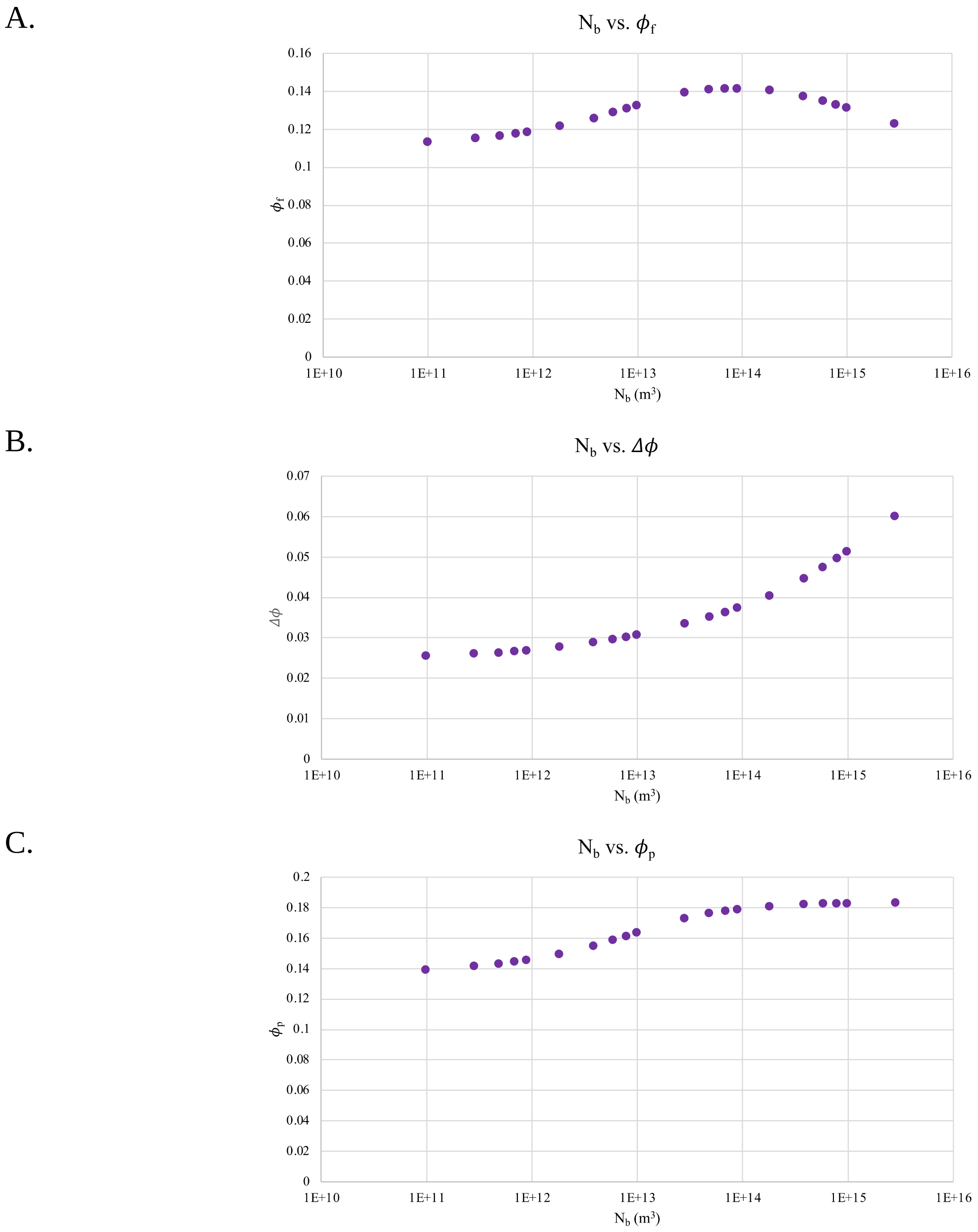

Figure 5.6 Changing bubble growth with an increase in N_b. A. an increase in N_b vs. ϕ_f, B. an increase in N_b vs. $\Delta\phi$, and C. an increase in N_b vs. ϕ_f.

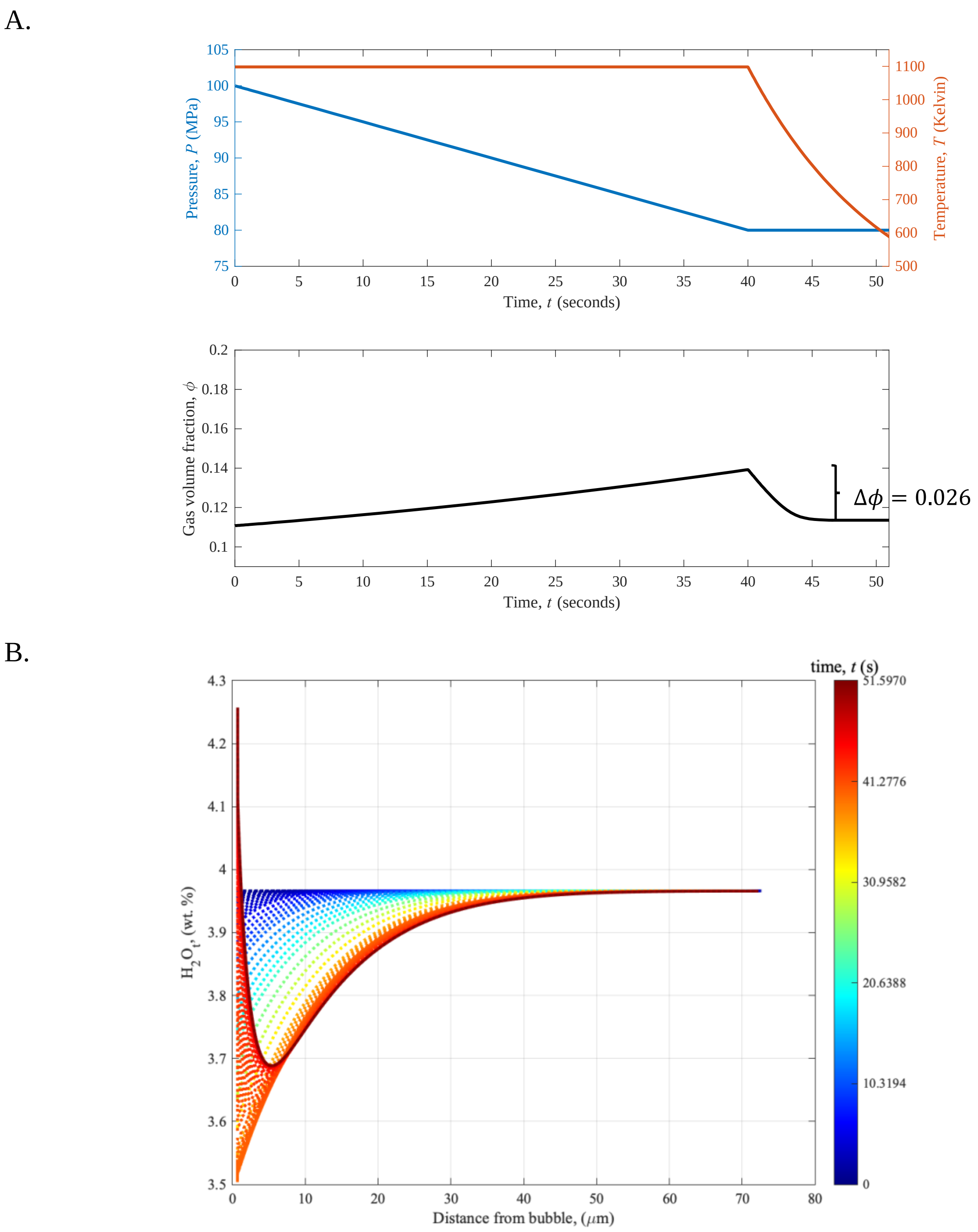
A.
Pressure, P (MPa)
105
100
95
90
85
80
75
Temperature, T (Kelvin)
1100
1000
900
800
700
600
500
Time, t (seconds)
0
5
10
15
20
25
30
35
40
45
50
Gas volume fraction, ϕ
0.2
0.18
0.16
0.14
0.12
0.1
$\Delta\phi = 0.026$
Time, t (seconds)
B.
H_2O_t, (wt. %)
4.3
4.2
4.1
4
3.9
3.8
3.7
3.6
3.5
Distance from bubble, (μm)
0
10
20
30
40
50
60
70
80
time, t (s)
51.5970
41.2776
30.9582
20.6388
10.3194
0

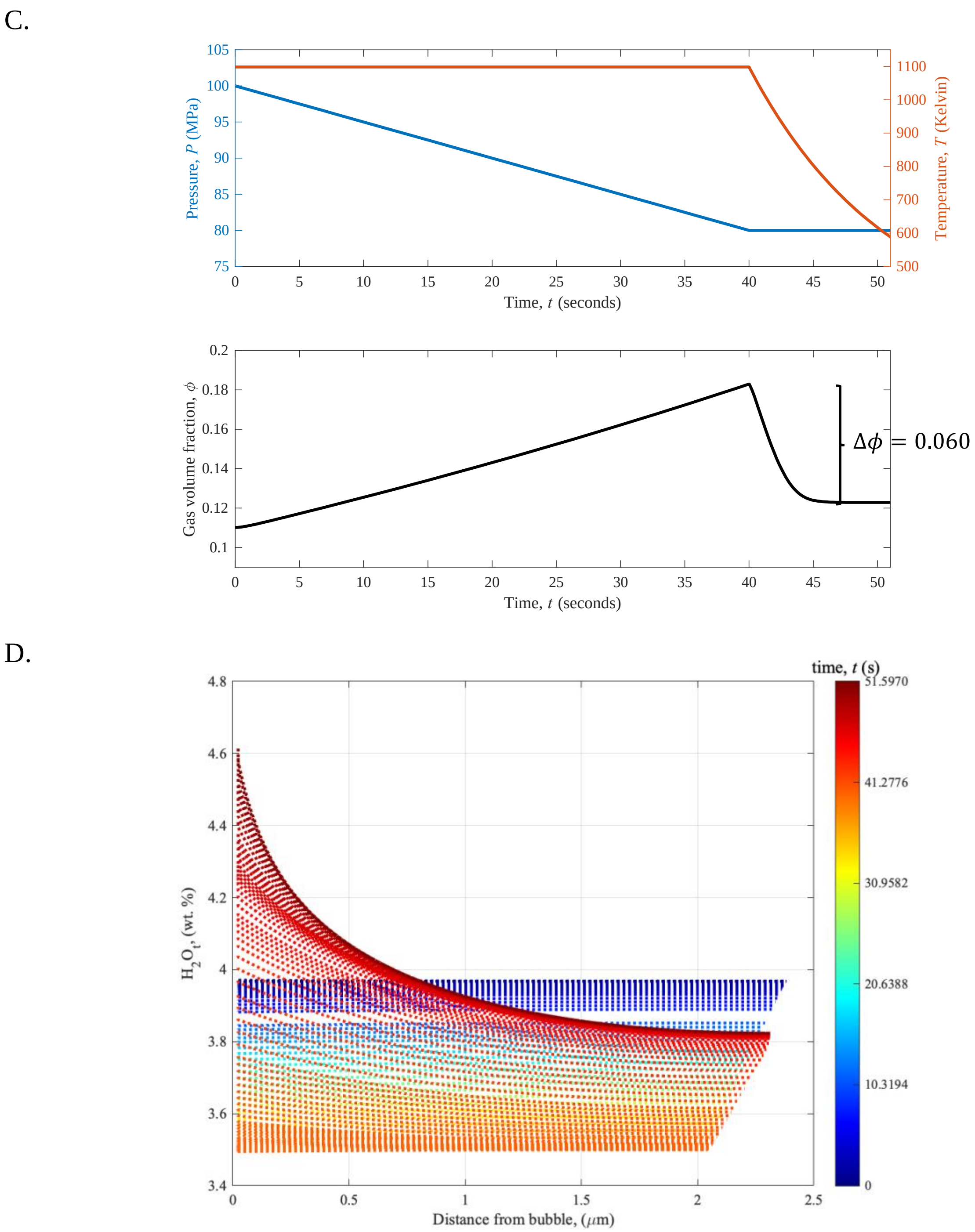

Figure 5.7 ABG14 with the conditions in table 2.1 but with varying values for N_b. A. and B. N_b value of 9.8×10^{10} *m^{-3} C. and D. N_b value of* 2.8×10^{15}*m^{-3}.*

A further understanding of how N_b affects resorption is important as N_b is a good marker for the decompression rate of magmas in volcanic conduits (Hamada et al., 2010) and is regularly used when evaluating bubble textures to further understand the process behind an eruption (Lyakhovsky et al., 1996; Gardner et al., 1999; Cluzel et al., 2008).

5.4.3 In Comparison to McIntosh et al. (2014)

McIntosh et al. (2014) finds similar results in terms of H_2O (wt.%) profiles for the ABG samples (figure 5.8A). The results are not identical (figure 5.8B-E), but they show similar trends where the H_2O concentration gradients are steeper at the vesicle wall and then reach a shallow gradient. The most notable difference is seen in sample ABG14 whereby the H_2O concentration measured by McIntosh et al. (2014) decreases from $5.4 - 5.25$ with distance from the bubble wall while the numerical model calculates a decrease in water concentration of $4.45 - 3.9$ with distance from the bubble wall. This trend is heightened when using the numerical model where there is a very steep trend at the final timestamp – when the distance from the vesicle wall is small. It is suggested that the difference between the values produced by McIntosh et al., 2015 and those predicted by the numerical model are due to errors when using SIMS (Regier et al., 2016; Taracsák et al., 2021). Alternatively, there could be small errors in the numerical model which do not account for the exact conditions of the Burgisser and Gardner (2005) experimental conditions.

McIntosh et al., 2014 have included error analysis in figure 5.8A, with the semi-opaque boundaries indicating twice the standard error of the mean (McIntosh et al., 2014). Error analysis should also be run on figure 5.8B to act as a comparison. Other potential sources of error in the numerical model calculations include the use of standard rhyolitic conditions for surface tension and density rather than using values specific to the composition used by Burgisser and Gardner, 2005. Assumptions are also made throughout the equilibrium bubble calculations (section 3.4.3) such as assuming conditions for an exact spherical bubble. It is also assumed that the bubble goes out of equilibrium as soon as the temperature drop begins.

To validate any experimental errors when applying previous experimental runs to the numerical model, it is suggested that the model should be applied to several other decompression experiments of an identical composition (the Panum Crater Dome) to confirm if disparities between experimental results and model results continue. Error analysis should also be carried out on the numerical model, including defining the uncertainty which surrounds using numerical models on experimental data.

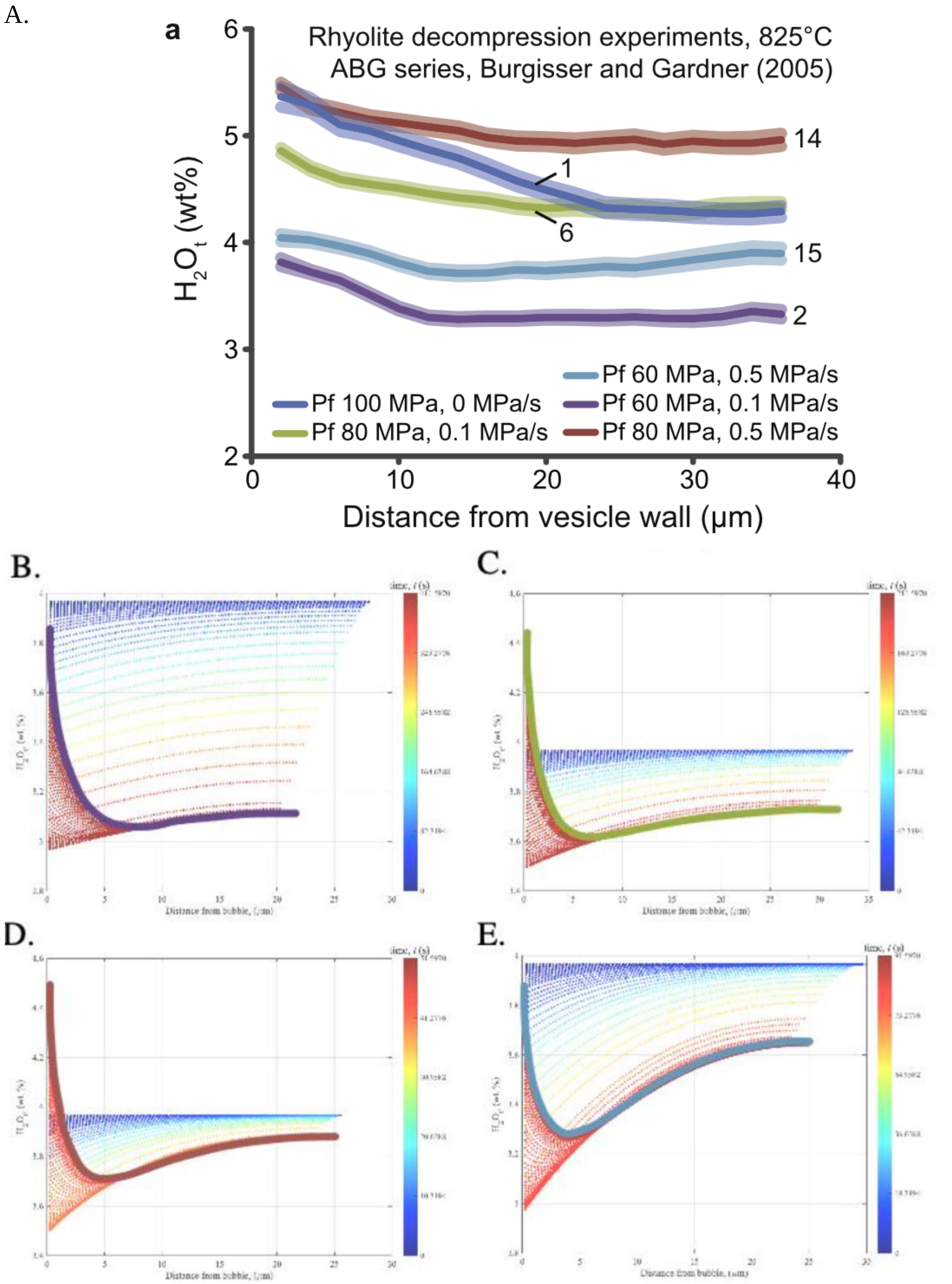

Figure 5.8. A. the results recorded by McIntosh et al., 2014. The changing water content is recorded for each sample against the distance from vesicle wall. The measurements are made using SIMS-calibrated H_2O concentration gradients. The colours of the different samples from the McIntosh et al., 2014 figure have been overlayed onto the numerical model water profiles. B. ABG2 water profile numerical model results. C. ABG6 water profile numerical model results. D. ABG14 water profile numerical model results. E. ABG15 water profile numerical model results.

It is suggested that if the disparities between the McIntosh et al. (2014) values and the numerical model values are calculated, a conversion equation can be used to determine how much the values differ between experimental and theoretical methodologies.

5.5 Conclusion

To determine if resorption does occur following the Burgisser and Gardner (2005) experiments, the four ABG samples looked at by McIntosh et al. (2014) are input into the numerical model. From initial observations, the ABG samples that experience the second decompression step undergo some level of bubble resorption. This resorption is not obvious in experimental results and may go unrecorded in published studies.

The larger the amount of resorption that occurs, the greater the error in experimental values of ϕ_f that can occur in the numerical model output. The level of resorption the ABG samples experience are dependent on a variety of factors. Depending on the final pressure chosen and the N_b of the sample, a higher or lower level of resorption may occur. In comparison to the McIntosh et al. (2014) results, similar resorption trends are seen, supporting conclusions made in this study.

In the next chapter, a full parametric investigation will be carried out to identify these conditions that are the most and least ideal for reducing bubble resorption.

6. Parametric Investigation of Quench Resorption

6.1 Introduction

Chapter 5 suggests that bubble resorption is influenced by several factors. Bubble Number Density (N_b), cooling rate ($dTdt$), initial pressure (P_0) and change in pressure (ΔP) are looked at simultaneously to determine the affect they have on resorbing bubbles.

A parametric sweep recognises broader trends in a much larger dataset (6561 rows of data) and allows for application to other decompression experiments as well as use in future studies. The table of results and mesh plots generated acts as a look-up table for the ideal conditions required to minimise the amount of resorption in future decompression experiments. When applying this parametric sweep to the natural environment, the amount of resorption that has occurred in a volcanic conduit can be calculated based on that conduit's estimated parameters.

For this study, the results of the parametric sweep will only be applicable to a rhyolite composition as the results are based on the experimental samples of Burgisser and Gardner (2005), but this methodology opens the possibility of application to a variety of compositions and scenarios. This will be explored in chapter 7.

6.2 Characteristics of the Parametric Sweep

A parametric sweep is an efficient experimental tool as it investigates several variables simultaneously, while incorporating an automatic sweep into the numerical model allows for an increase in computational efficiency.

Based on the results from chapter 4 and 5, N_b, $dTdt$, P_0 and ΔP are chosen as factors that most influence bubble growth and resorption. An increase in N_b is shown to increase bubble growth resulting in a changing diffusion length scale due to the thinning of the bubble wall (Mangan and Cashman, 1996; Carey et al., 2013), while a decrease in $dTdt$ causes an increase in bubble resorption as the longer cooling rate allows for an increase in water movement and bubble shrinkage. Chapter 5 also demonstrates the significance of pressure in controlling bubble size and how an increase in pressure drop causes an increase in bubble resorption due to the greater amount of gas exsolved. For this investigation, both P_0 and ΔP are changed which maximises the range of pressure values from initial pressures (P_i) of 125MPa to final pressures of 5MPa.

Each influencing factor has a range of 9 different values, creating 6561 possible combinations of data output ($9 \times 9 \times 9 \times 9$). This limit is chosen for the purpose of computational efficiency as just increasing the combinations to $10 \times 10 \times 10 \times 10$ creates $10{,}000$ possible combinations which would take too long for the timeline of this study. It is suggested that for any future studies, the combinations should be increased to improve model accuracy. The range of each influencing factor is shown in table 6.1. The range of values chosen are based on the typical ranges used in the lab as well as values found in nature.

N_b (m^{-3})	$dTdt$ (Ks^{-1})	P_0 (MPa)	ΔP (MPa)
7.2×10^{11}	0.5	105	20
2.2×10^{12}	1	110	30
6.2×10^{12}	2	115	40
1.2×10^{13}	5	120	50
5.2×10^{13}	10	125	60
9.2×10^{13}	20	130	70
4.2×10^{14}	50	135	80
3.2×10^{15}	100	140	90
8.2×10^{15}	200	145	100

Table 6.1 The ranges used when changing N_b, $dTdt$, P_0 and ΔP for the parametric sweep.

The N_b values chosen are different to the values used in chapter 5, although the range still extends to $> 8.5 \times 10^{15}$ to ensure consideration of experimental investigations (Mangan and Sisson, 2000; Martel and Schmidt, 2003; Hajimirza et al., 2019). The values increase in wider increments, compared to the range used in chapter 5. This allows a wider range of values to be sampled. N_b values range from $7.2 \times 10^{11} - 8.2 \times 10^{15}$m^{-3}.

For $dTdt$, the values range from $0.5 - 200$Ks^{-1}. The higher rates are more applicable to experimental conditions which is why the range does not extend to very slow cooling rates. The lowest cooling rates being used are more applicable to samples that may cool slowly in nature. For extremely low cooling rates, the numerical model produces an output of ‘bubble too small’, suggesting that at such low rates the bubble resorbs out of existence.

Experimental scenarios have extended to cooling rates as low as 0.08Ks^{-1} (Allabar et al., 2018) and 7.8Ks^{-1} (Browning et al., 2020) whilst other studies have utilised faster cooling rates such as 423Ks^{-1} (Buono et al., 2020) and 200Ks^{-1} (Burgisser and Gardner, 2005; Gardner, 2007). In this study, the cooling rates range from $0.5 - 200$Ks^{-1}.

Initially, a cooling rate range of $0.001 - 200$Ks^{-1} is used, however, a cooling rate of 0.001Ks^{-1} combined with high N_b values of $3.2 \times 10^{15} - 8.2 \times 10^{15}$m^{-3} produces a negative initial radius (r_i) values and a computational run time of $1 - 10$hours per combination run. To reduce this run time, the cooling rate range is adjusted to its current selection. The cooling rate increases logarithmically to cover as large a range as possible within 9 possible values. When inputting these variables into the numerical model it is the newton constant (k) values which are used, calculated from the $dTdt$ values, using equation (36).

The possible pressure values used range between $125 - 5$MPa, representing the common ranges used in decompression experiments as well as the pressure extremes that sometimes occur in natural scenarios (Martel and Iacono-Marziano, 2015; Gardner et al., 2018). This range is chosen because, based on figure 5.4B in chapter 5, it is suggested that as pressure increases, resorption decreases so investigating pressures beyond 125MPa will be obsolete. The scaling is in equal increments to cover all pressure values during this range based on results from chapter 5, pressures of $45 - 55$MPa seem to have the most influence on resorption so need to be covered during the parametric sweep.

The parametric sweep is chosen as the best method to cover the widest range of experimental conditions a sample may experience. For full details of the computational script for the parametric sweep see the appendix which provides sections of the relevant code required to carry out the full sweep. The full code is available as supplementary material. All parameters are entered into the model and a `combvec for loop` is set up to run through all 6561 possible combinations.

The full run time for the entire parametric sweep is 36 hours and following completion, an excel spreadsheet is produced automatically containing all combinations and the subsequent r_i, initial H_2O content (H_2O_i), initial gas volume fraction (ϕ_i), peak gas volume fraction (ϕ_p), and final gas volume fraction (ϕ_f). The resorption value ($\Delta\phi$) and fractional gas volume fraction (ϕ_{fr}) is calculated post-parametric sweep. ϕ_{fr} is defined as:

$$\phi_{fr} = \frac{\Delta\phi}{\phi_p}, \tag{39}$$

with a ϕ_{fr} of 1 meaning the bubble has fully resorbed.

6.3 Results

The parametric sweep successfully generated 6561 combinations of data results, however for roughly 100 rows of data, the combination of low cooling rate, high N_b and high-pressure values creates bubbles that 100% resorb and produce negative ϕ_f values. These negative values are corrected to zero for the purpose of noting complete resorption.

Following the complete run time, the output is analysed in MATLAB. Mesh grids are created to look at several influencing factors simultaneously. The results in figure 6.1 display the $\Delta\phi$, ϕ_f, ϕ_p and ϕ_{fr} against a changing N_b and $dTdt$. As the 2D mesh grids only allow three changing variables, the pressure remains set at two different extremes: a P_0 of 145MPa and ΔP of 20MPa (figure 6.1) and a P_0 of 145MPa and $\Delta\phi$ of 100MPa (figure 6.2).

For a P_0 of 145MPa and a ΔP of 20MPa, ϕ_p is highest for the high N_b values ($log_{10} > 15.0$) (figure 6.1A), this is because the diffusion length scale is shorter due to the thinning of the bubble wall as the bubble grows (Mangan and Cashman, 1996; Carey et al., 2013) and this is relevant across all cooling rates, although slightly more for lower cooling rates. The bubbles resorb more for high N_b values ($log_{10} > 13.7$) and low cooling rates ($log_{10} > 1.3$) (figure 6.1D), due to the influence of a thinning bubble wall, allowing an increased volume of water to move back into the bubble while lower cooling rates allow for more water to move from the melt shell into the bubble.

For a P_0 of 145MPa and a ΔP of 100MPa, a higher bubble growth is initiated at lower N_b values ($log_{10} > 13.0$) (figure 6.2A) at all cooling rates while the bubbles resorb less with higher N_b values ($log_{10} > 14.0$) and lower cooling rates ($log_{10} > -0.02$). This is because the greater the pressure drop (ΔP) the greater the amount of gas exsolved and so the greater the bubble growth and the higher the ϕ_p. While the larger the ΔP the less resorption occurs because the bubbles have grown by a large amount due to the greater amount of exsolved gas. Water moves from bubbles to the melt as there is a large increase in solubility. This is seen in figure 5.4B and 5.5A in chapter 5.

A.

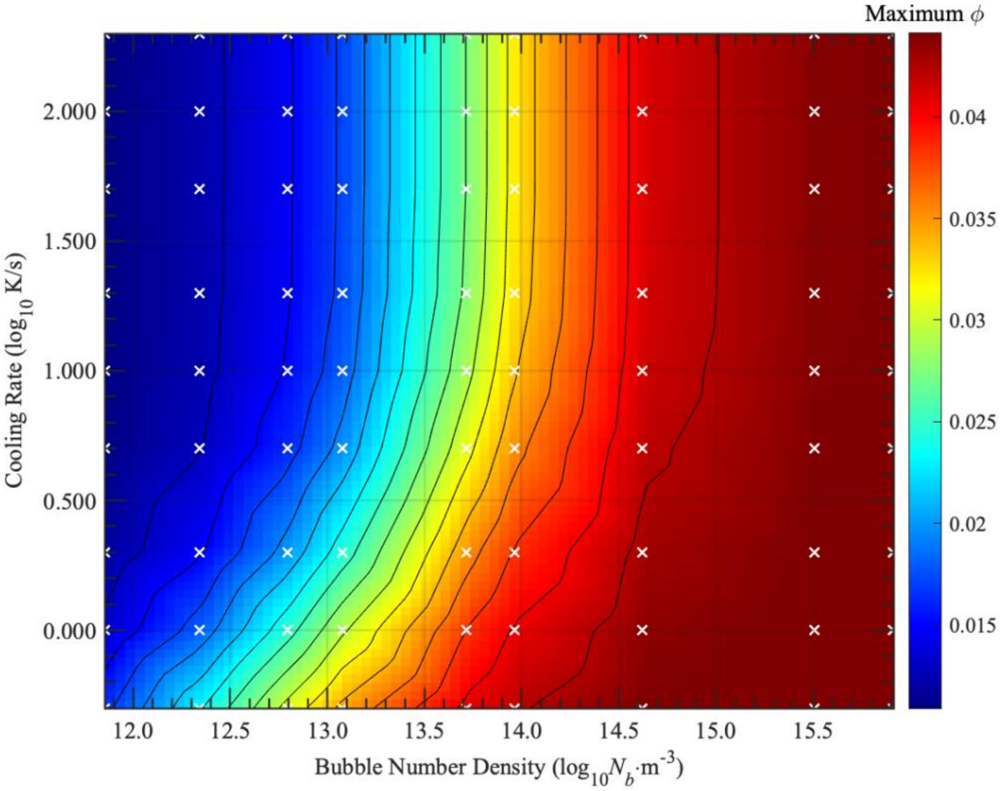
Maximum ϕ
0.04
0.035
0.03
0.025
0.02
0.015
Cooling Rate ($\log_{10}$ K/s)
2.000
1.500
1.000
0.500
0.000
12.0
12.5
13.0
13.5
14.0
14.5
15.0
15.5
Bubble Number Density ($\log_{10} N_b \cdot m^{-3}$)

B.

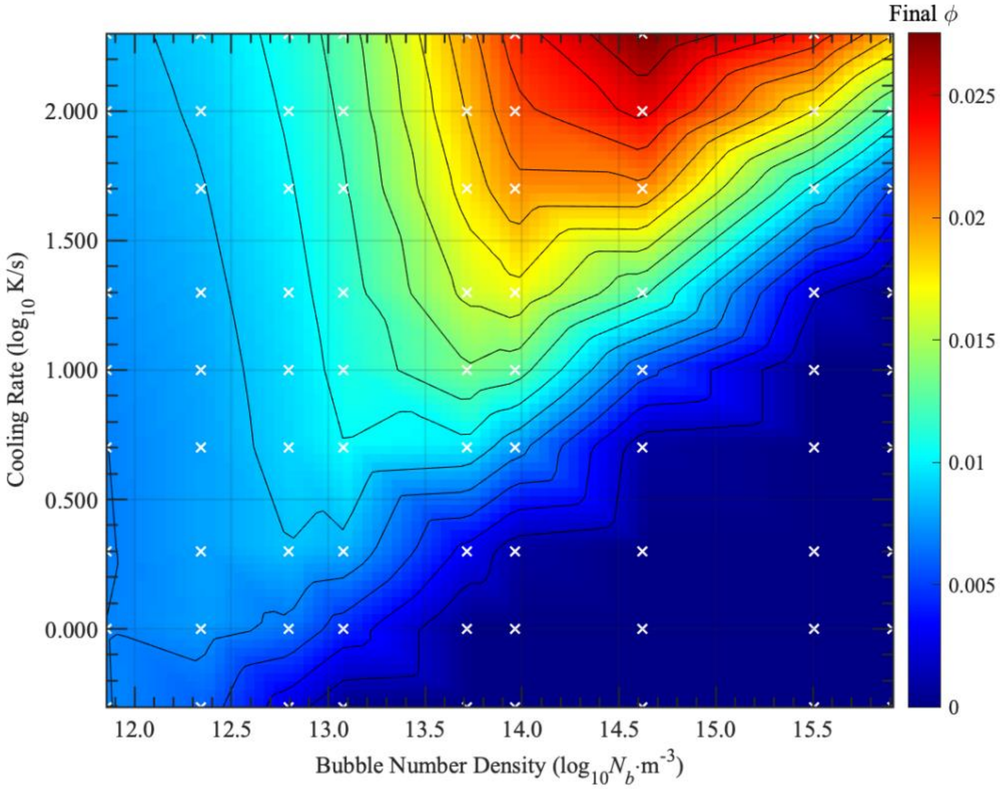
Final ϕ
0.025
0.02
0.015
0.01
0.005
0
Cooling Rate ($\log_{10}$ K/s)
2.000
1.500
1.000
0.500
0.000
12.0
12.5
13.0
13.5
14.0
14.5
15.0
15.5
Bubble Number Density ($\log_{10} N_b \cdot m^{-3}$)

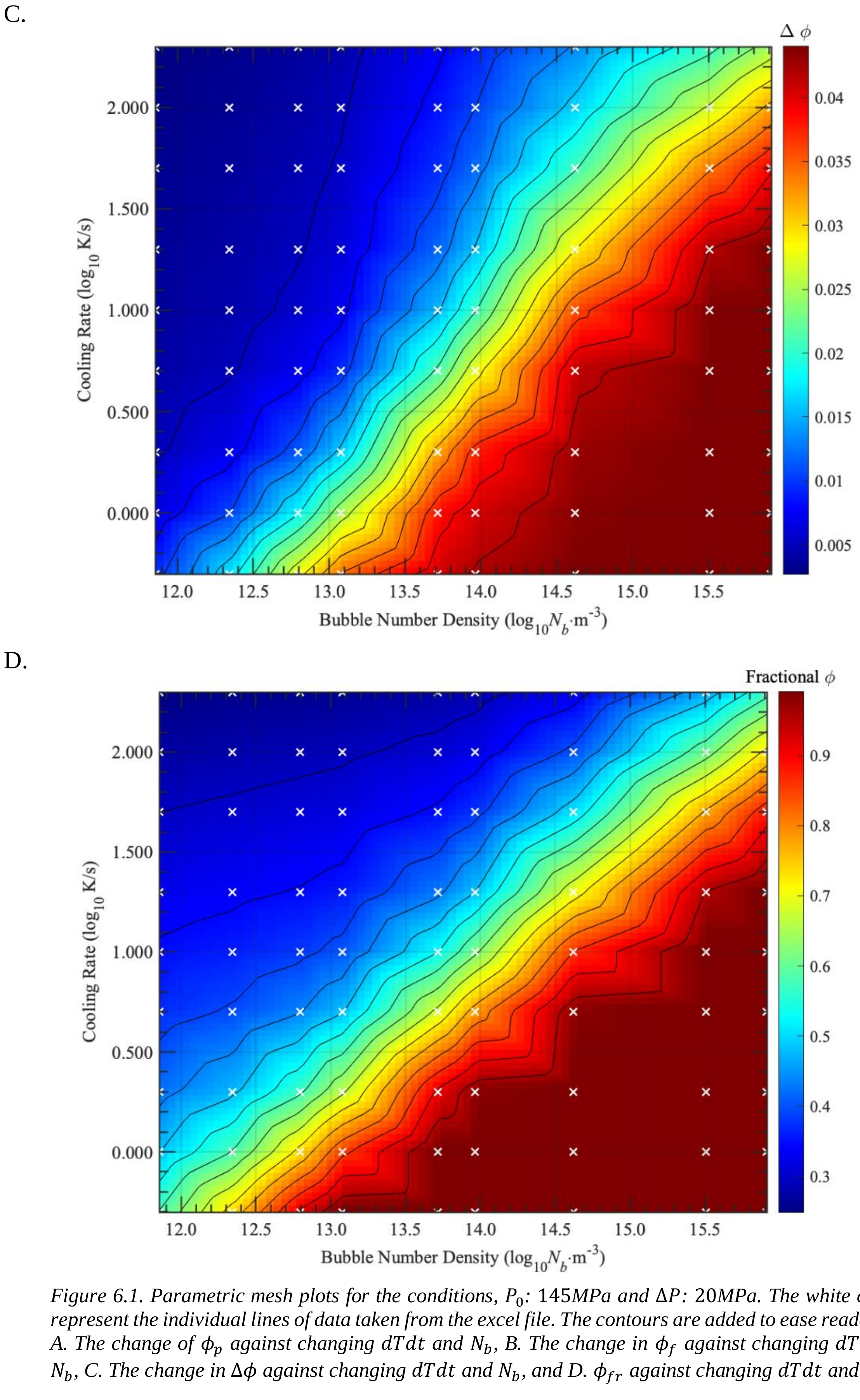

Figure 6.1. Parametric mesh plots for the conditions, P_0: $145MPa$ and ΔP: $20MPa$. The white crosses represent the individual lines of data taken from the excel file. The contours are added to ease readability. A. The change of ϕ_p against changing $dTdt$ and N_b, B. The change in ϕ_f against changing $dTdt$ and N_b, C. The change in $\Delta\phi$ against changing $dTdt$ and N_b, and D. ϕ_{fr} against changing $dTdt$ and N_b.

A.

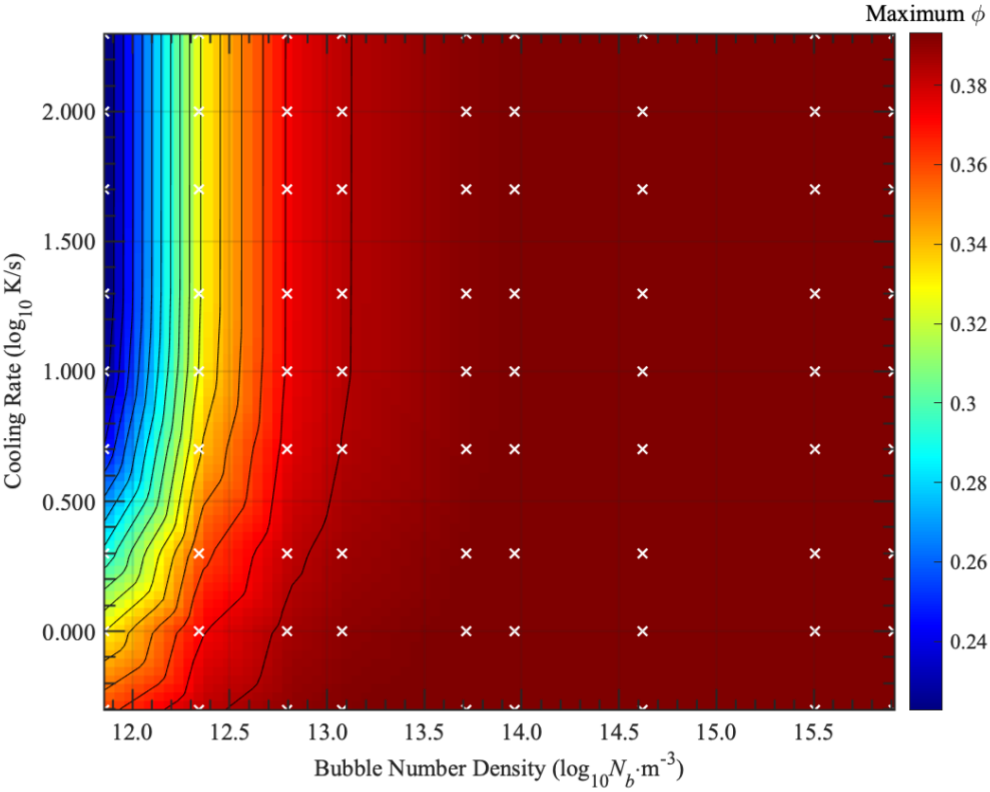
Maximum ϕ
0.38
0.36
0.34
0.32
0.3
0.28
0.26
0.24
2.000
1.500
1.000
0.500
0.000
Cooling Rate ($\log_{10}$ K/s)
12.0
12.5
13.0
13.5
14.0
14.5
15.0
15.5
Bubble Number Density ($\log_{10} N_b \cdot m^{-3}$)

B.

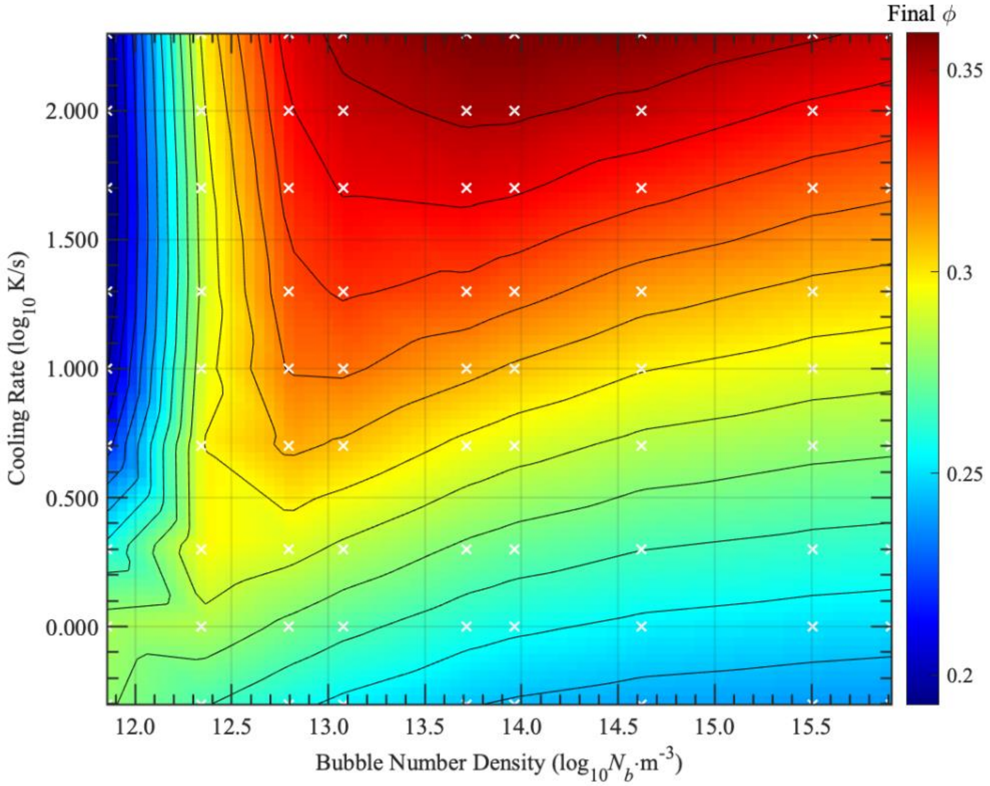
Final ϕ
0.35
0.3
0.25
0.2
2.000
1.500
1.000
0.500
0.000
Cooling Rate ($\log_{10}$ K/s)
12.0
12.5
13.0
13.5
14.0
14.5
15.0
15.5
Bubble Number Density ($\log_{10} N_b \cdot m^{-3}$)

C.

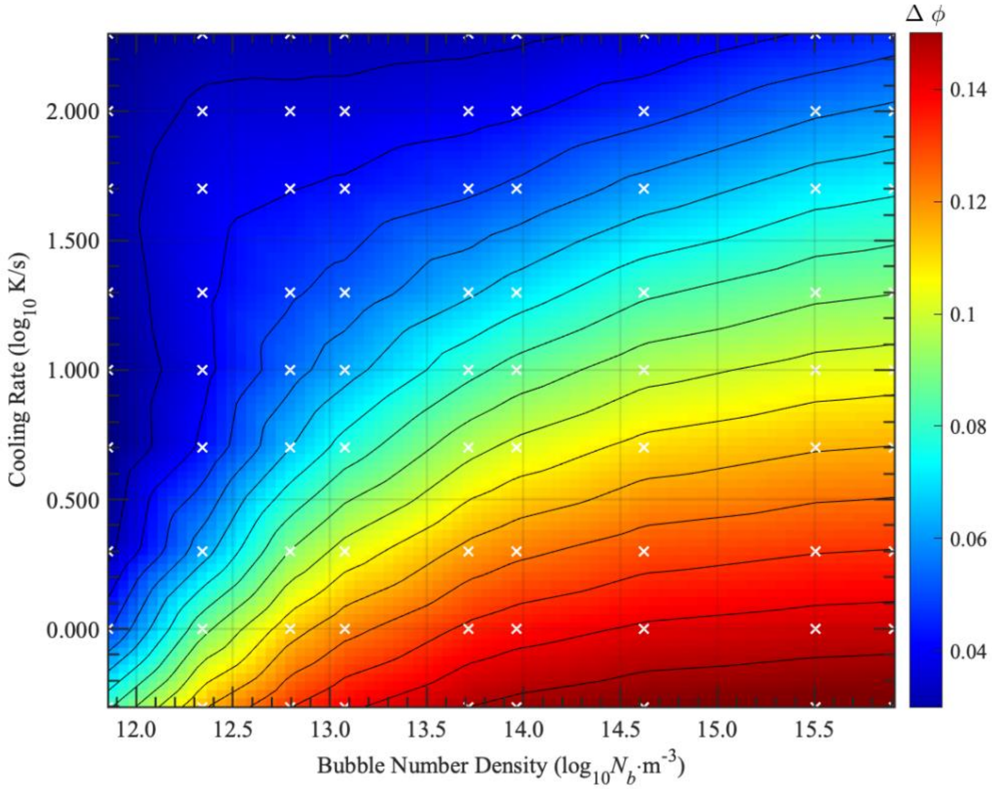

D.

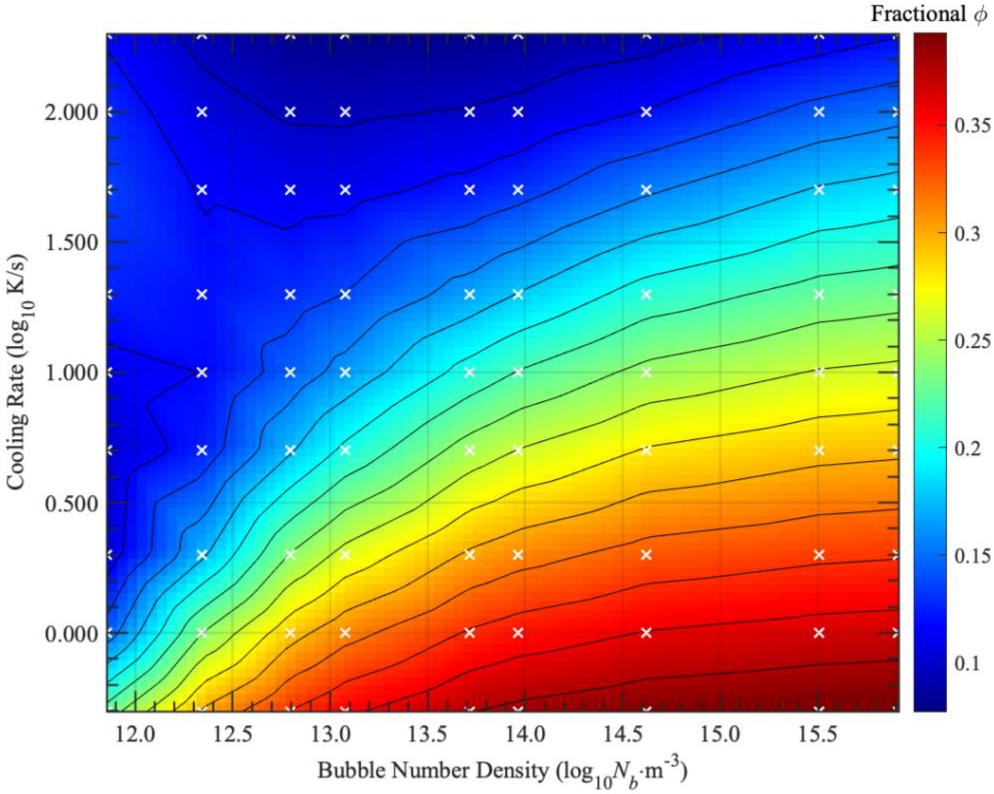

Figure 6.1. Parametric mesh plots for the conditions, P_0*:* $145MPa$ *and* ΔP*:* $100MPa$*. The white crosses represent the individual lines of data taken from the excel file. The contours are added to ease readability. A. The change of* ϕ_p *against changing* $dTdt$ *and* N_b*, B. The change in* ϕ_f *against changing* $dTdt$ *and* N_b*, C. The change in* $\Delta\phi$ *against changing* $dTdt$ *and* N_b*, and D.* ϕ_{fr} *against changing* $dTdt$ *and* $N_{b.}$

6.4 Discussion

6.4.1 Controlling N_b

Chapter 5 demonstrates the importance of N_b in influencing resorption levels. However, the N_b values used to construct figure 6.1 represent a range of potential N_b values rather than measured values. It can be determined that N_b does influence resorption levels (figure 6.1) so in an attempt to minimise resorption, can future decompression experiments control and maintain N_b values? The previous literature does not suggest that a way of controlling N_b levels has been used yet however, previous studies have shown a clear link between N_b and decompression rate (Toramaru, 2006; Hamada et al., 2009) and that it is possible to control decompression rate (Burgisser and Gardner, 2005). Toramaru, 2006 estimates the decompression rate by using N_b data from pumice samples, suggesting than an inverse of this solution would allow for a calculation of N_b based on decompression rates.

If N_b and cooling rate is controlled in future decompression experiments then the resorption levels of the samples can be calculated and any impact this may have on the studies outcome can be discussed in detail.

6.4.2 Application to Future Studies

The results from the parametric sweep provide useful information that is relevant to future studies that look at bubble growth and resorption.

Based on figures 6.1 and 6.2, it is recommended that to reduce the potential for resorption, a low N_b and a high $dTdt$ is used, however pressure conditions should also be considered. Based on figures 6.1A and 6.2A, it is difficult to minimise bubble growth unless a very low N_b is used paired with a high $dTdt$ however, depending on the experimental set up, bubble growth may want to be encouraged if it is the focus of the study (Blower et al., 2001; Blower et al., 2003; Massol and Koyaguchi, 2005). N_b is something which is often recorded post-experimentation (McIntosh et al., 2015), and it is suggested that samples that have a high N_b have undergone a large amount of resorption. This will need to be considered when concluding any studies on bubble growth.

6.4.3 Application to Different Composition

The results presented here are only applicable to studies which use rhyolitic samples, specifically the composition of the Panum Crater Dome (PCD), used by Burgisser and Gardner (2005). The PCD composition is also used by similar decompression studies (Mangan and Sisson, 2000; Watkins et al., 2017).

The use of different compositions results in different levels of bubble growth and resorption. This thesis uses data from decompression experiments on rhyolitic samples however is it possible to apply figure 6.1 to other similar compositions to produce reliable estimates of $\Delta\phi$? Compositions such as Vesuvius 79AD (VAD79), Italy, (a phonolitic white pumice), recorded by Iacono-Marziano et al., 2007, a rhyolitic obsidian from Krafla, Iceland, recorded by Tuffen and Castro, 2009, and a rhyolitic obsidian from Güney Dagi, Turkey recorded by Mourtada-Bonnefoi and Laporte, 2004 (table 6.2) are included in the numerical model.

Every decompression experiment mentioned above uses varying values for starting and ending pressures and temperatures as well as decompression and cooling rates. Every rock also has its own unique properties such as values for surface tension and density and requires different functions to be used for viscosity, solubility and diffusion. It is improbable that the mesh grids included in this thesis can be applied to other rhyolitic samples, let alone other compositions. A new numerical simulation needs to be run for every decompression study.

	VAD79	Krafla	Güney Dagi
SiO_2	57.15	75.17	76.51
TiO_2	0.30	0.22	0.03
Al_2O_3	21.34	12.02	12.56
FeO	2.70	3.13	0.70
MnO	0.14	0.11	0.07
MgO	0.39	0.09	0.01
CaO	3.26	1.66	0.25
Na_2O	5.16	4.58	4.47
K_2O	9.46	2.88	4.24
P_2O_5	0.09	0.0	0.0
Total	99.99	99.86	98.84

Table 6.2 The variability of rhyolitic compositions. Composition of Vesuvius (Iacono-Marziano et al., 2007), Krafla (Tuffen and Castro, 2009), and Güney Dagi (Mourtada-Bonnefoi and Laporte, 2004).

Allabar et al., 2020a reports that the VAD79 samples show a peak of 9wt% H_2O closest to the bubble wall (figure 6.3). This higher value for H_2Owt.% could be because of the different compositions and/or the experimental conditions. Allabar et al., 2020a use a series of decompression experiments (Allabar and Nowak, 2018; Allabar et al., 2020b) to quantify vesicle shrinkage. Initial temperatures (T_i) begin at $1050 - 1100$K, the initial pressure (P_0) used in 200MPa and follows a decompression rate ($dPdt$) of $0.064 - 1.7$MPas^{-1} before quenching at a rate of 150Ks^{-1} to a final pressure (P_f) of $110 - 20$MPa. With a higher pressure and higher decompression rate than the conditions used by Burgisser and Gardner (2005), this may result in different ϕ values even if the same composition has been used.

Figure 6.3 shows a H_2O profile from position A to B between two bubbles below the surface of an experimental sample. Errors are also included. The lower profile in the figure is a schematic illustration of the AB intersection of the sample below the surface. The resorption halo depicted around the bubbles has been calculated based on Raman Microscopy (RMS) measurements.

These high levels of resorption are just another example of why the numerical model used in this study is so important and should be applied to all decompression studies moving forward. Although the Allabar et al., 2020a method is suitable for measuring and calculating the H_2O content it is more time consuming than referring to a look-up table which could be generated based on the VAD79 composition using this studies' numerical method.

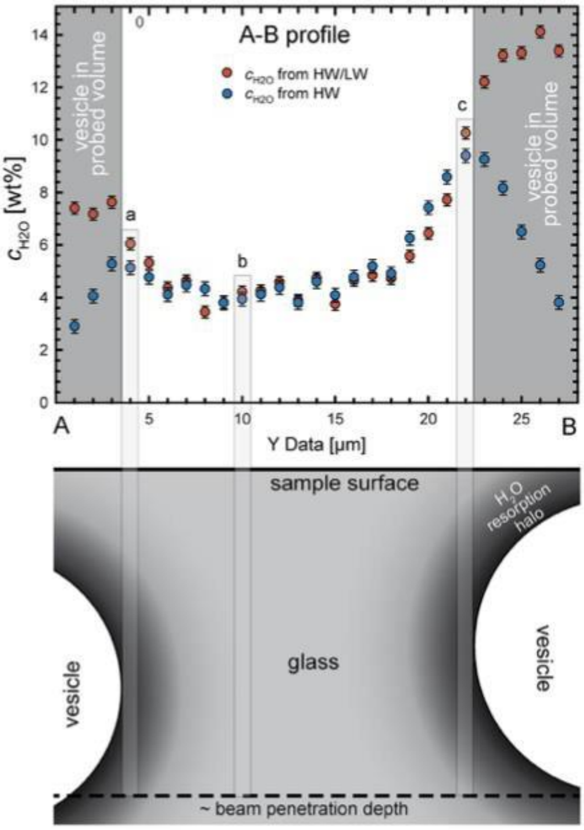

Figure 6.3 H_2O data from two bubbles as reported by Allabar et al., 2020a. Measured with RMS. The lower figure is a schematic illustration of the AB intersection of the sample below the surface.

6.4.4 Application to Natural Samples

When considering bubble growth and resorption is nature, other difficult to determine factors may need to be considered. It is difficult to accurately represent the conditions found in the volcanic environment however this studies' model could bring the natural environment into a realm which is more closely understood. A variety of previous natural samples are applied to figure 6.1C (figure 6.4), these previous studies all have a rhyolitic composition and provide data on N_b and/or $dTdt$ so it can be loosely understood how much resorption may have occurred within the natural environment.

Mitchel (2018) looks at submarine volcanism in relation to the Havre volcano with the cooling rate of the volcanic activity being linked to the vapor-rich submarine plume or hot seawater sheath (Mitchel et al., 2018). 2D image analyses is used to measure the vesicle characteristics, including N_b. Mitchel, 2018 references a $dTdt$ of $\gg 0.16$Ks^{-1} for large clasts that are erupted at Havre and have encountered water (Allen and McPhie, 2009; Fauria and Manga, 2018) suggested that resorption of anywhere < 0.16 could have occurred during the Havre eruption. Similar studies that utilise the natural environment are also recorded in figure 6.4 with a prediction of how much resorption may have occurred, indicated.

Kaminski and Jaupart, 1997 study the generation of pumice in Plinian eruptions and design a physical model to describe the behaviour of gas bubbles ascending a volcanic conduit. It is concluded that based on the physical model and observations pumice vesicularity increases as magma viscosity decreases. For the model calculations, Kaminski and Jaupart, 1997 reference a $dTdt$ of 20Ks^{-1}. Depending on the values chosen for the N_b, which isn't specified, the bubbles could be experiencing anywhere between $0.04 - 0.11$ resorption.

Gardner et al., 2018 study the sintering of rhyolitic ash under shallow conduit conditions. The evolution of samples is studied following isothermal and isobaric experiments with all samples appearing to follow four textural phases. Textures are found to evolve faster at higher temperatures and higher pressures. A $dTdt$ of 10Ks^{-1} is used for a range of N_b values from $4.89 \times 10^6 - 4.89 \times 10^{12}$m^{-3}. Depending on the experiment, a small amount of resorption will have occurred.

Gottsmann and Dingwell, 2001 quantify the cooling history across the glass transition of flow ramps at the front of the rhyolitic Rocche Ross flow of Lipari Aeolian Islands. Samples are studied and the chemical compositions measured using microprobe techniques while water contents are determined using Fourier-Transform Infra-Red (FTIR). However, the samples studied, based on the cooling rate provided, which is out of range of figure 6.4, will have undergone high levels of resorption which should be considered when making any concluding statements.

Giachetti et al., 2010 studies the volcanic activity displayed by the Soufrière Hills volcano in 1997. The vesicles contained within frothy pumices, breadcrust bombs and dense pumices are used to understand how and when bubble nucleation took place. Giachetti et al., 2010 reference a N_b value of 29×10^{14}m^{-3}. These pumice samples have undergone either very little or a substantial amount of resorption and taking this into account may aid the understanding of the bubble nucleation processes during the 1997 Soufrière Hills eruption even more.

Another rhyolitic eruption is studied by Houghton et al., 2010. The 1.8ka Taupo eruption generated seven eruptive units which are examined using SEM images and by calculating the vesicle number densities, the rate of magma ascent can be determined. The Vesicle Number Density (VND) is provided for each of the seven units and it should be assumed that each unit experienced some form of resorption. For instance, unit 1 has a VND of 6.89×10^{14}m^{-3} so it can be concluded that this unit experienced resorption ranging from $0.03 - 0.15$. In this study high number densities are used to reflect a second late-stage, disequilibrium nucleation event in the shallow conduit (Mourtada-Bonnefoi and Mader, 2004; Cluzel et al., 2008). However due to resorption, the VND's recorded may not be an accurate representation.

In Hamada et al., 2010 decompression experiments are carried out on a rhyolitic liquid to characterise effects of magma ascent rate and temperature on bubble nucleation kinetics on N_b. The experimental results are used to support the theory that N_b is a good marker of the decompression rate of magma in volcanic conduits, regardless of temperature. The N_b Hamada et al., 2010 work with is 4.6×10^{13}m^{-3} which can result in a range of resorption outcomes.

It is important that for future studies N_b and $dTdt$ are well documented to allow for bubble growth and resorption to be monitored.

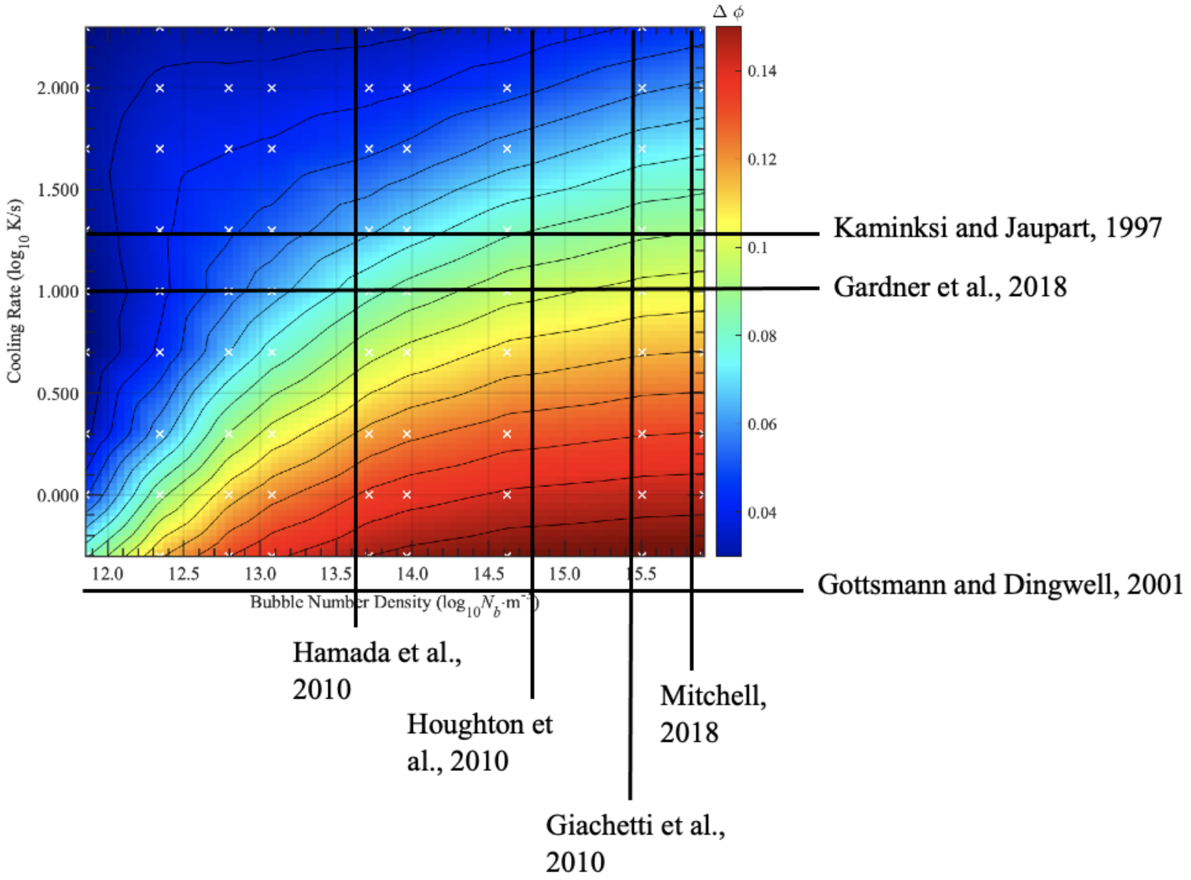

Figure 6.4 Data collected from various natural and experimental environments. The horizontal and vertical lines are based on conditions provided by the studies and are used to provide an estimate of how much resorption may occur. The studies in a clockwise direction are Kaminski and Jaupart, 1997: a study of expansion and quenching of vesicular fragments in Plinian eruptions, giving a cooling rate of between $2-20Ks^{-1}$*, in this plot the highest cooling rate is included. Gottsmann and Dingwell, 2001: looking at quenching of a rhyolitic flow from the Rocche Rosse flow of Lipari, Aeolian Islands, Italy. Gardner et al., 2018: the sintering of ash is examined under various conditions to look at mitigating explosivity. Hamada et al., 2010: rhyolitic pumices are studied using decompression experiments which generate samples comparable to those in natural silicic pumices from Plinian eruptions. Houghton et al., 2010: Samples from the 1.8ka Taupo eruption are examined. Giachetti et al., 2010: looking at syn-explosive vesiculation in pumices from La Soufrière, Montserrat.*

By minimising the effects of resorption, future studies can make more accurate conclusions based on bubble textures knowing that they have not been over-printed post-decompression by the resorption process or they can estimate how much overprinted has occurred. This will lead to more accurate findings on understanding how the volcanic conduit works and the study of bubbles as they travel towards the surface.

6.5 Conclusion

A parametric sweep is carried out for the rhyolite samples used by Burgisser and Gardner (2005). A range of values for N_b, $dTdt$, P_i and ΔP are used to generate 6561 bubble growth and resorption values.

The values for the influencing factors are chosen based on commonly used values found in experimental studies as well as values which exist in the natural world. A parametric sweep is programmed into the numerical model by running a MATLAB `combvec loop` through all possible outcomes before saving the complete output into an excel file. Mesh grids are used to plot the parametric outputs, allowing analysis of multiple variables simultaneously. Changing resorption levels are looked at based on N_b and $dTdt$ whilst also considering two separate pressure scenarios.

For future studies, to minimise the process of resorption happening it is suggested that higher pressure values be used as well as a high $dTdt$. If the post-experimental samples have a low N_b, it is suggested that resorption is likely to have happened to some extent. These results, however, are only applicable to specific compositions and the parametric sweep needs to be repeated for other compositions and experimental set ups.

7. Conclusion

7.1 Further Work

Further research into resorption for different compositions needs to be carried out with the aim of creating a full dataset applicable to a variety of experimental samples e.g., Vesuvius AD79 white pumice (Iacono-Marziano et al., 2007; Marxer et al., 2015; Allabar and Nowak, 2018; Allabar et al., 2020a), Chaitén rhyolite (Castro and Dingwell, 2009; Browning et al., 2020), Little Glass Butte obsidian (Kaminski and Jaupart, 1997; Gardner et al., 1999), and Krafla rhyolite (Tuffen and Castro, 2009). These same compositions are often used in decompression studies because of how accessible and homogeneous the samples are (Iacono-Marziano et al., 2007), as well as how much water is present in the samples (Castro and Dingwell, 2009).

Once there is an improved understanding of how bubble growth and resorption works for different compositions and experimental scenarios, further study can take place, looking at how much cooling rate ($dTdt$) and bubble number density (N_b) influence bubble growth and resorption and how important these factors are in considering decompression experiments.

It is a suggestion that in the future, full experimental guidance is published on the best experimental conditions to use to minimise bubble resorption as well as conditions to avoid. This should be paired with how much resorption can influence any desired results and how to correctly take resorption results into account.

An important aim of experimental volcanology is to be able to apply experimental findings to the natural world; a better understanding of how resorption occurs in the laboratory will translate into a better understanding of the process of resorption in the volcanic conduit and how this may present itself in volcanic samples.

The parametric sweep presented in chapter 6 opens itself up to further study. For each mesh plot in figures 6.1 and 6.2, two out of the four influencing factors listed ($N_b, dTdt,$ final pressure (P_f), and pressure change (ΔP)) are looked at, however it would be interesting to look at three or four of these factors in one plot by parameterising all four factors. This would be possible by turning N_b and $dTdt$ into a single non-dimensional number. This value would be based on diffusion, as $dTdt$ controlled the diffusion timescale while N_b sets the diffusion length scale, allowing these two factors to combine. This would allow these four influencing factors to be analysed simultaneously to improve resorption prediction. It is recommended that this is the next step for resorption analysis.

As this current study stands, the model presented is confined to a theoretical exercise. However, it has the potential to be applied and used widely in volcanological studies. For this to happen, further work needs to be undertaken to improve and legitimise the numerical model, this includes applying it to more decompression experiments to examine and compare results.

To apply this model to natural scenarios would be incredibly beneficial however with the current knowledge, it is difficult to constrain eruption environments so although the numerical model can be used to make estimates of resorption potential, any conclusions should be backed up by other evidence such as the textural images produced by Houghton et al. (2010), Pappalardo et al. (2018), Carey et al. (2013), and McIntosh et al. (2014) or geochemical data (McIntosh et al. 2014; Allabar et al., 2020b).

7.2 Summary of Study

Bubble growth and resorption are what drive volcanic eruptions, and they play a major role in determining eruption style. This study aims to understand how resorption can be influenced and how it may alter bubble textures and final experimental results.

A numerical model, initially developed by Coumans et al. (2020) is used to run simulations of bubble growth and resorption using experimental data from Burgisser and Gardner (2005), a study which made conclusions on volcanic processes based on final bubble textures of its samples. The Coumans et al. (2020) numerical model undergoes further model development to account for equilibrium bubble conditions and to define a more accurate cooling pathway.

The background behind the Coumans et al. (2020) model is explored and the components that are used for the composition, solubility, diffusivity, viscosity, and Equation of State (EOS) functions are explored. The basics of the model are also explored, including the models of Proussevitch and Sahagian (1998) and Blower (2001) which form the building blocks of the current model.

Three successive research chapters explore the questions raised in the introduction and background research: how important resorption is, the process of resorption following quench and how resorption can be minimised in decompression experiments.

The process of resorption is understood to a greater level of detail based on the numerical model results of the five samples from Burgisser and Gardner (2005). Burgisser and Gardner (2005) state that ABG1 is held at equilibrium and does not undergo any bubble growth or resorption, however, the numerical model concludes that resorption occurs during the quench. When looking at the four ABG samples that experience the second decompression stage, it is clear that the samples undergo significant amounts of resorption which have the potential to alter syn-experimental textures.

Four influencing factors - N_b, $dTdt$, P_f, ΔP – are named as having the most influence on how much resorption occurs. A parametric sweep is used to make conclusions on the best experimental practises to minimise the amount of resorption that occurs during the quenching process. The results gathered from the parametric sweep can allow for the effect of resorption to be removed from both experimental and natural samples, supporting more meaningful interpretations of bubble textures.

From this study, several conclusions can be drawn:

1) The Burgisser and Gardner (2005) study looks at samples which experience various levels of resorption, with the sample at equilibrium experiencing no resorption.
2) A newton cooling curve is more accurate when determining how samples cool in the laboratory and in nature.
3) Cooling rate influences how much resorption occurs, to varying degrees, with the lowest cooling rates causing more bubble growth and more resorption.
4) In comparison to the conclusions by McIntosh et al. (2014) which uses Secondary Ion Micro-Spectrometry (SIMS) to calculate resorption, similar levels of resorption are reported by this numerical model. The disparities between these sets of values are suggested to be because of experimental errors.
5) Both N_b and P_f affect how much resorption occurs, with low- and high-pressure minimising resorption, while peak resorption occurs at a P_f of 50MPa. For N_b, resorption increases with an increasing N_b.

6) A parametric sweep is carried out. A high N_b, low $dTdt$, and high initial pressure (P_i) and P_f, resorption is minimised. It is suggested that these influencing factors should be controlled in future studies to minimise how much over-printing occurs to bubble textures.

7.3 Implications in the Field of Experimental Volcanology

This study can have far-reaching implications in terms of experimental and natural analysis of volcanic samples. The full numerical model script is provided as supplementary material and should be used for further research into what controls resorption and how it affects final bubble textures.

The numerical model developed in this thesis should be used in all future decompression studies to factor in resorption and the impact it may have. This should be done by monitoring the N_b, cooling rate, decompression rate, starting and ending pressure and temperature for each study. It is also suggested that the surface tension and density of the experimental samples be measured to provide accurate compositional conditions.

For natural scenarios, it is difficult to control the above factors so caution should be taken when applying the numerical model to natural scenarios. It is suggested that for this model to be applicable to natural studies, further study needs to be done on the cooling pathways of individual natural scenarios as well as how to accurately use vesicle number density (VSD) as a replacement for N_b. Houghton et al. (2010) use binary images of pumices (see section 2.2.4) to investigate the textures of the samples in terms of vesicle distribution, size, shape, and elongation. The images (figure 2.4) show a complex architecture of vesicles and it is not possible at this stage to apply the numerical model to this data other than to make resorption estimates based on inferred eruption conditions. Similarly, the microstructures presented by Pappalardo et al. (2018) show a high degree of vesiculation and while these textures reveal details about the bubble behaviour, it is not constrained enough to calculate the likelihood of resorption. However, experimental studies similar to McIntosh et al. (2014) such as Watkins et al. (2012) which look at experimental scenarios and use these results to extrapolate out to also consider resorption in natural scenarios are beneficial to investigate.

The over-arching aim of this study and studies like it, should be to create a fully open-source database to allow researchers to carry out accurate decompression studies where it is known exactly what is happening to the bubbles in the samples. This will benefit the understanding of the role bubbles play in volcanic conduits and create a more concrete understanding of past volcanic eruptions.

8. Appendices

8.1 Newton Cooling Script

To select a cooling pathway for the numerical model, the user must select which `case` to use. ‘P: Isobaric, T: Isothermal’ refers to a constant pressure and constant temperature. ‘P: Isobaric, T: Polythermal-Dwell’ refers to a constant pressure and decrease in temperature. ‘P: Polybaric-Dwell, T: Isothermal-quench’ refers to a decreasing pressure and decreasing temperature. ‘P: Polybaric-Dwell, T: Isothermal-quench-N’ refers to a decreasing pressure and a decreasing temperature following a newton cooling pathway. This is written as:

```
%P-T-t profile
%PTtModel = ‘P: Isobaric, T: Isothermal’;
%PTtModel = ‘P: Isobaric, T: Polythermal-Dwell’;
%PTtModel = ‘P: Polybaric-Dwell, T: Isothermal-quench’;
PTtModel = ‘P: Polybaric-Dwell, T: Isothermal-quench-N’;
```

With % representing comments which do not influence the script and are usually intended for the benefit of the user. The last option listed represents the newton cooling pathway, a pathway which has to be incorporated into the model.

A new `case` is set up in the `switch PTt model`. This case contains the required parameters to calculate the newton cooling pathway: initial temperature (`T_0`), final temperature (`T_f`), ambient temperature (`T_a`), newton cooling constant (`k_cool_Newton`), initial pressure (`P_0`), final pressure (`P_f`), decompression rate (`dPdt`) and initial water concentration (`H2Ot_0`). To calculate the time of quench (`t_f`), equations (11) and (36) are used:

```
t_f = abs((P_f – P_0)/dPdt) + (log((T_f – T_a)./(T_0 –
T_a))./k_cool_Newton);
```

To calculate the decompression rate, the ambient temperature needs to be passed in place of final temperature and for the cooling rate (`dTdt`), the newton cooling constant needs to be passed in place of the cooling rate:

```
T_f = T_a;
dTdt = k_cool_Newton;
```

This ‘hacking’ of the arguments list is then reversed once the newton cooling function is at work:

```
T_a = T_f;
k_cool_Newton = dTdt;
```

In the newton cooling function, the time at which the experiment reaches the final pressure is calculated before calculating the pressure and temperature conditions throughout the experimental run:

```
P_t_Press = abs((P_f – P_0)/dPdt;
%if t <= P_t_Press, the value of ‘1’ will be returned and if it is not
the case then the value of ‘0’ will be returned
P = ((t <= P_t_Press).*(P_0 + t.*dPdt) + ((t > P_t_Press).*P_f);
```

```
%if t <= P_t_Press then this means the experiment is still undergoing
decompression so just T_0 is required however if the time is greater
than the decompression time then the temperature is calculating
according to the newton cooling rate
T = ((t <= P_t_Press).*T_0) + (((t > P_t_Press).*(T_a + T_0 –
T_a).*exp(k_cool_Newton.*(t-P_t_Press)));
```

These statements are what calculate the newton pathway, depending on the pressure and temperature conditions which are input. Non-newton cooling pathways are calculated in a similar manner.

8.2 Equilibrium Conditions Script

When solving equation (34) numerically, equation (32) acts as V_{g1} and equation (34) acts as V_{g2}. Both these equations feature the radius of the bubble, however V_{g1} features it explicitly while V_{g2} features it implicitly. To calculate the radius in MATLAB, the equations need to be equal. The function `fzero` is used where:

```
x = fzero(fun, x0);
```

The function finds point x where $fun(x) = 0$ and will be able to find the initial bubble radius where $V_{g1} - V_{g2} = 0$. The equilibrium bubble calculations are kept within a single function which stores the necessary variables for the calculations: initial temperature, final temperature, initial pressure, final pressure, bubble number density (`Nb`), melt density (`melt_Rho`), surface tension (`SurfTens`) and the solubility function (`SolFun`), and is written as:

```
function [phi, bub_rad] = GetEqmBub(T_0, T_f, P_0, P_f, Nb, SurfTens,
melt_Rho, SolFun);
```

To calculate the initial bubble radius (`bub_rad`), the `fzero` function is incorporated into the script and written as:

```
bub_rad = fzero(@find_vol, r_0, [], R, T_0, T_f, P_0, P_f, V_m, W,
SurfTens, melt_Rho, SolFun);
```

`r_0` is an initial estimate of the bubble radius (here it is 10^{-5}m), `R` is the universal gas constant, `V_m` is the volume of the melt, and `W` is the molecular mass of gas. The `fzero` function is used to calculate the bubble radius when `find_vol = 0`, `find_vol` is stored within the function:

```
function vol_diff = find_vol(r, R, T_0, T_f, P_0, P_f, V_m, W, SurfTens,
melt_Rho, SolFun);
```

The `vol_diff` is $V_{g1} - V_{g2}$ and when `vol_diff` is equal to zero, it is passed through to the `fzero` function. Once an initial radius has been calculated, the initial water concentration is calculated by selecting the appropriate solubility model function:

```
Ib_H2O_0 = SolFun(Ib_Tf, Ib_Pf + ((2*SurfTens)/R_0)));
```

`SolFun` is a function which contains the various solubility models and can change depending on the solubility model selected by the user.

8.3 Parametric Sweep

The first stage in creating a parametric sweep is to create a matrix which contains all possible combinations of the input vectors: bubble number density (`BND`), initial pressure (`P0`), pressure change (`P_delta`) and newton constant (`newton_c`). This is written as:

```
A = combvec = (BND, P0, P_delta, newton_c);
%Calculate the number of combinations
[Comb,~] = size(A);
%Create a series of ones for each parameter so that the number of
values for each parameter is known
peak_phi_vector = ones(Comb, 1);
R_0 = ones(Comb, 1);
Phi_0 = ones(Comb, 1);
Ib_H2O_0 = ones(Comb, 1);
final_phi_vector = ones(Comb, 1);
```

The output folder is stated and then a `for loop` runs through all combinations of `A`.

```
for i = 1:1:Comb
%Pull out the input variables from the parameter combination matrix
     input_BND = A(i, 1);
     input_P0 = A(i, 2);
     input_P_delta = A(i, 3);
     input_newton_c = A(i, 4);
```

The excel folder is output each time a new combination is run, creating 6561 excel files, before concatenating all files into one master file at the end of the run.

9. References

Allabar, A., Dobson, K.J., Bauer, C.C., Nowak, M., 2020a. Vesicle shrinkage in hydrous phonolitic melt during cooling. *Contrib. Mineral. Petrol.,* 175(21). [doi: 10.1007/s00410-020-1658-3].

Allabar, A., Nowak, M., 2018. Message in a bottle: Spontaneous phase separation of hydrous Vesuvius melt even at low decompression rates. *Earth. Planet. Sci. Lett.,* 501, pp192-201. [doi: 10.1016/j.epsl.2018.08.047].

Allabar, A., Sallis Gross, E., Nowak, M., 2020b. The effect of initial H2O concentration of decompression-induced phase separation and degassing of hydrous phonolitic melt. *Contrib. Mineral. Petrol.* 175(22). [doi: 10.1007/s00410-020-1659-2].

Allen, S.R., McPhie, J., 2009. Products of neptunian eruptions. *Geology,* 37(7), pp639-642. [doi: 10.1130/G30007A.1].

Badin, G., Crisciani, F., 2018. Variational Formulation of Fluid and Geophysical Fluid Dynamics - Mechanics, Symmetries and Conservation Laws. *Springer.* pp 218. [doi:10.1007/978-3-319-59695-2]. [ISBN 978-3-319-59694-5].

Balmforth, N.J., Craster, R.V., 2000. Dynamics of cooling domes of viscoplastic fluids. *J. Fluid. Mech.,* 422, pp225 – 248. [doi: 10.1017/S002211200000166X].

Bennett, F.D., 1974. On volcanic ash formation. *Am. J. Sci.,* 274, pp644 - 661. [doi: 10.2475/ajs.274.6.648].

Berndt, J., Liebske, C., Holtz, F., Freise, M., Nowak, M., Ziegenbein, D., Hurkuck, W., Koepke, J., 2002. A combined rapid-quench and H2-membrane setup for internally heated pressure vessels: Description and application for water solubility in basaltic melts. *Am Mineral.* 87, pp1717–1726. [doi: 10.2138/am-2002-11-1222].

Blank, J.G., Stolper, E.M., Carroll, M.R., 1993. Solubilitie of carbon dioxide and water in rhyolitic melt at 850C and 750bars. *Earth. Planet. Sci. Lett.,* 119(1-2), pp27-36. [doi: 10.1016/0012-821X(93)90004-S].

Blower, J., 2001. Factors controlling permeability-porosity relationships in magma. *Bull. Volcanol.,* 63, pp497-504.

Blower, J.D., 2001. 'Degassing processes in volcanic eruptions', PhD Thesis, University of Bristol.

Blower, J.D., Keating, J.P., Mader, H.M., Phillips, J.C., 2001a. Inferring volcanic degassing processes from vesicle size distributions. *Geophys. Res. Lett.,* 28(2), pp347-350. [doi: 10.1029/2000GL012188].

Blower, J.D., Mader, H.M., Wilson, S.D.R., 2001b. Coupling of viscous and diffusive controls on bubble growth during explosive volcanic eruptions, *Earth Planet. Sci. Lett.,* 193(1-2), 47-56. [doi: 10.1016/S0012-821X(01)00488-5].

Blower, J.D., Keating, J.P., Mader, H.M., Philips, J.C., 2003. The evolution of bubble size distributions in volcanic eruptions. *J. Volcanol. Geotherm. Res.,* 120(1-2), pp1-23. [doi: 10.1016/S0377-0273(02)00404-3].

Browning, J., Tuffen, H., James, M.R., Owen, J., Castro, J.M., Halliwell, S., Wehbe, K., 2020. Post-fragmentation vesiculation timescales in hydrous rhyolitic bombs from Chaitén volcano. *J. South. American. Earth. Sci.,* 104, 102807. [doi: 10.1016/j.jsames.2020.102807].

Brugger, C.R., Hammer, J.E., 2010. Crystallization Kinetics in Continuous Decompression Experiments: Implications for Interpreting Natural Magma Ascent Processes. *J. Petrol.,* 51(9), pp1941-1965. [doi: 10.1093/petrology/egq044].

Buono, G., Fanara, S., Macedonio, G., Palladino, D.M., Pestrosino, P., Sottili, G., Lucia, P., 2020. Dynamics of degassing in evolved alkaline magmas: Petrological, experimental and theoretical insights. *Earth Sci. Rev.*, 211, 103402. [doi: 10.1016/j.earscirev.2020.103402].

Burgisser, A., Gardner, J.E., 2005. Experimental constraints on degassing and permeability in volcanic conduit flow. *Bull. Volcanol.*, 67, pp42-56. [doi: 10.1007/s00445-004-0359-5].

Carey, R.J., Manga, M., Degruyter, W., Gonnermann, H., Swanson, D., Houghton, B., Orr, T., Patrick, M, 2013. Convection in a volcanic conduit recorded by bubbles. *Geology*, 41(4), pp.395-398. [doi: 10.1130/G33685.1].

Caricchi, L., Pommier, A., Pistone, M., Castro, J., Burgisser, A., Perugini, D., 2011. Strain-induced magma degassing: insights from simple-shear experiments on bubble bearing melts. *Bull. Volcanol.*, 73, pp1245-1257. [doi: 10.1007/s00445-011-0471-2].

Carroll, M.R., Blank, J.G., 1997. The solubility of H_2O in phonolitic melts. *American Mineral.*, 82(5-6), pp549-556. [doi: 10.2138/am-1997-5-615].

Cashman, K.V., 2004. Volatile controls on magma ascent and eruption. Sparks, R.S.J., Hawkesworth, C.J. (ed). The State of the Planet: Frontiers and Challenges in Geophysics, 150, Wiley & Blackwell. [doi: 10.1029/150GM10].

Cassidy, M., Castro, J.M., Helo, C., Troll, V.R., Deegan, F.M., Muir, D., Neave, D.A., Mueller, S.P., 2016. Volatile dilution during magma injections and implications for volcano explosivity. *Geology*. 44(12), pp1027–1030. [doi: 10.1130/G38411.1].

Castro, J.M., Dingwell, D.B., 2009. Rapid ascent of rhyolitic magma at Chaitén volcano, Chile. *Nature Lett.*, 461, pp780-783. [doi: 10.1038/nature08458].

Chaussard, E., 2016. Subsidence in the Parícutin lava field: Causes and implications for interpretation of deformation fields at volcanoes. *J. Volcanol. Geotherm. Res.* 320. [doi: 10.1016/j.volgeores.2016.04.009].

Chouet, B., Dawson, P., Nakano, M., 2006. Dynamics of diffusive bubble growth and pressure recovery in a bubbly rhyolitic melt embedded in an elastic solid. *J. Geophys. Res.*, 111, B07310. [doi:10.1029/2005JB004174].

Cluzel, N., Laporte, D., Provost, A., 2008. Kinetics of heterogenous bubble nucleation in rhyolitic melts: implications for the number density of bubbles in volcanic conduits and for pumice textures. *Contrib. Mineral. Petrol.*, 156, pp745-763. [doi: 10.1007/s00410-008-0313-1].

Corsaro, R.A., Pompillo, M., 2004. Buoyancy-controlled eruption of magmas at Mt Etna, *Terra Nova*, 16, pp16-22. [doi: 10.1046/j.1365-3121.2003.00520.x].

Coumans, J.P., Llewellin, E.W., Wadsworth, F.B., Humphreys, M.C.S., Mathias, S.A., Yelverton, B.M., Gardner, J.E., 2020. An experimentally validated numerical model for bubble growth in magma. *J. Volcanol. Geotherm. Res.*, 402, 107002. [doi: 10.1016/j.jvolgeores.2020.107002].

Degruyter, W., Bachmann, O., Burgisser, A. & Manga, M., 2012. The effects of outgassing on the transition between effusive and explosive silicic eruptions. *Earth Planet. Sci. Lett.*, 349–350, pp161–170. [doi: 10.1016/j.epsl.2012.06.056].

Deschamps, A., Grigne, C., Le Saout, M., Soule, S.A., Allemand, P., Lanoe, B.V.V., Floc'h, F., 2014. Morphology and dynamics of inflated subaqueous basaltic lava flows. *Geochem. Geophys. Geosyst.*, 15, pp2128 – 2150. [doi: 10.1002/2014GC005274].

Di Genova, D., Kolzenburg, S., Wiesmaier, S., Dallanave, E., Nueville, D.R., Hess, K.U., Dingwell, D.B., 2017. A compositional tipping point governing the mobilization and eruption style of rhyolitic magma. *Nature*, 552, pp235–238. [doi: 10.1038/nature24488].

Dixon, J.E., Stolper, E.M., Holloway, J.R., 1995. An experimental study of water and carbon dioxide solubilities in mid-ocean ridge basaltic liquids. Part I: calibration and solubility models. *J. Petrol.*, 36, pp1607-1631.

Duan, Z., Zhang, Z., 2006. Equation of state of the H2O, CO2, and H2O-CO2 systems up to 10 GPa and 2573.15K: Molecular dynamics simulations with ab initio potential surface. *Geochim. Cosmo. Acta.,* 70(9), pp2311-2324. [doi: 10.1016/j.gca.2006.02.009].

Eichelberger, J.C., Carrigan, C.R., Westrich, H.R., Price, R.H., 1986. Non- explosive silicic volcanism. *Nature,* 323, pp598–602. [doi: 10.1038/323598a0].

Fauria, K.F., Manga, M., 2018. Pyroclast cooling and saturation in water, *J. Volcanol. Geotherm. Res.,* 352, pp17-31. [doi: 10.1016/j.jvolgeores.2018.07.002].

Fulcher, G.S., 1925. Analysis of recent measurements of the viscosity of glasses. *J. Am. Ceram. Soc.,* 8, pp339–355.

Gardner, J. E., 2009. The impact of pre-existing gas on the ascent of explosively erupted magma. *Bull. Volcanol.,* 71, pp835–844. [doi: 10.1007/s00445-009-0276-8].

Gardner, J., 2007. Heterogeneous bubble nucleation in highly viscous silicate melts during instantaneous decompression from high pressure. *Chem. Geol.,* 236(1-2), pp1-12. [doi: 10.1016/j.chemgeo.2006.08.006].

Gardner, J.E., Hilton, M., Carroll, M.R., 1999. Experimental constraints on degassing of magma: isothermal bubble growth during continuous decompression from high pressure. *Earth. Planet. Sci. Let.,* 168(1-2), pp201-218. [doi: 10.1016/S0012-821X(99)00051-5].

Gardner, J.E., Wadsworth, F. B., Llewellin, E. W., Watkins, J.M., Coumans, J. P., 2018. Experimental sintering of ash at conduit conditions and implications for the longevity of tuffsites. *Bull. Volcanol.,* 80(3), pp23. [doi: 10.1007/s00445-018-1202-8].

Giachetti, T., Druitt, T.H., Burgisser, A., Arbaret, L., Galven, C., 2010. Bubble nucleation, growth and coalescence during the 1997 Vulcanian explosions of Soufriere Hills Volcano, Montserrat. *J. Volcanol. Geotherm. Res.,* 193(3), pp215-231. [doi: 10.1016/j.jvolgeores.2010.04.001].

Goanac'h, H.S., Lovejoy, J.S., Scherzter, D., 1996. A scaling growth model for bubbles in basaltic lava flows. *Earth. Planet. Sci. Lett.,* 139(3-4), pp395-409. [doi: 10.1016/0012-821X(96)00039-8].

Gonnermann, H., and Manga, M., 2003. Explosive volcanism may not be an inevitable consequence of magma fragmentation. *Nature,* 426, pp432–435, [doi: 10.1038/nature02138].

Gonnermann, H.M., 2015. Magma Fragmentation. *Annu. Rev. Earth. Planet. Sci.,* 43, pp431-458.

Gonnermann, H.M., Manga, M., 2007. The Fluid Mechanics Inside a Volcano. *Annu. Rev. Fluid. Mech.,* 39, pp321-56. [doi: 10.1146/annurev.fluid.39.050905.110207].

Gottsmann, J., Dingwell, D.B., 2001. The cooling of frontal flow ramps: a calorimetric study on the Rocche Rosse rhyolite flow, Lipari, Aeolian Islands, Italy. *Terra Nova,* 13, pp157-164. [doi: 10.1046/j.1365-3121.2001.00332.x].

Hajimirza, S., Gonnermann, H.M., Gardner, J.E., Giachetti, T., 2019. Predicting homogeneous bubble nucleation in rhyolite. *JGR Solid Earth,* 124(3), pp2395-2416. [doi: 10.1029/2018JB015891].

Hamada, M., Laporte, D., Cluzel, N., Koga, K.T., Kawamoto, T., 2010. Simulating bubble number density of rhyolitic pumices from Plinian eruptions: constraints from fast decompression experiments. *Bull. Volcanol.,* 72, pp735-746. [doi: 10.1007/s00445-010-0353-z].

Hammer, J.E. and Rutherford, M.J., 2002. An experimental study of the kinetics of decompression-induced crystallization in silicic melt. *J. Geophys. Res.,* 107 (81). [doi: 10.1029/2001JB000281].

Hansteen. T.H. and Klügel. A., 1998. Multi-stage magma ascent beneath the Canary Islands: evidence from fluid inclusions. *Contrib. Mineral. Petrol.*, 132, pp48-64.

Heap, M.J., Violay, M., Wadsworth, F.B., Vasseur, J., 2017. From rock to magma and back again: The evolution of temperature and deformation mechanism in conduit margin zones. *Earth. Planet. Sci. Lett.*, 463, pp92-100. [doi: 10.1016/j.epsl.2017.01.021].

Houghton, B.F., Carey, R.J., Cashman, K.V., Wilson, C.J.N., Hobden, B.J., Hammer, J.E., 2010. Diverse patterns of ascent, degassing, and eruption of rhyolite magma during the 1.8ka Taupo eruption, New Zealand: Evidence from clast vesicularity. *J. Volcanol. Geotherm. Res.*, 195(1), pp31-47. [doi: 10.1016/j.jvolgeores.2010.06.002].

Huppert, H.E., Sparks, R.S.J., Turner, J.S., Arndt, N.T., 1984. Emplacement and cooling of komatiite lavas. *Nature*, 309, pp19 – 22. [doi: 10.1038/309019a0].

Iacono-Marziano, G., Schmidt, B.C., Dolfi, D., 2007. Equilibrium and disequilibrium degassing of a phonolitic melt (Vesuvius AD 79 “white pumice”) simulated by decompression experiments. *J. Volcanol. Geotherm. Res.*, 161(3), pp151-164. [doi: 10.1016/j.jvolgeores.2006.12.001].

Jacobs, G.K., Kerrick, D.M., 1980. A simple rapid quench design for cold-seal pressure vessels. *American Min.*, 65, pp1053-1056.

Kaminski, E., Jaupart, C., 1997. Expansion and quenching of vesicular magma fragments in Plinian eruptions. *J. Geophys. Res. Solid Earth*, 102(B6), pp12187-12203. [doi: 10.1029/97JB00622].

Kilbride, B.M., Edmonds, M., Biggs, J., 2016. Observing eruptions of gas-rich compressible magmas from space. *Nature Comms.*, 7, 13744. [doi: 10.1038/ncomms13744].

Klug, C., Cashman, K.V., 1996. Permeability development in vesiculating magmas: implications for fragmentation. *Bull. Volcanol.*, 58, pp87-100. [doi: 10.1007/s004450050128].

Kolzenburg, S., Giordano, D., Cimarelli, C., Dingwell, D.B., 2016. In situ thermal characterization of cooling/crystallizing lavas during rheology measurements and implications for lava flow emplacement. *Geochima. Cosmo. Acta.*, 195, pp244 – 258. [doi: 10.1016/j.gca.2016.09.022].

Lamb, H., 1932. Hydrodynamics, 6th ed., Cambridge University Press, Cambridge.

Larsen, J.F. and Gardner, J.E., 2000. Experimental constraints on bubble interactions in rhyolite melts: implications for vesicle size distributions. *Earth. Planet. Sci. Let.*, 180(1-2), pp201-214. [doi: 10.1016/S0012-821X(00)00166-7].

Lavallee, Y., Dingwell, D.B., Johnson, J.B., Cimarelli, C., Hornby, A.J., Kendrick, J.E., von Aulock, F.W., Kennedy, B.M., Andrews, B.J., Wadsworth, F.B., Rhodes, E., Chigna, G., 2015. Thermal vesiculation during volcanic eruptions. *Nature*, 528, pp544-547. [doi: 10.1038/nature16153].

Lejeune, A.M., Trull, Y.B.T.W., Richet, P., 1999. Rheology of bubble-bearing magmas. *Earth. Planet. Sci. Lett.*, 166(1-2), pp71-84. [doi: 10.1016/S0012-821X(98)00278-7].

Lensky, N.G., Lyakhovsky, V., Navon, O., 2001. Radial variations of melt viscosity around growing bubbles and gas overpressure in vesiculating magmas. *Earth Planet. Sci. Lett.*, 186(1), pp1-6. [doi: 10.1016/S0012-821X(01)00227-8].

Lensky, N.G., Navon, O., Lyakhovsky, V., 2004. Bubble growth during decompression of magma: experimental and theoretical investigation. *J. Volcanol. Geotherm. Res.*, 129(1-3), pp7-22. [doi: 10.1016/S0377-0273(03)00229-4].

Liu, Y., Zhang, Y., Behrens, H., 2005. Solubility of H_2O in rhyolitic melts at low pressures and a new empirical model for mixed H_2O-CO_2 solubility in rhyolitic melts. *J. Volcanol. Geotherm. Res.*, 143(1-3), pp219-235. [doi: 10.1016/j.jvolgeores.2004.09.019].

Lesher, C.E., Spera, F.J., 2015. *The Encyclopaedia of Volcanoes*. 2nd Ed. Academic Press. Massachusetts.

Lyakhovsky, V., Hurwitz, S., Navon, O., 1996. Bubble growth in rhyolitic melts: experimental and numerical investigation. *Bull Volcanol.,* 58, pp19-32. [doi: 10.1007/s004450050122].

Manga, M., Castro, J., Cashman, K.V., Loewenberg, M., 1998. Rheology of bubble-bearing magmas. *J. Volcanol. Geotherm. Res.,* 87(1-4), pp15-28. [doi: 10.1016/S0377-0273(98)00091-2].

Mangan, M., Sisson, T., 2000. Delayed, disequilibrium degassing in rhyolitic magma: decompression experiments and implications for explosive volcanism. *Earth. Planet. Sci. Lett.,* 183(3-4), pp441-455. [doi: 10.1016/S0012-821X(00)00299-5].

Mangan, M.T., Cashman, K.V., 1996. The structure of basaltic scoria and reticulite and inferences for vesiculation, foam formation, and fragmentation in lava fountains. *J. Volcanol. Geotherm. Res.,* 73(1-2), pp1-18. [doi: 10.1016/0377-0273(96)00018-2].

Manley, C.R., 1992. Extended cooling and viscous flow of large, hot rhyolite lavas: implications of numerical modelling results. *J. Volcanol. Geotherm. Res.,* 53(1-4), pp27-46. [doi: 10.1016/0377-0273(92)90072-L].

Martel, C. and Iacono-Marziano, G., 2015. Timescales of bubble coalescence, outgassing, and foam collapse in decompressed rhyolitic melts. *Earth. Planet. Sci. Lett.,* 412, pp173-185. [doi: 10.1016/jepsl.2014.12.010].

Martel, C., Dingwell, D.B., Spieler, O., Pichavant, M., Wilke, M., 2001. Experimental fragmentation of crystal- and vesicle-bearing silicic melts. *Bull. Volcanol.,* 63, pp398-405. [doi: 10.1007/s004450100157].

Martel, C., Schmidt, B.C., 2003. Decompression experiments as an insight into ascent rates of silicic magmas. *Contrib. Mineral. Petrol.,* 144, pp397–415. [doi: 10.1007/s00410-002-0404-3].

Marxer, H., Bellucci, P. and Nowak, M., 2015. Degassing of H_2O in a phonolitic melt: A closer look at decompression experiments. *J. Volcanol. Geotherm. Res.,* 207, pp109-124. [doi: 10.1016/j.jvolgeores.2014.11.017].

Marxer, H., Nowak, M., 2013. Micro-FTIR imaging: an advanced method for the determination of CO_2 and H_2O concentration gradients in silicate glasses. *Eur. J. Mineral.,* 25(3), pp307–316. [doi: 10.1127/0935-1221/2013/0025-2299].

Massol, H., Koyaguchi, T., 2005. The effect of magma flow on nucleation of gas bubbles in a volcanic conduit. *J. Volcanol. Geotherm. Res.,* 143(1-3), pp69-88. [doi: 10.1016/j.jvolgeores.2004.09.011].

Mastin, L.G., 2002. Insights into volcanic conduit flow from an open-source numerical model. *Geochem. Geophys. Geosyst.,* 3(7), pp1-18. [doi: 10.1029/2001GC000192].

McBirney, A.R. and Murase, T., 1970. Factors governing the formation of pyroclastic rocks *Bull. Volcanol.,* 34, pp372 - 384. [doi: 10.1007/BF02596762].

McBirney, A.R., 1963. Factors governing the nature of submarine volcanism. *Bull. Volcanol.,* 26, pp455-469. [doi: 10.1007/BF02597304].

McIntosh, I.M., 2013. 'Bubble growth and resorption in magma: insights from dissolved water distributions in volcanic glass'. Durham theses, Durham University. [Available at Durham E-Theses Online: http://etheses.dur.ac.uk/8505].

McIntosh, I.M., Llewellin, E.W., Humphreys, M.C.S., Nichols, A.R.L., Burgisser, A., Schipper, C.I., Larsen, J.F., 2014. Distribution of dissolved water in magmatic glass records growth and resorption of bubbles. *Earth Planet. Sci. Lett.,* 401, pp1-11. [doi: 10.1016/j.epsl.2014.05.037].

Mitchell, S. J., 2018. 'Deep submarine silicic volcanism: Conduit and eruptive dynamics of the 2012 Havre eruption'. [Available from ProQuest Dissertations & Theses Global.

(2190795042). Retrieved from https://www.proquest.com/dissertations-theses/deep-submarine-silicic-volcanism-conduit-eruptive/docview/2190795042/se-2?accountid=11455].

Mitchell, S.J., McIntosh, I.M., Houghton, B.F., Carey, R.J. and Shea, T., 2018. Dynamics of a powerful deep submarine eruption recorded in H_2O contents and speciation in rhyolitic glass: The 2012 Havre eruption. *Earth. Planet. Sci. Lett.,* 494, pp135-147. [doi: 10.1016/j.epsl.2018.04.053].

Mourtada-Bonnefoi, C.C., Laporte, D., 2004. Kinetics of bubble nucleation in a rhyolitic melt: an experimental study of the effect of ascent rate. *Earth. Planet. Sci. Lett.*, 218, pp521-537. [doi: 10.1016/S0012-821X(03)00684-8].

Mourtada-Bonnefoi, C.C., Mader, H.M., 2004. Experimental observations of the effect of crystals and pre-existing bubbles on the dynamics and fragmentation of vesiculating flows. *J. Volcanol. Geotherm. Res.* 129, pp83-97.

Moussellam, Y., Oppenheimer, C., Scaillet, B., Buisman, I., Kimball, C., Dunbar, N., Burgisser, A., Schipper, C.I., Andujar, J., Kyle, P., 2015. Megacrystals track magma convection between reservoir and surface. *Earth. Planet. Sci. Lett.*, 413, pp1-12. [doi: 10.1016/j.epsl.2014.12.022].

Mueller, S., Melnik, O., Spieler, O., Scheu, B. & Dingwell, D. B., 2005. Permeability and degassing of dome lavas undergoing rapid decompression: an experimental determination. *Bull. Volcanol.*, 67, pp526–538. [doi: 10.1007/s00445-004-0392-4].

Mueller, S., Scheu, B., Spieler, O. & Dingwell, D. B., 2008. Permeability control on magma fragmentation. *Geology,* 36(5), pp399-402. [doi: 10.1130/G24605A.1].

Nichols, A.R.L., Potuzak, M., Dingwell, D.B., 2009. Cooling rates of basaltic hyaloclastites and pillow lava glasses from the HSDP2 drill core. *Geochim. Cosmo. Acta.,* 73(4), pp1052 – 1066. [doi: 10.1016/j.gca.2008.11.023].

Pal, R., 2003. Rheological behaviour of bubble-bearing magmas. *Earth. Planet. Sci. Lett.,* 207(1-4), pp165-179. [doi: 10.1016/S0012-821X(02)01104-4].

Pappalardo, L., Buono, G., Fanara, S., Petrosino, P., 2018. Combining textural and geochemical investigations to explore the dynamics of magma ascent during Plinian eruptions: a Somma-Vesuvius volcano (Italy) case study. *Contrib. Mineral. Petrol.,* 173, 61. [doi: 10.1007/s00410-018-1486-x].

Petcovik, H.L., Dufek, J.D., 2005. Modelling magma flow and cooling in dikes: Implications for emplacement of Columbia River flood basalts. *J. Geophys. Res.,* 110, B10201. [doi: 10.1029/2004JB003432].

Pitzer, K.S., Sterner, S.M., 1994. Equations of state valid continuously from zero to extreme pressures for H_2O and CO_2, *J. Chem. Phys.* 101, 31111. [doi: 10.1063/1.467624].

Polacci, M., Papale, P., Rosi, M., 2001. Textural heterogeneities in pumices from the climactic eruption of Mount Pinatubo, 15 June 1991, and implications for magma ascent dynamics. *Bull. Volcanol.*, 63, pp83–97. [doi: 10.1007/s004450000123].

Proussevitch, A.A. and Sahagian, D.L., 1998. Dynamics and energetics of bubble growth in magmas: Analytical formulation and numerical modelling. *J. Geophys. Res.,* 103(B8), pp18223-18251. [doi: 10.1029/98JB00906].

Proussevitch, A.A., Sahagian, D.L., 1996. Dynamics of coupled diffusive and decompressive bubble growth in magmatic systems. *J. Geophys. Res. Solid Earth,* 101(B8), pp17447–17455. [doi: 10.1029/96JB01342].

Proussevitch, A.A., Sahagian, D.L., Anderson, A.T., 1993. Dynamics of diffusive bubble growth in magmas: Isothermal case. *J. Geophys. Res. Solid Earth,* 98(B12), pp22283–22307. [doi: 10.1029/93JB02027].

Rayleigh, L., 1917. On the pressure developed in a liquid during the collapse of a spherical cavity. *Philos. Mag.,* 34, pp94-98. [doi: 10.1080/14786440808635681].

Regier, M.E., Hervig, R.L., Myers, M.L., Roggensack, K., Wilson, C.J.N., 2016. Analyzing nitrogen in natural and synthetic silicate glasses by secondary ion mass spectrometry. *Chem. Geol.,* 447, pp27-39. [doi: 10.1016/j.chemgeo.2016.10.019].

Rust, A.C., Cashman, K.V., 2011. Permeability controls on expansion and size distributions of pyroclasts. *J. Geophys. Res. Solid Earth,* 116(B11), pp1–17. [doi: 10.1029/2011JB008494].

Rust, A., Cashman, K., Wallace, P., 2004. Magma degassing buffered by vapor flow through brecciated conduit margins. *Geology,* 32(4), pp349–352. [doi:10.1130/G20388.2].

Rust, A.C., Manga, M., Cashman, K.V., 2003. Determining flow type, shear rate and shear stress in magmas from bubble shapes and orientations. *J. Volcanol. Geotherm. Res.,* 122(1-2), pp111-132. [doi: 10.1016/S0377-0273(02)00487-0].

Rutherford, M.J., 2008. Magma Ascent Rates. *Revs. Mineral. Geochem.,* 69, pp241-271. [doi: 10.2138/rmg.2008.69.7].

Scandone, R., Cashman, K.V., Malone, S.D., 2007. Magma supply, magma ascent and the style of volcanic eruptions. *Earth. Planet. Sci. Lett.,* 253, pp513-529. [doi: 10.1016/j.epsl.2006.11.016].

Shea, T., 2017. Bubble nucleation in magmas: A dominantly heterogeneous process? *J. Volcanol. Geotherm. Res.,* 343, pp155-170. [doi: 10.1016/j.jvolgeores.2017.06.025].

Sparks, R. S. J., 2003. Dynamics of magma degassing. *Geol. Soc. Lond. Spec. Publ.,* 213, pp5–22. [doi: 10.1144/GSL.SP.2003.213.01.02].

Sparks, R.S.J., 1978. The dynamics of bubble formation and growth in magmas: a review and analysis. *J. Volcanol. Geotherm. Res.,* 3(1-2), pp1-37. [doi: 10.1016/0377-0273(78)90002-1].

Sparks, R.S.J., Annen, C., Blundy, J.D., Cashman, K.V., Rust, A.C., Jackson, M.D., 2019. Formation and dynamics of magma reservoirs. *Phil. Trans. R. Soc. A.,* 377, 20180019. [doi: 10.1098/rsta.2018.0019].

Sparks, R.S.J., Tait, S.R., Yanev, Y., 1999. Dense welding caused by volatile resorption. *J. Geol. Soc.* 156, pp217-225. [doi: 10.1144/gsjgs.156.2.0217].

Suzuki, K., Nakamura, K., Kato, S., Yamagishi, A., 2009. Experimental Approach to Obtain a Comprehensive Understanding of Biogeochemistry of a Seafloor Hydrothermal System. *J. Geography.,* 118(6), pp1131-1159. [doi: 10.5026/jgeography.118.1131].

Taracsák, Z., Neave, D.A., Beaudry, P., Gunnarsson-Robin, J., Burgess, R., Edmonds, M., Halldorsson, S.A., Longpre, M-A., Ono, S., Ranta, E., Stefánsson, A., Turchyn, A.V., EIMF, Hartley, M.E., 2021. Instrumental mass fractionation during sulfer isotope analysis by secondary ion mass spectrometry in natural and synthetic glasses, *Chem. Geol.*, 578, 120318. [doi: 10.1016/j.chemgeo.2021.120318].

Toramaru, A., 1995. Numerical study of nucleation and growth of bubbles in viscous magmas. *J. Geophys. Res.*, 100(B2), pp1913-1931. [doi: 10.1029/94JB02775].

Toramaru, A., 2006. BND (bubble number density) decompression rate meter for explosive volcanic eruptions. *J. Volcanol. Geotherm. Res.,* 154(3-4), pp303-316. [doi:10.1016/j.jvolgeores.2006.03.027].

Tuffen, H., Castro, J.M., 2009. The emplacement of an obsidian dyke through thin ice: Hrafntinnuhryggur, Krafla Iceland. *J. Volcanol. Geotherm. Res.,* 185(4), pp352-366. [doi: 10.1016/j.jvolgeores.2008.10.021].

Tuffen, H., Dingwell, D., and Pinkerton, H., 2003. Repeated fracture and healing of silicic magma generate flow banding and earthquakes? *Geology,* 31(12), pp1089–1092. [doi:10.1130/G19777.1].

Tuttle, O.F., 1948. A new hydrothermal quenching apparatus. American J. Sci., 246 (10), 628-635). [doi: 10.2475/ajs.246.10.628].

Verhoogen, J., Mechanics of Ash Formation, 1951. *A. J. Sci.,* 249(10), pp729-739. [doi: 10.2475/ajs.249.10.729].

Vogel, D.H., 1921. Temperaturabhängigkeitsgesetz der Viskosität von Flüssigkeiten. *Phys.,* 22, pp645-646.

Watkins, J.M., Gardner, J.E., Befus, K.S., 2017. Nonequilibrium degassing, regassing, and vapor fluxing in magmatic feeder systems. *Geology,* 45(2), pp183-186. [doi: 10.1130/G38501.1].

Watkins, J.M., Manga, M. & DePaolo, D.J., 2012. Bubble geobarometry: A record of pressure changes, degassing, and regassing at Mono Craters, California. *Geology,* 40(8), pp699-702. [doi: 10.1130/G33027.1].

Westrich, H.R., Eichelberger, J.C., 1994. Gas transport and bubble collapse in rhyolitic magma: an experimental approach. *Bull. Volcanol.,* 56, pp447-458. [doi: 10.1007/BF00302826].

White, J.D.L., Valentine, G.A., 2016. Magmatic versus phreatomagmatic fragmentation: Absence of evidence is not evidence of absence. *Geosphere.* 12(5), pp1478-1488. [doi: 10.1130/GES01337.1].

Wilson, L., 1980. Relationships between pressure, volatile content and ejecta velocity in three types of volcanic explosions. *J. Volcanol. Geotherm. Res.,* 8(2-4), pp297–313. [doi: 10.1016/0377-0273(80)90110-9].

Winson, A. E. G., Newhall, C. G., Costa Rodriguez, F., 2014. Is there a recipe for Plinian eruptions? Evidence from past events and analogous volcanoes. *American Geophysical Union, Fall Meeting 2014.,* abstract id: V41B-4819. [bibcode: 2014AGUFM.V41B4819W].

Wright, R., Garbell, H., Davies, A.G., 2010. Cooling rate of some active lavas determined using an orbital imaging spectrometer. *J. Geophys. Res.,* 115(B6), B06205. [doi: 10.1029/2009JB006536].

Yoshimura, S., Nakamura, M., 2008. Diffusive dehydration and bubble resorption during open- system degassing of rhyolitic melts. *J. Volcanol. Geotherm. Res.,* 178(1), pp72-80. [doi: 10.1016/j.jvolgeores.2008.01.017].